EXPERIMENTAL AND NUMERICAL MODEL STUDIES OF FRICTIONAL INSTABILITY SEISMIC SOURCES

by

Paul G. Okubo

B.S.E., Princeton University (1975)
M.A., University of California, Berkeley (1977)

SUBMITTED TO THE DEPARTMENT OF
EARTH, ATMOSPHERIC, AND PLANETARY SCIENCES
IN PARTIAL FULFILLMENT
OF THE REQUIREMENTS
FOR THE DEGREE OF

DOCTOR OF PHILOSOPHY

at the

MASSACHUSETTS INSTITUTE OF TECHNOLOGY

January 1986

Signature of Author _____
Department of Earth, Atmospheric, and Planetary Sciences

Certified by _____ 1/17/86
Keiiti Aki
Thesis Supervisor

Accepted by _____
Chairman, Department Committee on
Graduate Students

EXPERIMENTAL AND NUMERICAL MODEL STUDIES OF FRICTIONAL INSTABILITY SEISMIC SOURCES

by

PAUL G. OKUBO

Submitted to the Department of Earth,
Atmospheric, and Planetary Sciences
on January 17, 1986 in partial fulfillment of the
requirements for the Degree of Doctor of Philosophy

ABSTRACT

Stick-slip frictional instability is widely regarded as a viable mechanism for crustal earthquakes, particularly because of the way that it can be incorporated into the notion of earthquakes as episodic unstable slip events along preexisting zones or planes of weakness represented by faults in the Earth. In this thesis, detailed laboratory observations of stick-slip events generated on a simulated fault provide a basis for extending a constitutive description of frictional sliding developed from quasistatic experiments to describe fault response under dynamic slip conditions. An appropriate fault constitutive relation is implemented into a numerical model of dynamic crack propagation. Test calculations reveal that a fully specified rate- and fault state-dependent friction constitutive model is capable of producing effects which are consistent with earlier predictions of dynamic fault rupture using simpler slip weakening fault models, but differences from the slip weakening calculations arise because of some of the features of the state variable friction model. A possible means for extending the modeling to the scale of crustal earthquakes by assessing suitable length scales based on a fractal geometry approach is presented.

Stick-slip shear failures have been generated on simulated faults of two different roughnesses and at different levels of applied normal stress σ, between 0.6 and 4 MPa. The unique, large test sample size (2 m fault length) used in these experiments provides the opportunity to investigate the shear instability over length scales which are not allowed by typical laboratory rock mechanics experiments, and the stick-slip event is clearly viewed as a crack-like failure which nucleates in one part of the fault and subsequently propagates over the entire fault surface. Rupture velocities are of the same order as the seismic wave speeds in the granite test sample. In addition, high-speed records of local shear stress and fault slip reveal details of the initial breakdown of fault frictional resistance or strength at the onset of stick slip resembling slip weakening. A critical displacement d_c associated with this slip weakening is identified and it is observed to be relatively insensitive to normal stress acting on the fault. This displacement parameter is larger for the rougher of the two prepared fault surfaces. Stick-slip stress drops and fracture energies increase with increasing normal stress, and fracture energies also increase for increased fault roughness through the dependence of critical displacement on roughness. The existence of a critical weakening displacement implies that the rupture characteristics of the stick-slip events are scale-dependent, based either on a critical crack length or, alternatively, a crack endzone size. Both the critical crack and crack endzone increase with increasing roughness and decrease with increasing normal stress. Rupture and slip velocities from both the smooth and the rough fault surfaces, reflect this scale-dependence such that when a rupture propagation distances are scaled by critical crack length, the data indicate that rupture velocity and fault

slip velocity increase with increasing fault length.

Similarities between the slip weakening-like behavior of the fault at the onset of stick slip and an analogous transition observed when fault surfaces initially sliding at a constant slip rate are quasistatically forced to slide at another rate suggest that rate- and state-dependent friction models motivated by the quasistatic observations might apply to the dynamic slip conditions as well. Calculated friction time histories based on the recorded slip histories and rate- and state-dependent friction constitutive relations compare favorably with recorded stress histories. While the fault frictional response is inferred to be formally rate- and state-dependent, the data do suggest that an appropriate friction model must include cutoffs to the velocity-related effects so that, at high speed slip beyond the cutoff values, the fault response can be regarded as rate-independent or as slip weakening, at least during the stick-slip instability.

The rate- and state-dependent friction model that fit the stick-slip data is implemented into a numerical model of a dynamic plane-strain shear crack. The model is a boundary integral, or numerical Green function, method which was previously used to solve the problems of elastic-brittle and slip-weakening shear cracks. The numerical crack solutions are generally consistent with slip weakening calculations and they display the effects of varying normal stress and critical fault displacement on the growth of the crack, generally consistent with the laboratory observations in that smaller d_c and larger σ both tend to decrease the size of the critical crack. Jumps in rupture velocity which take place as the traction peak associated with the S-wave becomes large enough to drive the rupture occur sooner with respect to critical length in the state variable calculations. This is possibly related to a stage of accelerating creep before the onset of the instability which is admitted only by the state variable friction model. Fault initial conditions are not uniquely specified in terms of a strength-to-prestress ratio s. Initial values of slip rate and state variable can be traded off so that a given s can be achieved in an infinite number of ways.

Extending the laboratory and numerical results to earthquakes and natural faults depends on the critical lengths. In the laboratory data, the cohesive endzone size is related to a characteristic cutoff frequency in the stick-slip spectrum. This implies that a cutoff frequency related to earthquake endzone size is expected, but identification of this frequency in the seismic spectrum requires that the effects of wave propagation path and near-receiver structure are not felt. Quasistatic modeling of crustal scale faults favors d_c many times larger than the largest d_c values measured in the laboratory. Large scale fault complexity like fault discontinuities or fault branching have been recognized as important in influencing fault behavior. Using detailed fault trace maps from portions of the San Andreas Fault, it is possible to characterize fault trace complexity in these regions in terms of fractal geometry. It is observed that a critical length exists and acts as a fractal cutoff such that, for scales greater than the critical length, fault trace sets are non-fractal. Within the cutoff, and, at least down to the smallest scale measurable on the map, fault traces exhibit fractal geometric features. The cutoffs appears to be related to fault zone widths which vary from region to region. The values of the cutoffs also coincide with estimates of endzone sizes for moderate and larger California earthquakes derived by assuming that the observed limiting frequency f_{max} is a source effect. If fractal cutoff or f_{max} is related to fault cohesive zone size, then critical lengths for faulting can be determined.

Thesis supervisor: Keiiti Aki
Title: Professor of Geophysics

ACKNOWLEDGMENTS

I would like to begin these acknowledgments by expressing my most sincere thanks and appreciation to my thesis adviser, Professor Keiiti Aki. It has been a privilege to be able to work and study with Professor Aki and to enjoy the openness, the optimism and the genuine interest with which he approaches (students' and his) research. I hope that someday I can develop my intuitions and my approach to research problems to operate in a similar manner to his.

Much of this thesis work was done at the United States Geological Survey in Menlo Park, CA . I am grateful to Professor Aki and the rest of my thesis committee for approving this research plan to allow me to work there. At the Survey, my principal adviser has been Dr. James Dieterich. I owe so much to Jim whose encouragement and support over the years has made all of the difference in my chasing after a scientific research career. Many thanks to Jim and his wife Susan for their caring and their support. Another adviser at the Survey has been Dr. Joe Andrews, who generously provided the boundary integral code that was used for the calculations in Chapter 4. Joe's door has always been wide open, and he has always willingly fielded my questions - from fracture energy to fractals to boundary integrals - and freely provided suggestions and insights.

At MIT, I was very fortunate to be stationed on the 5th floor, in offices with the likes of Roger Buck, Dan Davis, Joao Rosa, and Mark "Hunter S." Murray. Thanks to them and to Lynn Hall, Paul Huang, Greg Beroza, Bob Grimm and Justin Revenaugh for lots of interesting discussions, good humor, and moral support. Jeanne Sauber and Kiyoshi Yomogida provided me with some really good examples to try to follow: Jeanne, so kind and generous of spirit, and Kiyoshi, so full of enthusiasm and so optimistic - continually telling me "Don't worry so much !!" Mavis Driscoll and Paul Scharr, Barbara Braatz, Barbara and Eric Sheffels, Sharon Feldstein, Jan Nattier-Barbaro, Sharon Quayle, Kaye

Shedlock, and Scott Phillips all contributed significantly to the environmental protection service, too.

While Professor Aki was not here and I was, I greatly appreciated Professor Sean Solomon's willingness to discuss things. I admire his careful and thoughtful approach. Professor Brace provided some important encouragement very early on and in connection with the friction workshop that was held at Harvard in March, 1983. These are all things that helped to make a difference to me.

It was my very good fortune to be so close to Harvard where I was able to get to know Professor James Rice and his research group. He and Dr. Renata Dmowska are capable of generating so much excitement and enthusiasm for geophysics in a single short conversation. Their openness and optimism, too, are real treasures for all of us students.

Teng-Fong Wong, Brian Bonner, Andy Ruina, David Lockner, and Shamita Das have all been very helpful and always provided lots of encouragement. Toward the more distant past, earlier advisers were instrumental in my development of research interests and approach. Professor Tom Jordan pointed me toward seismology when I was an undergraduate. It's a nice coincidence that he's now here at MIT (at least I've graduated from college now). Professor Lane Johnson probably gave some of the best advice when he said "You've got to go with the good experiment when you see one," when I was first looking into going to work with Jim Dieterich. He has continued to be very supportive and interested in what I've been doing. Thanks to them all.

Partial financial support came from NSF grant ENG-8408227.

Now there's Joan with whom I can share everything. She makes a world of difference to me.

Final words of thanks and aloha to my parents, for their tremendous examples, encouragement, and support. None of this would have been attempted had it not been for their constant supply of strength and faith and love.

Experimental and Numerical Model Studies

of

Frictional Instability Seismic Sources

Chapter 1 - Introduction

Since the pioneering study of Reid [1910] which suggested that earthquakes represent the sudden release of accumulated strains by episodic slip along a fault, there has been a close identification of the earthquake source process with slip along a fault plane. A vast body of literature has emerged, focusing on understanding or describing the mechanics of the faulting process. Obviously, two practical considerations motivate these and similar attempts, earthquake prediction and the prediction of the ground motions produced during an earthquake in order to reduce potential risk to engineering structures.

Kinematic fault models have been developed to address this second question of predicting and understanding the radiated ground motions produced by an earthquake. It generally seems that the degree of detail included in these models has grown with the sophistication of the instrumentation that records the seismic motions. Along with this, the development of powerful general elastodynamic representation theorems by Maruyama [1963] and Burridge and Knopoff [1964] has been exploited to address the inverse problem of estimating properties of the source from the seismic wave field. Interpreting the kinematic solution in terms of possible physical source processes is, in a sense, yet another inverse problem.

Dynamic earthquake source models have also been developed. These are commonly based on idealizing the earthquake as a dynamically extending shear crack. By assuming a fault failure criterion and otherwise being able to prescribe initial loading conditions and material properties, the crack rupture history is determined. The physics of the earthquake source process is incorporated into the failure criterion. With an incomplete understanding of the fault failure process, dynamic earthquake source modeling has drawn from the theory of fracture for modeling insights.

The suggestion by Brace and Byerlee [1966] of the stick-slip frictional instability as a crustal earthquake source process introduced the possibility of experimentally determining appropriate fault constitutive properties with laboratory tests on fault materials and simulated faults. Many laboratory rock friction studies have been reported on, concerned with the effects of rock type, loading conditions and loading history, fault surface preparation , and other experimental variables. A review of much of this work can be found in Paterson [1978].

Recently, a class of frictional constitutive relation has been one focus of laboratory investigation and theoretical development. This type is now sometimes referred to as the state variable, or rate- and state-dependent, friction model. It was developed out of observations of the time and slip rate dependence of rock friction [Dieterich, 1972 and 1978a], and it uses modeling concepts that were originally introduced into constitutive descriptions of the frictional behavior of metals. In addition to accounting for a variety of laboratory observations, the state variable friction models predict a wide range of frictional behavior. They have been used to model features of crustal earthquake occurrence and details of the frictional sliding process leading up to and through the stick-slip instability.

This discussion of frictional stick-slip instabilities begins with a description of a series of laboratory experiments undertaken to resolve details of the stick-slip dynamic shear failure of a simulated fault. In Chapter 2, the observations from these experiments, performed to investigate the effects of fault surface roughness and applied normal stress, are summarized. The samples used in these tests are the largest used in the study of the frictional sliding of simulated fault surfaces in rock samples, with a simulated fault length of approximately 2 m . An early analysis [Dieterich *et al.*, 1978] suggested that this fault length represented a realistic fault dimension, given suitable applied load levels and sliding surface characteristics, which would allow the containment of a stick-slip event within the free ends of the simulated fault surface. The large sample size and the use of a high-speed data

acquisition system readily allow the observation of details of the growth of the stick-slip failures, and the large sample size facilitates transducer deployment so that measurements are made directly adjacent to and across the sliding surface. Thus, the data rather directly reflect details of the deformations and motions along the fault surface during stick-slip sliding.

From recordings of fault displacement and shear stress at individual "station" locations, the breakdown process at the onset of stick-slip can be resolved, and it is observed that the fault follows an apparent displacement weakening-like course. A displacement parameter which characterizes the duration of the breakdown is identified in these observations. Source parameters, stress drop, fault slip rate, fracture energy, and rupture velocity, are measured. In general, the effect of increasing normal stress on the stick-slip source parameters is to increase stress drop, average slip rate during stick slip, and fracture energy. Stick-slip events generated on a fault with increased roughness are associated with increased fracture energy, but, more importantly, the roughness imposes a different length scale for the stick-slip failure process such that the stick slip on a roughened fault surface requires a greater nucleation distance and spreads out over the fault at slower rates.

In addition, the observations made locally as the dynamic rupture spreads over the simulated fault suggest that the characteristic displacement for a stick-slip event reflects the same transitional behavior from an initial sliding configuration to a final configuration as observed in quasistatic laboratory tests and which is featured in the state variable friction models. In Chapter 3, this suggestion is further investigated, with the potential for identifying an appropriate fault constitutive relation for stick-slip. Model calculations of the fault frictional response using combinations of recorded and estimated slip rate history information are carried out using two specific forms of the state variable law which are equally suited for describing low speed slip. Comparisons of these calculations with the corresponding recorded stress histories indicate that velocity cutoffs to limit the frictional response of the fault at very high slip rates are required to match the recorded stick-slip data.

In Chapter 4, a numerical model of a dynamic shear crack governed by a state variable friction law, with high speed cutoffs, is developed from a boundary integral solution method originally proposed for the two-dimensional crack problem by Hamano [1974]. This solution had been previously used for elastic-brittle crack modeling [Das, 1976; Das and Aki, 1977a] and for slip-weakening crack modeling [Andrews, 1985]. Due to the effects of the high-speed cutoffs, the state variable fault models share some features with the slip-weakening models and can be understood in terms of the theory of fracture of cracks with finite peak limiting strength. They differ with regard to features specific to a rate- and state-dependent friction model. Consistent with fracture theory for shear cracks with finite peak yield stress, dynamic cracks governed by a state variable friction model are capable of propagating at transsonic rupture speeds, and, under certain circumstances, a jump from stable crack extension at the Rayleigh wave speed to crack extension at super-shear wave speeds is clearly observed. For analogous initial stress conditions, the onset of super-shear crack growth occurs sooner, with respect to a critical dynamic crack length, for a state variable crack model than for a strictly slip weakening crack model. The critical crack length is directly dependent upon a friction model parameter analogous to a critical slip weakening displacement.

Natural faults are obviously longer and more complicated than the simulated faults that can be readily tested in the laboratory. Uncertainty as to how the results obtained in laboratory testing can be applied to the length scales of natural faults has classically prevented detailed incorporation of laboratory modeling results into field problems. Uncertainty with regard to defining relevant scaling lengths for earthquake processes hinders the application of fracture theories to earthquakes, although Rice [1980] outlines a small-scale yielding critierion that must be satisfied in order to justify a crack-based analysis.

In Chapter 5, a cohesive zone critical length for stick-slip events is first presented. In the laboratory, where local stress and displacement data registered directly on the fault are

available, the cohesive zone length can be determined from the time duration of the fault breakdown process at the onset of stick-slip sliding. A cutoff frequency in the Fourier amplitude spectra of recorded stress signals is associated with this breakdown time, so that, it would be possible to estimate the size of the cohesive zone without data from on the fault if this cutoff frequency characteristic is preserved through the wave propagation.

Also in Chapter 5, geometric critical lengths are identified for the geometry of mapped fault traces as fractal cutoffs beyond which the fault traces can be regarded as essentially linear topologic features. Below the cutoffs, fault traces in subsets of the San Andreas Fault system are fractal sets for which a length measure depends upon the resolution of the measuring technique and increases with finer resolution. Thus, fractal fault trace geometry is not scale-invariant. Moreover, the cutoffs vary with position along the fault so that different subsets of the fault are subject to different fractal cutoffs.The values of the geometric critical lengths coincide with estimates of fault cohesive endzone sizes based on a fracture mechanics interpretation of both historical and instrumental seismic records [Aki, 1979]. If a physical correlation can be established among the geometric fault features and other observations that relate to the endzone sizes of earthquakes, then the possibility exists for associating appropriate scales with the mechanics of earthquake faulting.

Chapter 2 - Laboratory Results : The Effects of Fault Surface Roughness and Normal Stress

2.1 Introduction

Stick-slip frictional instability as a mechanism for crustal earthquake failure was suggested by Brace and Byerlee[1966], who noted that stick-slip behavior as observed in laboratory tests could account for the episodic occurrence of earthquakes on faults characterized by stress drops which are low compared to the strengths of intact rocks. Utilizing high-speed recording systems, it is possible to study the details of stick-slip failures as seismic sources. Several studies of this nature describing observations of stick-slip events generated on simulated faults in rock samples and samples of synthetic materials have been reported [Wu *et al.*,1972; Archuleta and Brune, 1975; Hartzell and Archuleta, 1979; Ohnaka, 1973; Johnson *et al.*, 1973; Johnson and Scholz, 1976; Dieterich, 1980]. Results which are common to these studies are that stick-slip rupture velocities are of the order of the seismic wave speeds and that the particle or slip velocities are orders of magnitude less. Slip velocities are related to the stress drops accompanying the stick-slip failures. The stress drops are related to the normal stress acting on the fault at the time of the stick-slip failure.

Wu *et al.* [1972] observed the onset and arrest of propagating stick-slip failures produced on a fault cut into a sheet of CR 39 plastic. The series of experiments begun by Brune [1973] and continued by Archuleta and Brune [1975] and Hartzell and Archuleta [1979] made similar observations on two-dimensional faults cut into blocks of foam rubber. They investigated the effects of both fault length and fault width on the stick-slip events. Because the seismic wave speeds in these synthetic materials are lower than those in granites or other rock types commonly used in laboratory work, details of the propagation of the stick-slip events are more readily observed without requiring extremely fast recording equipment. However, this same feature, namely, the different material properties of the

laboratory samples, renders more difficult the direct application of these results to questions concerning earthquake faulting without a more quantitative knowledge of the constitutive behavior of these materials.

Johnson *et al.* [1973], Ohnaka [1973], Johnson and Scholz [1976], and Dieterich [1980] have examined some aspects of propagating stick-slip in rock samples. The principal difficulty which accompanies experimental work done on rock samples is related to the scaling of lengths and rates to values which more accurately represent deformation processes in the Earth. An example of this problem which is relevant to laboratory stick-slip studies on small samples is that the entire sliding surface moves during the slip event so that interactions leading to the arrest of stick-slip sliding depend upon finite sample size and properties of the testing apparatus. Therefore, it is generally not possible to investigate directly the properties of the fault which can lead to the arrest of the propagating failure on a patch of pre-existing fault. Nevertheless, it is still possible to study in detail the onset of sliding and the propagation of the stick-slip failure on simulated faults.

In this chapter, we present observations of stick-slip events produced on a simulated fault cut into a large granite test sample. The large sample dimensions in these experiments permit detailed resolution of propagating stick-slip events and a consideration of length scaling questions. We have generated stick-slip events at different normal stresses on simulated faults of two different roughnesses. Stresses and displacements are recorded at high sampling rates and provide resolution of the local breakdown processes as the stick-slip failure spreads over the simulated fault. We estimate dynamic source parameters of the events and discuss factors which might control them.

2.2 Apparatus, Recording System and Experimental Procedures

Details of the apparatus used in these experiments are given by Dieterich *et al* . [1978] and Dieterich [1981b]. The loading press is a special purpose biaxial press developed

at the United States Geological Survey in Menlo Park, California to study the mechanics of large-scale simulated faults. The press accommodates samples with dimensions of 1.5 x 1.5 x 0.4 m. The press has a loading capacity of 2.2 x 10^7 N in the major principal stress direction and 1.2 x 10^7 N in the minor principal stress direction.

Figure 2.1 is a sketch showing the apparatus with a rock sample in place. The samples that have been used to the present are blocks of Sierra white granite from the quarry near Raymond, California. Seismic wave speeds in this granite are v_p = 4.3 km/s and v_s = 2.9 km/s, measured at laboratory temperature and zero confining pressure. The simulated fault is a through-going sawcut surface oriented at a 45° angle to the sides of the sample. Hydraulic flatjacks positioned between the sample and the steel loading frame are used to apply loads to the sample biaxially, normal to the smallest sample dimension. Pressures in the flatjacks are servocontrolled independently in the two loading directions according to programmable loading histories. At different normal stresses between 0.6 and 4 MPa, the shear stress on the fault was gradually increased at a constant rate while the normal stress was maintained at a constant level until a stick-slip event occurred. Because of the approximate symmetry with respect to stiffnesses in the two loading directions, the normal stress remains at a roughly constant value, even through the stick-slip event [Goodman and Sundaram, 1978].

The samples are sawn to size, including the diagonal cut to simulate the fault, at the quarry. Final preparations of the sliding surface are carried out in the laboratory using a specially constructed lapping frame. For the series of experiments reported on here, two different fault roughnesses were used. Following a standard lapping procedure to attain suitably mated sliding surfaces, the smoother of the two faults was produced by final lapping of the surfaces with #240-grit silicon carbide abrasive. Identical procedures, including the lapping with the #240 grit, were followed in producing the rougher of the two faults. The final step in the preparation of the rough fault was to follow the fine lapping with a brief

period of lapping with a #30-grit abrasive to introduce rough features. The stick-slip behavior of simulated faults with both these roughnesses and with respect to the normal stresses applied to the fault was studied.

The large sample size and fault length of 2 m allow for improved recording resolution for the dynamic stick-slip sliding over that usually achieved in smaller scale rock mechanics experiments. Semiconductor strain gage pairs, oriented to monitor the shear strains parallel to the sliding surface, are mounted in a linear array 1 cm from the fault. The outputs of the strain gages have been calibrated against the signals from pressure transducers mounted at the flatjacks, and the strain signals can be scaled directly to represent shear stress. Velocity transducers are located at the same positions as the strain gages to monitor the relative offset of the fault. For each stick-slip event, ten channels of data from the strain gage and velocity transducers are recorded in high-speed digital memories which sample at 200,000 Hz. The velocity records are also integrated once in the time domain to provide estimates of fault displacement during the stick-slip events. With this instrumentation, it is possible to resolve clearly the details of the growth of the failed portion of the fault. It is also important to note that the records of fault deformation and displacement that are discussed below are local records of the failure process made from very close to the sliding surface, rather than the more commonly reported measures obtained from externally mounted load cells and displacement transducers, from which the stresses and displacements actually on the sliding surface are inferred.

2.3 Data

Digitized profiles along approximately 1-cm-long paths on the simulated fault surfaces were recorded using a Starrett electronic "Last Word" indicator. The radius of the probe tip was measured to be 40 μm. These profiles are plotted in Figure 2.2, and their starting positions are listed in Table 2.1 along with estimates of rms-height for each trace.

Seven profiles parallel to the direction of fault slip, A - G, and two profiles perpendicular to fault slip direction, H and J, were recorded from the smooth fault. They are shown in Figures 2.2a and 2.2b. The average rms-height over these 1-cm-long profiles is 1.54 μm. A comparison of the profiles taken in the two different directions suggests that the lapping procedures did not introduce strong differences in fault topography in these two directions.

Similarly, four profiles, K - N, taken from the rough fault in the direction parallel to fault slip are plotted in Figure 2.2c. This surface, as indicated by these profiles, appears to consist of relatively flat, or smooth, areas marked by pits as deep as 0.1 mm. The average rms-height of these rough fault profiles is 16.11 μm, about ten times larger than for the smoother fault. Profile P in Figure 2.2d was taken from the rough fault in a location which appeared, by inspection, to be similar to the smooth fault. The top plot in Figure 2.2d is scaled to the same amplitudes as those in Figure 2.2c. It resembles some of the flatter parts of the profiles in 2.2c. The lower plot is scaled to the same amplitudes as in Figures 2.2a and 2.2b . This profile resembles the smooth fault profiles except for more closely spaced intermediate-depth pits. Rms-height is 3.73 μm, which is slightly greater than the average smooth fault profile rms-height. Where the sliding surfaces are in contact, the smooth fault and rough fault appear to be similar.

Examples of the high-frequency (200 kHz) stick-slip data are given in Dieterich [1980, 1981a] and Okubo and Dieterich [1981, 1984]. Figure 2.3a shows the shear stress and fault displacement data from a stick-slip event generated on the smooth fault at a normal stress of 3.45 MPa. The numbers along the left side of the figure are the transducer locations expressed in millimeters measured from the upper right-hand corner of the block. The arrows at the top of the figure indicate the time of the onset of stick-slip sliding and the approximate time of termination of sliding.

Several characteristic features of stick-slip sliding can be seen in the figure.

1. Slip along the fault associated with the stick-slip event begins with a large and

rapid drop in shear stress. Sliding continues at a lower, relatively constant residual shear stress level until the end of sliding.

2. The stress drops at the different locations along the fault do not occur simultaneously, but, rather, they occur at different times. This indicates a propagation of the stick-slip failure from a nucleation region to other parts of the fault. The event pictured in Figure 2.3a begins near the strain gage at 953 mm and spreads bilaterally to the ends of the sample.

3. Slip at the different locations along the fault is preceded over fractions of a millisecond by increases in shear stress ahead of the propagating rupture.

4. The stress drops at the individual locations, while rapid, do occur over finite time intervals. During this time, as the fault weakens, a finite amount of fault slip is sustained. Such behavior is referred to as fault slip weakening, and it will be discussed to greater detail in later sections of this chapter and of this thesis.

5. In contrast to the onset of stick-slip, which is marked by large and rapid changes in shear stress and abrupt changes in fault slip velocity, the termination of fault slip appears to be a more gradual process without sudden changes in either stress or slip velocity. The long period oscillations observed after the end of the stick-slip event are free vibrations of the loading press-rock sample assembly.

6. The frictional sliding at the residual stress level is marked with small amplitude, high-frequency oscillations. Two possible explanations for this observation are that the oscillations are caused by interactions and fracturing of small-scale irregularities on the fault surfaces or that the oscillations are due to seismic energy, generated at the onset of the instability, which is reflected from the upper and lower free surfaces of the sample.

Data from a stick-slip instability generated on the rough fault, also at a normal stress of 3.45 MPa, are shown in Figure 2.3b. While displaying the same general features as the event shown in Figure 2.3a, this event took longer to achieve its eventual stress drop and it

propagated over the fault surface at a slower rate. The records do not exhibit the same high-frequency character following the onset of the rapid sliding as during the event generated on the smooth fault. Because the rough fault is characterized by a greater degree of irregularity than the smooth fault, we expect that the sliding at the residual shear stress level would involve more rupturing of surface irregularities or asperities. This might justify the expectation that, if this surface asperity interaction during sliding were indeed of a rupturing nature, there would be additional high-frequency signal associated with this process. However, because it is the smooth fault which appears to have extra high-frequency signal, we favor the interpretation that the high-frequency chatter observed for the smooth fault is reflected seismic energy and is not the result of the interaction of surface irregularities. Data are presented in Chapter 5 which address this question in further detail.

Another significant difference which is observed between the smooth fault and the rough fault is in the amounts of quasistatic fault offset prior to the stick-slip instability. Compared to the rough fault, events on the smooth fault were preceded by very little measurable fault creep. On the rough fault, stick-slip always followed a period of stable sliding with displacements often of the order of the displacements registered during the stick-slip event. The amount of stable fault offset and the duration of this period of stable fault creeping appears to be related to the degree of heterogeneity in shear stress along the simulated fault. Discussion of creep precursors to stick slip can be found in the work by Dieterich [1978b, 1979b] and Dieterich *et al.* [1978].

The fault slip weakening mentioned previously can be viewed directly by combining the records of shear stress and fault slip. If, for each paired strain gage/velocity transducer location, fault shear stress is plotted point-by-point as a function of fault displacement, a stress-vs-displacement, or fault slip weakening, curve similar to that shown in Figure 2.4 is obtained. The original shear stress and fault displacement records are shown in the lower part of the figure. The features of the fault slip weakening which were described from

looking at the time-domain records can be seen in detail here. (1) Shear stress builds up from the initial value τ_0 to a peak value τ_p prior to the occurrence of any measurable fault offset. (2) After peak shear stress τ_p is achieved, shear stress decreases with increasing fault displacement up to displacement d_r, beyond which (3) continued sliding occurs at the lower, relatively constant residual shear stress level τ_r until the end of sliding. Similar slip weakening is observed following the initiation of unstable fault slip or following a quasistatically achieved jump in slip rate [Dieterich, 1978b, 1979a, 1980, 1981b; Rice, 1980 (in a discussion of the experiments of Rummel *et al.*, 1978); Okubo and Dieterich, 1981, 1984]. Slip weakening in conjunction with stiffness of the system loading the fault determines the occurrence of stable or unstable slip [Dieterich, 1978a]. Finally, it is worth noting that the observations of fault slip weakening at the onset of stick slip which are presented here are local observations made at several locations directly adjacent to the sliding surface. Owing to limitations usually imposed by transducer size, such resolution of the dynamic shear failure of the fault was not obtained in earlier small-scale laboratory stick-slip studies.

2.4 Stick-slip Source Parameters

The following discussion presents data for a number of stick-slip source parameters and considers how they are affected by applied normal stress and fault roughness. In the accompanying figures, data for the rough fault are presented as triangles; those for the smooth fault are presented as circles.

2.4.1 Slip Weakening and Critical Displacements

Figures 2.5 and 2.6 summarize the observations of the slip-weakening behavior of the simulated fault during stick-slip sliding. From slip-weakening curves produced using the same procedures as for Figure 2.4, critical slip-weakening displacements d_r at each paired

strain gage/velocity transducer location are estimated. The critical slip-weakening displacement is taken as that amount of fault slip which is sustained as the shear stress on the fault decreases from its peak value to its residual sliding level.

The general character of slip-weakening behavior with varying normal stress and fault roughness is pictured in Figure 2.5. In Figure 2.5a, slip-weakening curves from the same transducer pair are shown for stick-slip events generated on the smooth fault at different normal stresses. In Figure 2.5, curves A are from events generated at a normal stress of 1.38 MPa, curves B at 2.76 MPa, and curves C at 3.45 MPa. Figure 2.5b is a similar presentation of rough fault slip-weakening data. For both fault roughnesses, the value of d_r does not appear to depend strongly on normal stress. The critical displacement on the rough fault is larger than on the smooth fault. These observations are consistent with the observations of Dieterich [1978a, 1981b] from studies of the quasistatic sliding behavior of small rock samples: independent of normal stress, rougher faults are characterized by larger critical slip-weakening displacements.

Figure 2.6 contains all of the slip-weakening critical displacement data. Measured values of d_r are plotted as a function of normal stress for both the rough fault (triangles) and the smooth fault (circles). Average values of d_r are 5 μm for the smooth fault and 25-30 μm for the rough fault. The occasional, larger values of d_r for events generated on the smooth fault are typically obtained from complicated records which suggest closely stacked, double or multiple stick-slip events occurring during a single experimental cycle.

Ida [1972], Palmer and Rice [1973], Andrews [1976] and Freund [1979], among others, discuss slip-weakening models in connection with shear crack propagation and other shear failure processes. These slip-weakening models extend the earlier concept of cohesive zones ahead of propagating tensile cracks proposed by Dugdale [1960] and Barenblatt [1962] to the case of shear failure. By using a cohesive zone model like a slip-weakening model, details of the breakdown process at the crack tip can be included directly in modeling the

growth of the crack or failure surface. Breakdown processes at the crack tip result in cohesive forces which act near the crack tip to resist additional growth of the crack. The cohesive zone is the zone on the slip surface over which the stresses vary from peak to residual values. In these models, the length of the cohesive zone is chosen theoretically in order to eliminate the crack tip singularity in stress which is characteristic of elastic-brittle crack tip stress fields. The experiments reported here provide an observational justification for introducing the concepts of cohesive zones and slip weakening ahead of the tips of dynamically propagating shear failures. Cohesive zone size can be estimated from the laboratory data by multiplying local rupture velocity by the time required to fully slip weaken at a strain gage location. Cohesive zones are of the order of 10-20 cm long and 20-100 cm for some of the events generated on the smooth and rough faults, respectively. The size of the cohesive zone decreases with increasing normal stress.

As shown, for example, by Palmer and Rice [1973] and Rice [1980], slip-weakening models also provide an interpretation of the energy release rate, or fracture energy, as introduced in engineering fracture mechanics. It is shown that the energy associated with a shear failure is given by integrating cohesive stress over slip-weakening displacement, that is, by integrating a slip-weakening curve and subtracting that work which is accounted for by frictional sliding at the residual shear stress level. The fracture energy and slip-weakening displacement permit other parametrizations that could prove to be very useful in modeling dynamic shear failures. Examples of these are the estimation of the size of the zone on the crack surface over which the cohesive stresses act and the estimation of a critical crack length beyond which further fault growth is achieved dynamically rather than in a quasistatic manner.

In later discussion, the concept of a critical shear crack length is used. It is based on a balance between the energy released by incremental crack extension and the energy which must be supplied to the crack system in order to overcome the effects of cohesive forces

acting near the crack tip. The critical crack length determination that is used is that by Andrews [1976], except that we specifically utilize the experimentally observed parameters d_r and stress drop. Similar approaches are taken by Dieterich *et al.* [1978] and Day [1982]. The result is that there is a critical crack length L_c beyond which the energy released with further crack advance is greater than the energy which must go toward creating newly cracked area, *i. e.*, the fracture energy. With this energy surplus, crack growth occurs dynamically. The critical crack length is given by:

$$L_c = \frac{2G\,(\,\lambda + G\,)\,(\tau_p - \tau_r)\,d_r}{\pi(\,\lambda + 2G\,)\,(\tau_0 - \tau_r)^2}. \qquad (2.1)$$

where λ and G are the Lame constants. As seen in this equation, L_c increases linearly with increasing d_r and it also scales approximately as (stress drop)$^{-1}$. Because stress drop is proportional to normal stress for frictional sliding, L_c decreases with increasing normal stress. Similarly, the cohesive end zone of rupture also decreases with decreasing normal stress.

2.4.2 Stress Drop and Slip Velocity

Two commonly reported dynamic stick-slip source parameters are stress drop and particle, or slip, velocity. As established in the development of general elastodynamic representation theorems, these parameters are important seismic source parameters so that experimental stick-slip friction studies can also be regarded from the viewpoint of seismic source mechanics and dynamically propagating failures.

Average stress drops for each stick-slip event are determined by simply averaging the local stress drops $\Delta\tau = \tau_0 - \tau_r$ recorded at the individual transducer locations during the event. The effects of fault roughness and normal stress on this average stress drop are

shown in Figure 2.7, which is a plot of stress drop as a function of applied normal stress. As seen in the figure, stress drops generally increase with increasing normal stress such that the average stress drop of a stick-slip event is between about 0.02 and 0.08 times the normal stress acting on the fault.

The stress drop data also suggest a fault roughness effect on the stick-slip stress drops. At a given normal stress, stress drops on the rough fault (triangles) are smaller than those of events generated on the smooth fault (circles). This same observation has been made in other experimental studies of stick-slip [Ohnaka, 1973; Dieterich, 1978a]. It might be possible to explain this effect in a qualitative way using the idea of a velocity-dependent frictional strength of the type introduced by Dieterich [1978a, 1979a] and used and developed by others. Because the rough fault undergoes more pronounced precursory creep than the smooth fault prior to the stick-slip sliding, the changes in slip rate experienced by the rough fault during the stick-slip event are correspondingly smaller on the rough fault. Within the framework of this type of friction model, *i. e.*, the rate- and state-dependent friction constitutive relation, these smaller changes in fault slip rate are accompanied by smaller changes in the frictional resistance of the fault. The rate- and state-dependent friction constitutive relations are discussed in greater detail in a later section of this thesis.

Slip velocity also increases with increasing normal stress. In Figure 2.8, average slip velocities are plotted as a function of normal stress. These are averages in the sense that they reflect the response of the entire fault. These slip velocities are determined by first estimating an average stick-slip duration time for the entire fault, also referred to as the stick-slip "rise time" by Ohnaka [1973] and Johnson and Scholz [1976], from the high-frequency velocity and displacement records and then dividing the total fault offset by this stick-slip duration time. The tendency for increasing average slip velocity with increasing normal stress can be seen.

Both experimental and theoretical fault modeling indicate that velocity during stick

slip is related to stress drop [Brune, 1970; Johnson and Scholz, 1976; Ohnaka, 1978; Shimamoto *et al.*, 1980]. The constant of proportionality for an embedded crack depends on the shear modulus and shear wave speed of the medium. Experimental observations of the linear relationship between stick-slip stress drop and slip velocity are typically explained in terms of spring and point mass fault models for which analytic solutions are readily obtained. In these solutions, stress drops and slip velocity are related through spring stiffness and system mass, and the fault offset is assumed to occur uniformly and over the entire fault surface simultaneously. (See, for example, Shimamoto *et al.* [1980].)

Stress drop and slip velocity are plotted together in Figure 2.9. These data represent estimates of slip velocity following the passage of the cohesive zone at a recording location and preceding the onset of complications in the records which arise from interactions of the stick-slip event with the ends of the rock sample. Unlike the data in Figures 2.7 and 2.8, each of the data in this figure is an estimate of the local fault slip velocity and stress drop obtained for a single position on the fault and not an average of data intended to represent the response of the entire fault. As seen in Figure 2.9, there is a direct relationship between stress drop and slip velocity for events generated on both the smooth and the rough fault surfaces.

Also plotted in Figure 2.9 is the theoretical stress drop/slip velocity relation, using suitable values for material properties v_s and G, predicted from what has become known as Brune's model [Brune, 1970]. The equation for this line is

$$v = 2 \frac{\Delta\tau}{G} v_s. \qquad (2.2)$$

where the factor of 2 arises because the slip rate measured in the experiments refers to the relative offset between the two sides of the fault rather than to the absolute particle motion. The model assumes that fault offset is achieved simultaneously over the entire fault,

essentially at infinite rupture speeds, similar to the analyses of stick slip produced in small laboratory samples. In Figure 2.9, the smooth fault data are scattered about the Brune model prediction. Perhaps the Brune model fits these data in an averaged sense, but, owing to its assumption of infinitely fast rupture propagation, it is not able, nor even intended, to account for detailed behavior of local slip velocities. The Brune model predicts strictly larger stress drops for the rough fault than those actually measured. It is possible that the difference between the rough fault data and the model prediction is related to the substantial amounts of fault creep prior to the stick-slip event which would lead to adjustments in the stress field which would not be included in the measured stick-slip stress drops.

A more complete test of whether the stick-slip data support a rate- and state-dependent friction constitutive model as suggested by Dieterich [1979a] would involve an examination of complete time histories of local shear stress and local slip velocity from the paired transducers deployed along the fault. The local slip velocities increase with increasing local stress drops, and, as reflected by the data in Figure 2.9, the rough fault sustains smaller stress drops than the smooth fault for the same measured stick-slip slip velocity. For the same reasons mentioned earlier, this behavior is generally consistent with a rate- and state-dependent friction model, but, by themselves, the high-frequency stick-slip data are not sufficient to provide any more than a qualitative support for such friction models. It is necessary to include data regarding the local quasistatic fault slip histories to address this question of velocity-dependence further.

2.4.3 Apparent Fracture Energy

As mentioned earlier, observed fault slip weakening may be interpreted in terms of an apparent fracture energy required for continued fault growth, or energy release rate. Preliminary estimates of the apparent fracture energy of stick-slip events generated on a simulated fault appear in Okubo and Dieterich [1981]. A more detailed discussion of the

effects of fault roughness on measured fracture energy is presented here.

A very idealized model of fault slip weakening was introduced by Ida [1972] and later used by Andrews [1976] and Day [1982] in their finite difference calculations of dynamic shear crack propagation. It consists of a linear relationship between shear stress and fault slip, drawn in Figure 2.10, by which the strength of the fault decreases with increasing fault slip. At a critical displacement indicated in the figure as d_r, the fault weakening process is completed and further fault slip takes place at residual stress level τ_r. With this model it is possible to make some simple predictions about the effects of fault roughness and applied normal stress on fracture energy.

Apparent fracture energy is that energy in excess of the work required to promote frictional sliding at τ_r and it is simply the area of the shaded portion of Figure 2.10. Fracture energy G is thus given by:

$$G = d_r (\tau_p - \tau_r)/2 . \qquad (2.3)$$

In a friction experiment, the stress parameters τ_p and τ_r are associated with static and kinetic friction, and the difference $\tau_p - \tau_r$ would be expected to increase with increasing normal stress. Observed values of d_r are insensitive to normal stress but increase with increased fault roughness. Therefore, G is expected to increase both with increasing normal stress and with increasing fault roughness.

Average apparent fracture energies of stick-slip events are determined by averaging local estimates of G made from individual slip-weakening curves. These average G values are plotted in Figure 2.11 as a function of normal stress. The triangles represent the rough fault data and the circles represent the smooth fault data. As seen in this figure, the average apparent fracture energies do indeed increase both with increasing normal stress and with increasing fault roughness, consistent with the prediction made above. The values of G

range from 0.2 J/m^2 to about 2.4 J/m^2. This variability of fracture energy subject to experimental and physical conditions indicates that the apparent fracture energy of stick-slip shear instability, unlike tensile fracture, is not a material property, and should not be confused with specific surface energy. While surface energy is undoubtedly a component of the apparent fracture energy, its actual effect in shear faulting has not been clearly established. Therefore, published values for the surface energy of rocks and minerals [*e. g.*, Brace and Walsh, 1962; Friedman *et al.*, 1972] are perhaps best used only to establish bounds for the actual energy requirements of shear failures and earthquakes.

Recent estimates of G have been provided by Rice [1980], Wong [1982, 1985] and Wang *et al.* [1985]. These estimates are also based on an integration of post-failure stress-vs-fault slip records from quasistatic and dynamic shear failure of rock samples. The experiments from which these estimates are taken are conducted on small test samples in triaxial testing machines at relatively high normal stresses (*i. e.*, confining pressures up to 470 MPa). Measured G values range from 1×10^4 to 5×10^4 J/m^2, and these values are qualitatively consistent with fracture energy which increases with increasing normal stress. A linear extrapolation of the fracture energy measurements presented in this thesis would predict, for these elevated normal stresses, G of the order of 400 J/m^2. This linear extrapolation would not necessarily incorporate a presumed greater amount of surface damage sustained under elevated normal stress conditions. Wong [1985] has shown that a logarithmic normal stress dependence of G might be more reasonable.

2.4.4 Rupture Velocity

With the 2-m-long fault and the high-speed sampling system for the local shear stress records, it is possible to measure the apparent rupture speed of the stick-slip event as it propagates between strain gage locations. At a sampling rate of 200,000 Hz, the timing accuracy for the onset of stick-slip is 5 μs. The rupture velocities that are discussed below

are determined by dividing the strain gage separation distance by the difference between times of stick-slip initiation. Therefore, these velocities are an average of the apparent rupture propagation speeds between strain gages.

Apparent rupture velocities for stick-events generated at different normal stresses are plotted in Figure 2.12. Only those rough fault data which allowed a fairly unambiguous estimate of the onset times of stick slip at a strain gage are included. In some cases, one end of the fault would display very gradual decreases in stress, suggesting a creep-to-stick slip transition or nucleation, so that the onset of slip during the stick-slip event would be difficult to identify. Stick-slip records from the smooth fault all clearly display the onset of the event. (See, for example, the records in Figure 2.3.) In order to eliminate some of the more obvious two-dimensional rupture propagation effects from these data (*i. e.*, rupture fronts that do not propagate uniformly parallel to the strain gage array), an arbitrary cutoff is applied such that apparent rupture velocities measured from the gages nearest to that which first registered the stick-slip stress drop are not included. At each normal stress a wide range of rupture velocities is observed. Rupture velocities on the smooth fault are almost exclusively larger than those on the rough fault measured at the same normal stress. Representative rupture velocities are between 2.5 and 4 km/s for the smooth fault and 0.5 and 1.5 km/s for the rough fault. The rough fault apparent rupture velocities also exhibit a slight tendency to increase with increasing normal stress, although the variation in rupture velocity at a single normal stress is at least of the same magnitude as this increase with increasing normal stress. This tendency in the smooth fault data is not perceptible.

Numerical modeling of a slip-weakening fault [*e. g.*, Andrews, 1976; Day, 1982] shows that a propagating instability will accelerate from a slowly expanding nucleation stage toward terminal rupture speeds as the area of failed fault surface increases. Thus, for a single stick-slip failure (*i. e.*, one normal stress) it would be expected that a range of rupture velocities would be observed, depending on the rate at which the rupture accelerates to its

terminal rupture speed. In Figure 2.13, apparent rupture velocities are plotted as a function of fault propagation distance. The measured rupture velocity is regarded as the rupture velocity of the stick-slip event as it passes the midpoint between two adjacent transducers. The propagation distance is measured from the strain gage with the earliest stress drop to these midpoints. Again, there is a clear distinction between the rough fault data (triangles) and the smooth fault data (circles). Not only is the difference between the magnitudes of the rough and smooth fault rupture speeds observed, but the smooth fault data and the rough fault data also exhibit different propagation distance effects. While the rough fault rupture velocities increase as the rupture area grows, showing the acceleration of the rupture front expected from the theoretical and numerical results, the smooth fault data show no such increase of rupture velocity with distance. Because the smooth fault rupture velocities are in the range of the seismic wave speeds of the granite, it migh be reasonable to suggest that the stick-slip events on the smooth fault have achieved their terminal rupture speeds.

Although this approach to the data is diferent from that taken by Johnson and Scholz [1976], who characterize a stick-slip event by a single rupture speed, there are some similarities between these data and those summarized in their work. Johnson and Scholz [1976] note that the rupture velocity of stick-slip events on Westerly granite surfaces is reduced when gouge material is introduced onto the sliding surface and that the stick-slip rupture velocity over the gouge-covered surface increased with increasing stress drop. They also note that stick-slip events propagate over the gouge-free surface at a speed which is essentially the shear wave speed. In the sense that both the introduction of fault gouge onto the sliding surfaces and an increased fault roughness increase the critical slip-weakening displacement d_r required to drop to residual sliding stress [Dieterich, 1981b and this thesis], the observations of lower rupture velocity on the rough fault agree with the Johnson and Scholz [1976] results. Because d_r is dependent on the physical character of the sliding surfaces, rupture velocity predictions for stick slip on surfaces in different rock types should

take into account not only the seismic wave speeds in the materials but also the fault surface condition.

The theoretical role of rupture velocity in the partitioning of energy during dynamic crack propagation has been reviewed, for example, by Freund [1979]. Husseini [1977] provides an interpretation of the Johnson and Scholz [1976] rupture velocity data in terms of an energy budget. Assuming that fracture energy is constant, he suggests that the observed increase in rupture velocity with increasing stress drop arises directly from the increase in the radiation efficiency of the dynamic rupture with increasing stress drop. However, as discussed in an earlier section of this chapter, apparent fracture energy increases both with increasing d_r and with increasing normal stress or stress drop. Therefore, the assumption of constant fracture energy, independent of stress drop, made by Husseini [1977] is not appropriate for stick slip on simulated faults. An alternative explanation for the increase in rupture velocity with stress drop can be based on a fault length scaling parameter which decreases with increasing stress drop.

2.5 Length Scaling of Stick-Slip Data

Up to this point, the discussion has focused primarily on the use of the large test samples to provide detailed observations of the stick-slip failure process leading to the determination of source parameters including stress drop and critical slip-weakening displacement. However, as mentioned by Dieterich [1981a], an important aspect of large-scale geophysical experimental work is the possible resolution of scale-related effects which is generally unattainable under laboratory conditions because of sample size restrictions. A complete understanding of the scaling problem and of how the laboratory results can be applied to earthquakes and natural faults would depend on the analysis of the size of the endzone with respect to the sample or fault size as discussed by Rice [1980]. However, to illustrate one possible length scaling, consider the rupture velocity data

summarized in Figures 2.12 and 2.13.

A comparison of smooth and rough fault apparent rupture velocities as in Figure 2.13 suggests that the process of rupture acceleration to a terminal rupture velocity occurs over different fault propagation distances or fault lengths. The rough fault stick-slip events accelerate with increasing fault length, yet the last measured rupture velocities remain significantly below the shear wave speed of the Sierra granite used in the tests. As plotted in Figure 2.13, the smooth fault stick-slip data do not appear to show this same distance effect and the rupture speeds are scattered about the seismic wave speeds. This suggests that stick slip on the smooth fault can nucleate and achieve rupture speeds scattered about a terminal rupture velocity over fault dimensions which are less than the total length of the simulated fault. Over these same absolute rupture dimensions, stick-slip events on the rough fault cannot achieve the same terminal rupture speeds.

The observed fault slip weakening and critical displacement parameter d_r require that consideration be given to length scales and characteristic lengths in analysing the stick-slip data. In general, when considering unstable fault propagation effects, a relevant scaling length arises in the form of L_c given in equation (2.1). Both normal stress, or stress drop, and d_r are present in L_c. In general, L_c values are larger for the rough fault stick-slip events due to the d_r dependence and the smaller stress drops measured for these events. It should also be noted that L_c values for these stick-slip events as estimated from equation (2.1) are probably overestimates of any actual critical fault length because the effects of finite sample size are not accounted for in (2.1).

In Figure 2.14, apparent rupture velocity is plotted as a function of distance normalized by critical fault length L_c. As expected, the rough fault data scale completely into a very short normalized distance range, and the trend of increasing rupture velocity with increasing, this time, normalized fault propagation distance is still observed. The higher rupture velocities for the smooth fault stick-slip events are now associated with larger fault

propagation distances. When the smooth and the rough fault data are considered together, as in Figure 2.14, these observations suggest that the apparent rupture velocities of stick-slip events increase with increasing fault length. The numerical dynamic crack models of Andrews [1976] and Day [1982] predict similar rupture acceleration.

Maximum slip velocities, corrected for local stress drops, recorded at individual transducers are plotted in Figure 2.15 as a function of normalized fault length. Data from a single event are connected with straight line segments. At small propagation distances these data show scatter that are probably related to two-dimensional rupture propagation effects. At larger distances, consistent increases in maximum slip velocity with increasing fault length are observed. On smaller scale fault models for which fault motion is typically equated with relative displacement of the loading rams, these variations in local slip velocity are not observable. Nor are they included in the Brune model because that model does not include rupture propagation. Such increases are predicted by other theoretical models [Andrews, 1976; Day, 1982].

2.6 Summary

These experimental studies of stick-slip failures produced on simulated faults yield results which are consistent with observations of frictional sliding and stick slip from experiments performed with smaller test samples. As observed by Dieterich [1978a, 1979a] for the case of quasistatically imposed changes in the rate of frictional sliding of rock samples, the transition from one sliding state to the next is characterized by a critical slip-weakening displacement d_r. The general behavior of d_r for stick-slip events is the same as that for the quasistatic sliding, namely, that d_r is insensitive to normal stress acting on the fault at the time of the stick-slip event and that d_r values are larger on a roughly lapped sliding surface than on a smoothly lapped sliding surface. Stick-slip stress drops are directly proportional to normal stress, over the range of normal stress used in these experiments.

The constant of proportionality between stress drops and normal stress is approximately 0.05. The fault slip-weakening behavior and stress drops qualitatively support a rate- and state-dependent constitutive friction model proposed by Dieterich [1978a, 1979a] which was motivated by his observations of quasistatic sliding experiments.

Dieterich [1981b] studied in greater detail the effects of varying fault conditions on the critical slip-weakening displacement parameter d_r. Values of d_r which ranged over two orders of magnitude (from 2 to 200 μm) were observed for sliding surfaces which were ground to varying degrees of roughness and with simulated fault gouge layers. Because even the roughest of these simulated faults and the coarsest of these fault gouge layers still represent extreme idealizations of natural faults, it is possible only to speculate about d_r values which would be appropriate for slip on natural faults. The additional complexity that might be expected on natural faults could lead to heterogeneous roughness with maximum or effective values of d_r far greater than the largest values reported by Dieterich [1981b].

Recent efforts to provide a common interpretation to laboratory and field fault mechanics observations have incorporated the fracture energy interpretation of fault slip-weakening models, and they find that the laboratory measurements of fracture energy are one hundred to one thousand times smaller than the values of G determined for earthquakes using a number of different approaches [Rice, 1980; Wong, 1982 and 1985]. The comparison of the laboratory data to the inferred estimates of earthquake or fault fracture energy could be of limited application because the laboratory experiments may not conform to the conditions on natural faults, in particular, those related to the scale of yielding or size of cohesive end zone. If the difference between laboratory and field estimates of G is attributed solely to different values of d_r, then appropriate values of d_r for natural faults could be as large as 1 to 10 cm for some events.

Observations of fault slip weakening at the onset of stick-slip frictional instabilities point out that length scales or characteristic lengths are important aspects of dynamic fault

modeling. In this chapter, a length scaling based on a critical fault length concept was applied to fault propagation data. Normalization of fault lengths according to this scaling led to the observation that both rupture velocity and peak slip velocity increase as a function of fault length. The scaling length is also useful in providing a consistent analysis for stick-slip data obtained from different laboratory apparatuses.

Table 2.1 - Profile locations and rms-heights.

Profile	Fault	x_0(in)	y_0(in)	direction	z_{rms}(μm)
A	smooth	73.25	14.0	+X	1.57
B	smooth	73.25	11.0	+X	1.80
C	smooth	73.25	9.0	+X	1.64
D	smooth	12.48	8.1	+X	0.92
E	smooth	36.48	8.1	+X	1.53
F	smooth	51.13	8.1	+X	1.12
G	smooth	63.33	8.1	+X	2.18
H	smooth	24.35	8.1	-Y	1.15
J	smooth	36.48	8.1	-Y	1.66
K	rough	19.69	10.5	+X	23.51
L	rough	29.53	10.5	+X	11.87
M	rough	39.37	10.5	+X	12.93
N	rough	59.06	10.5	+X	16.14
P	rough	66.14	4.5	+X	3.73

Figure Captions

Figure 2.1 . Sketch of large-scale testing machine with rock sample in place. Sample dimensions are 1.5 x 1.5 x 0.4 m . Different types of transducers are shown. Point at end of upper surface of block on fault is taken as (0,0). Positive x- and y-directions specified to go into rock.

Figure 2.2 . Fault profiles. a. Profiles from smooth fault in the direction parallel to the direction of fault slip. b. Profiles perpendicular to fault slip direction. c. Rough fault profiles parallel to fault slip direction. d. Rough fault profile from location specially selected for comparison with smooth fault.

Figure 2.3 . High frequency stick-slip data from events generated at σ = 3.45 MPa. a. Event generated on smooth fault. b. Event generated on rough fault. Numbers along the left borders represent transducer locations measured in mm from one end of fault. Vertical arrows indicate approximate times of onset and termination of stick-slip sliding. S : shear stress; D : displacement.

Figure 2.4 . Slip-weakening curve from rough fault obtained from local shear stress and displacement records. Original stress and slip records are shown in lower plot.

Figure 2.5 . a. Smooth fault slip weakening curves. b. Rough fault slip weakening curves. Curves A are from events generated at σ = 1.38 MPa, curves B at 2.76 MPa, and curves C at 3.45 MPa .

Figure 2.6 . Critical slip weakening displacement d_r plotted as a function of normal stress. Rough fault data are shown as triangles and smooth fault data shown as circles.

Figure 2.7 . Average stick-slip stress drops plotted as a function of normal stress. The same symbol convention as in Figure 2.6 is used here.

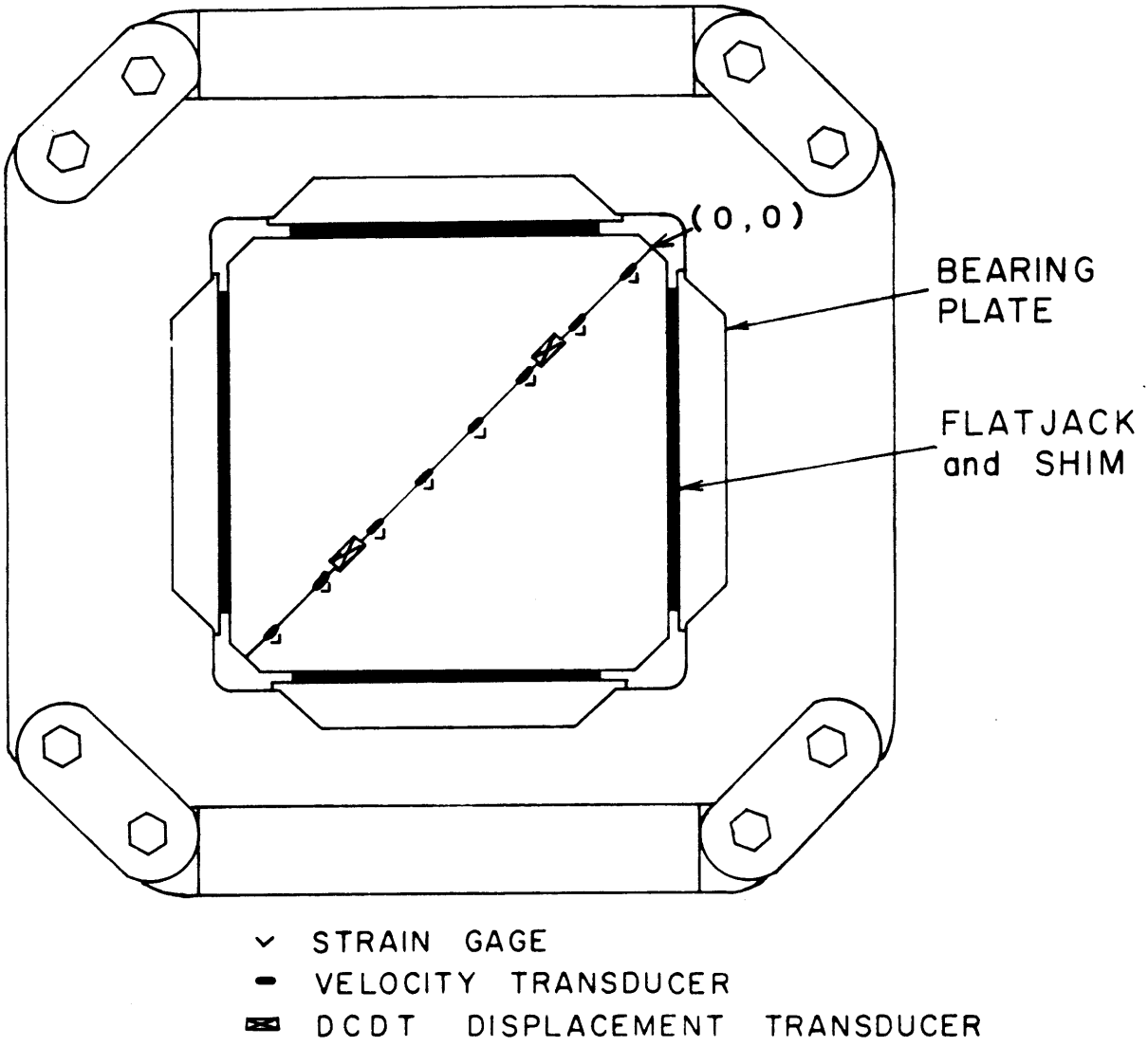
(0,0)
BEARING PLATE
FLATJACK and SHIM
STRAIN GAGE
VELOCITY TRANSDUCER
DCDT DISPLACEMENT TRANSDUCER

Figure 2.1

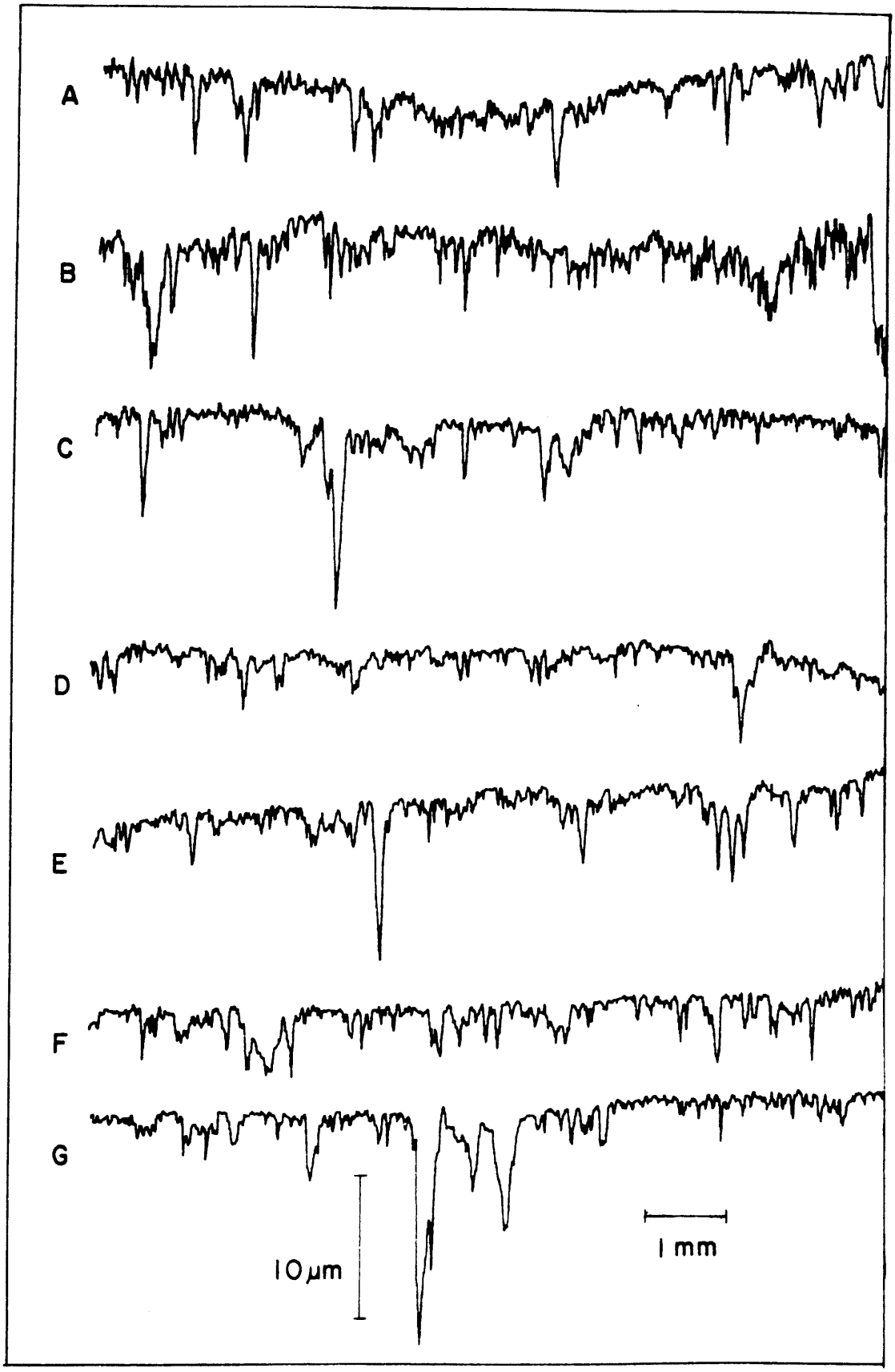

Figure 2.2a

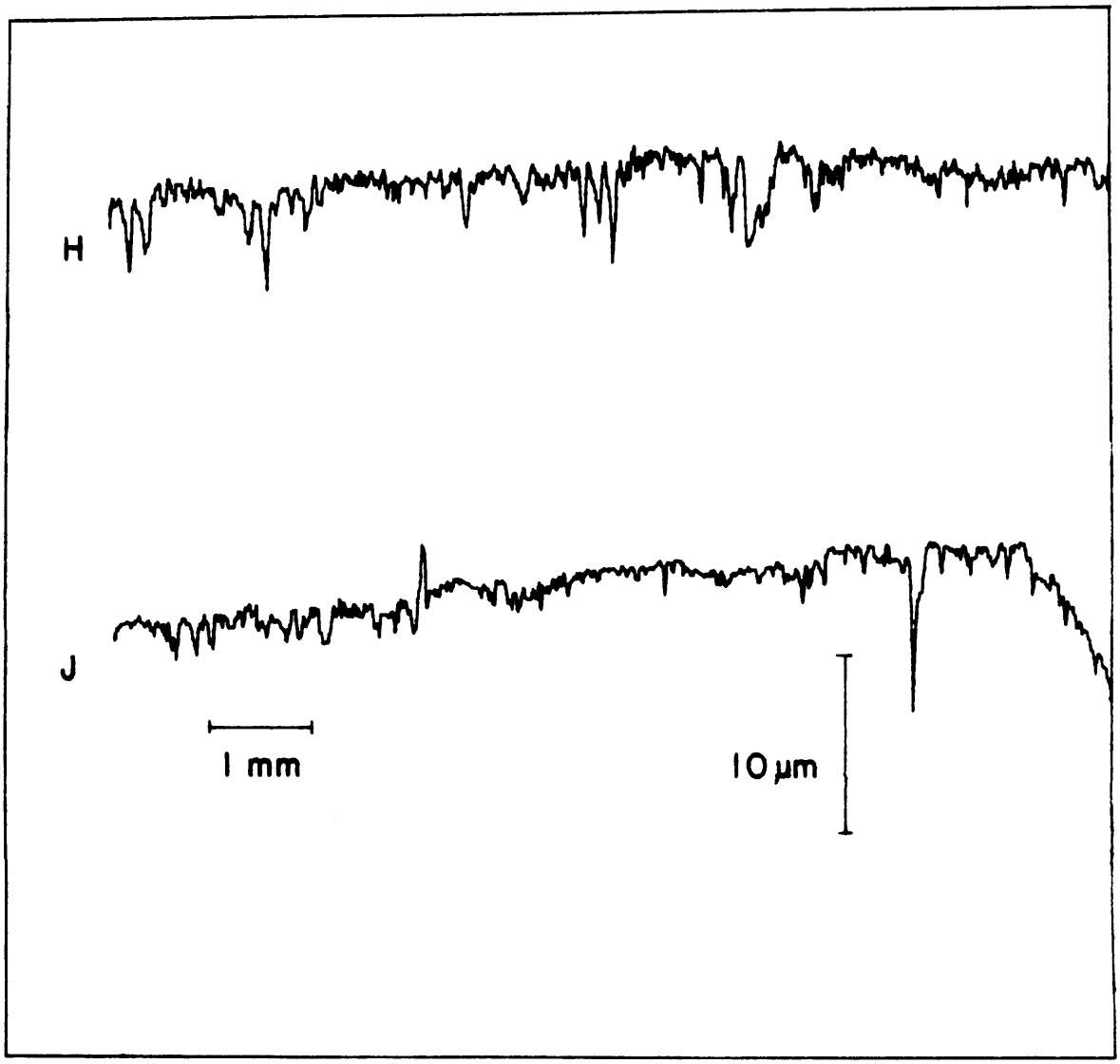

Figure 2.2b

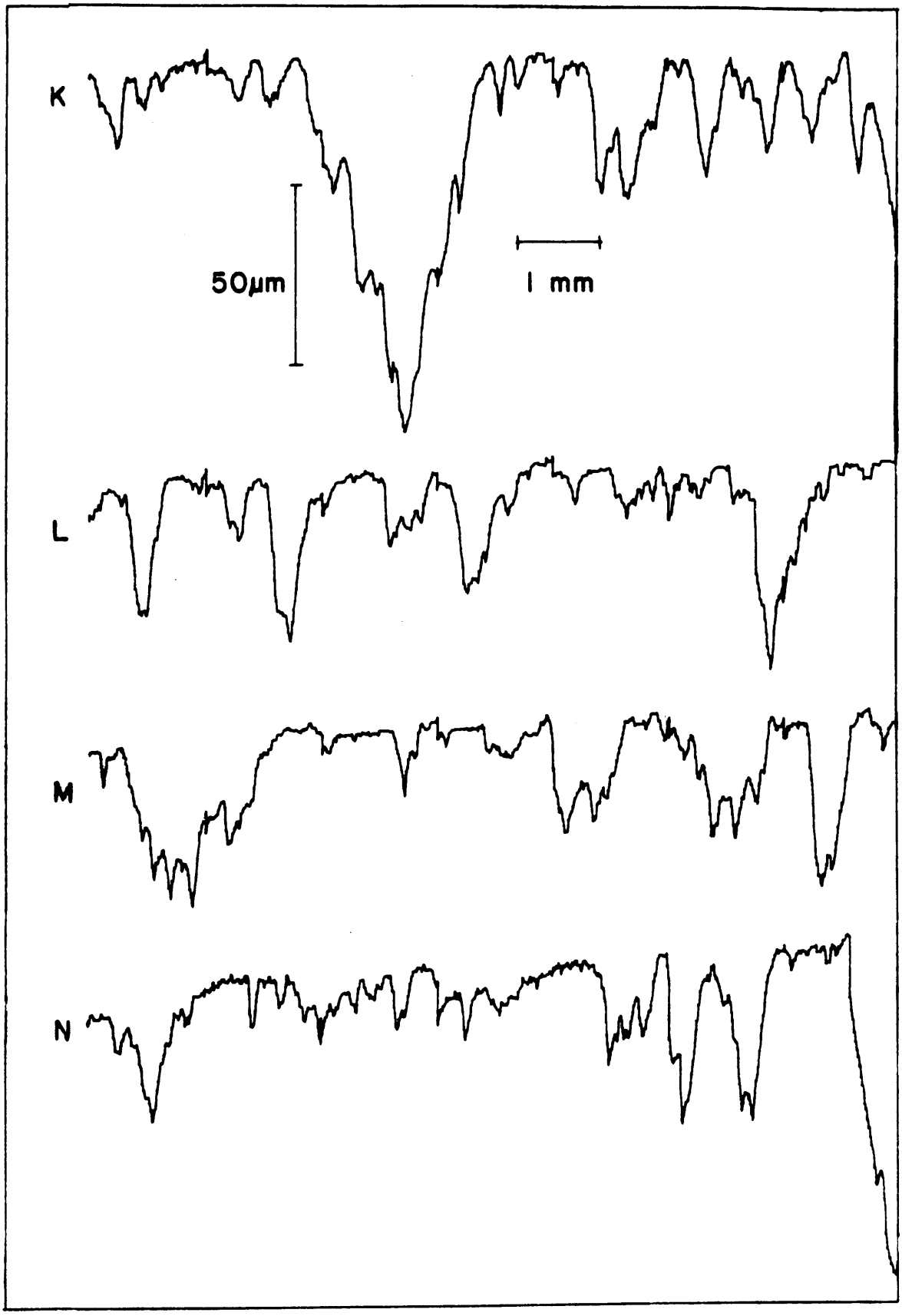

Figure 2.2c

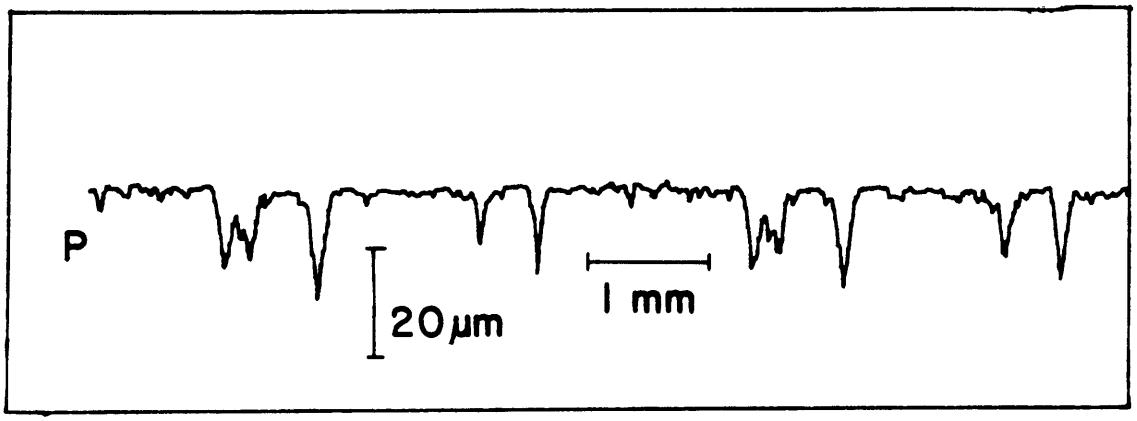

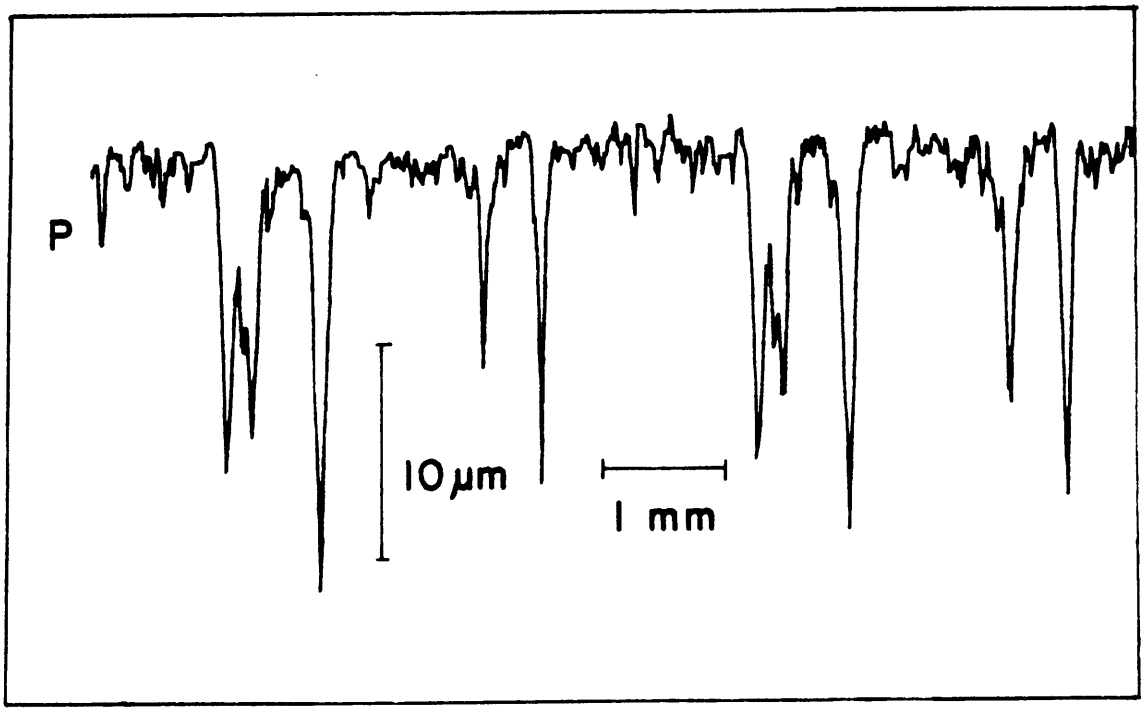

Figure 2.2d

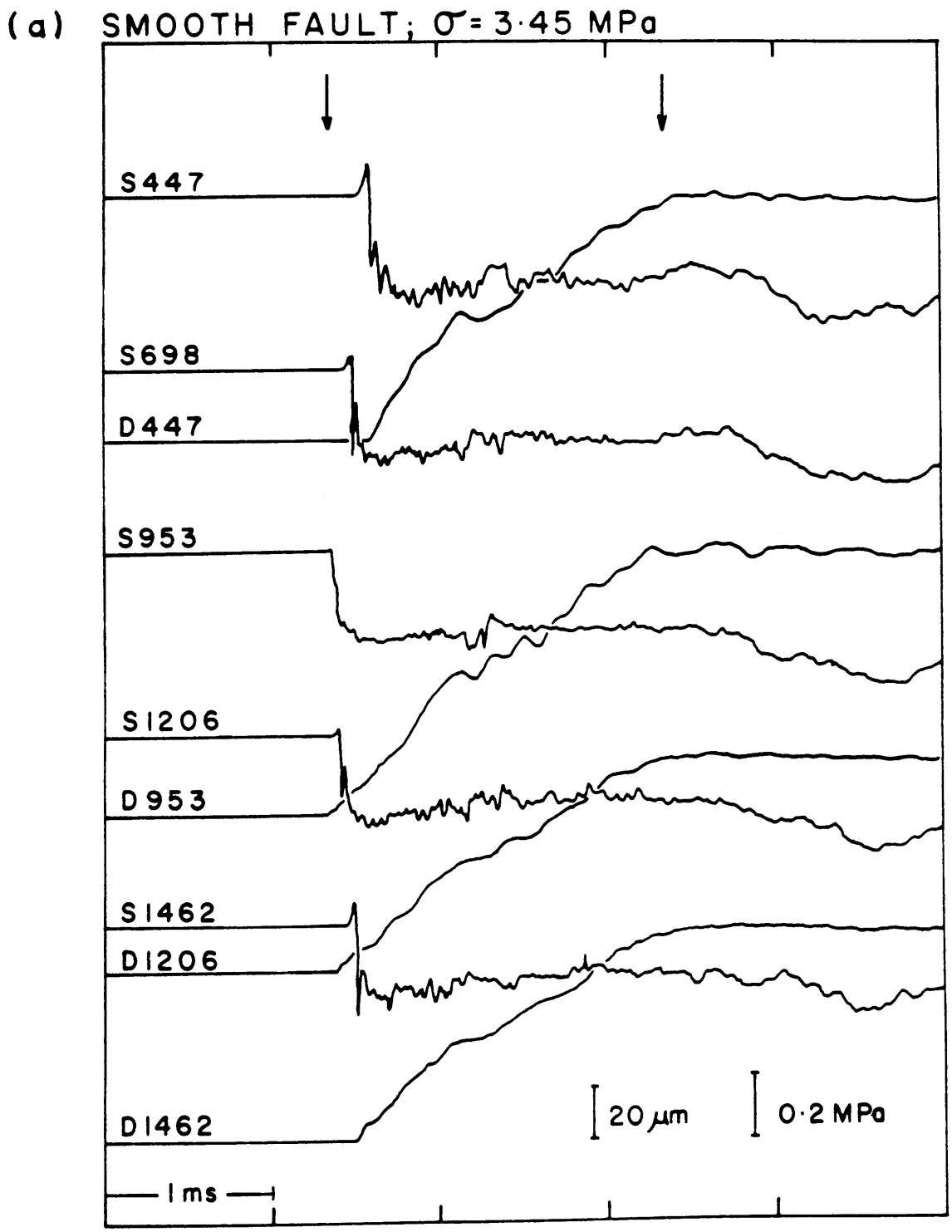
(a) SMOOTH FAULT; σ = 3·45 MPa
S447
S698
D447
S953
S1206
D953
S1462
D1206
D1462
20 μm
0·2 MPa
1 ms

Figure 2.3a

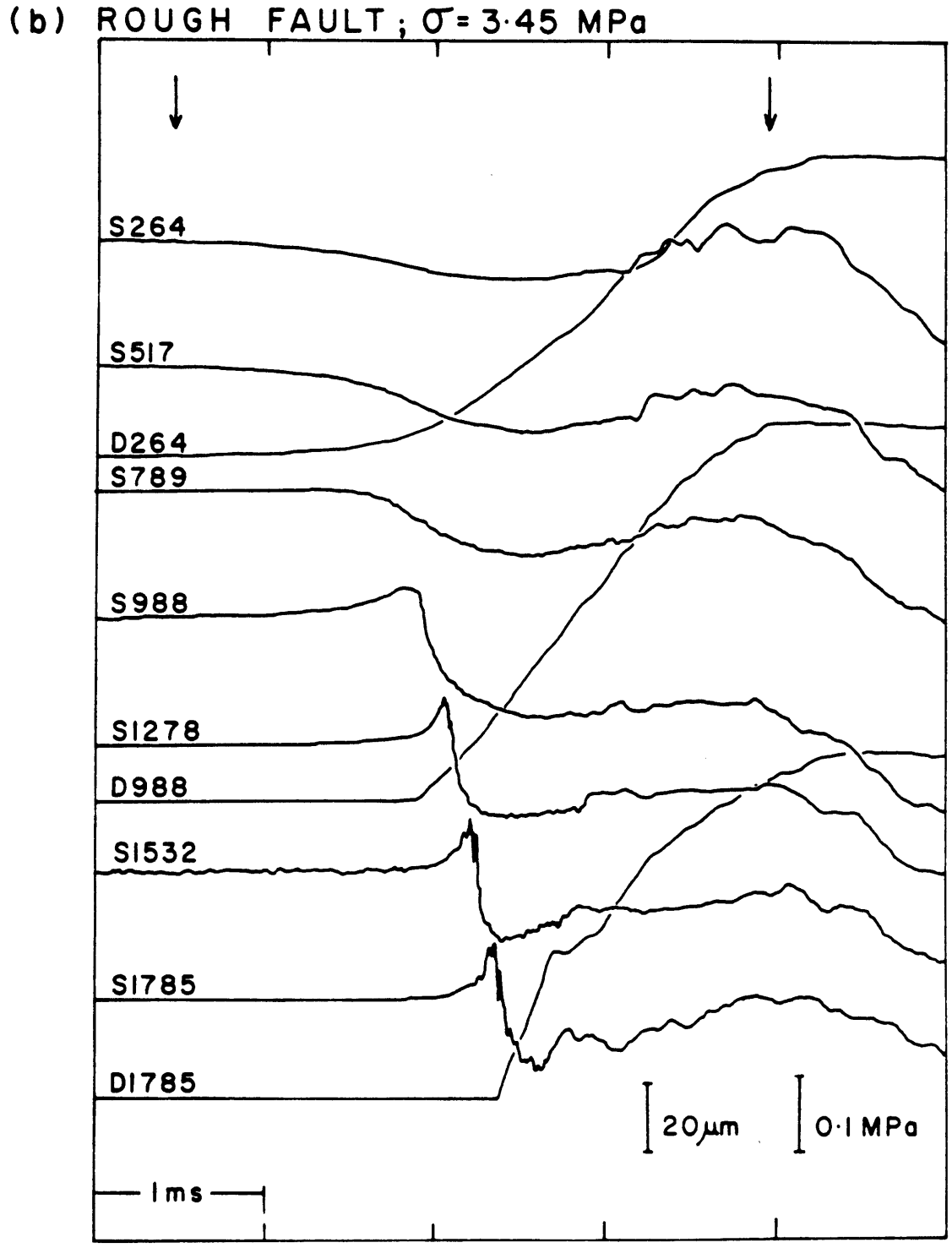
(b) ROUGH FAULT; σ = 3·45 MPa
S264
S517
D264
S789
S988
S1278
D988
S1532
S1785
D1785
20μm
0·1 MPa
1ms

Figure 2.3b

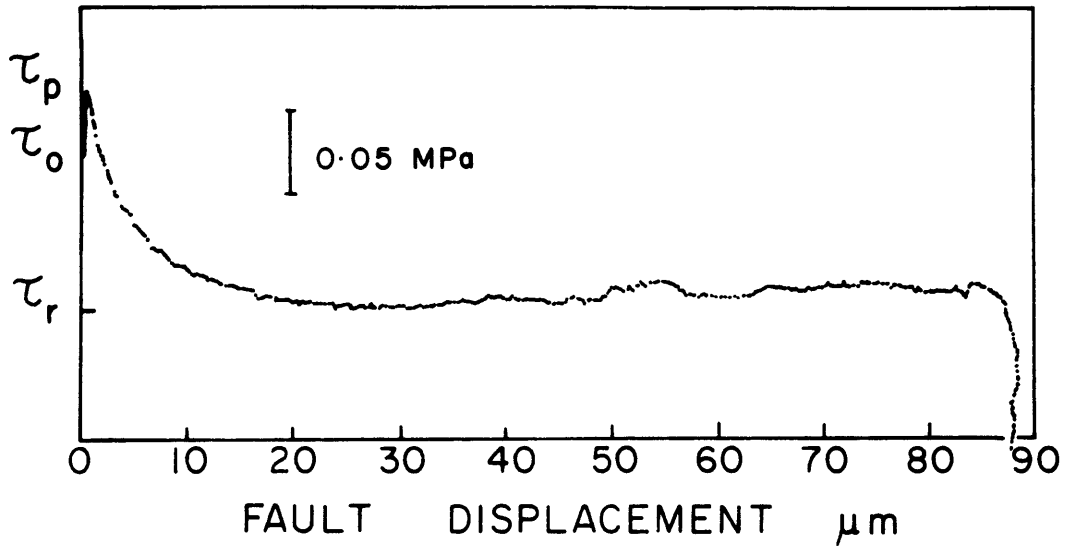
τ_p
τ_o
τ_r
0·05 MPa
0
10
20
30
40
50
60
70
80
90
FAULT DISPLACEMENT μm

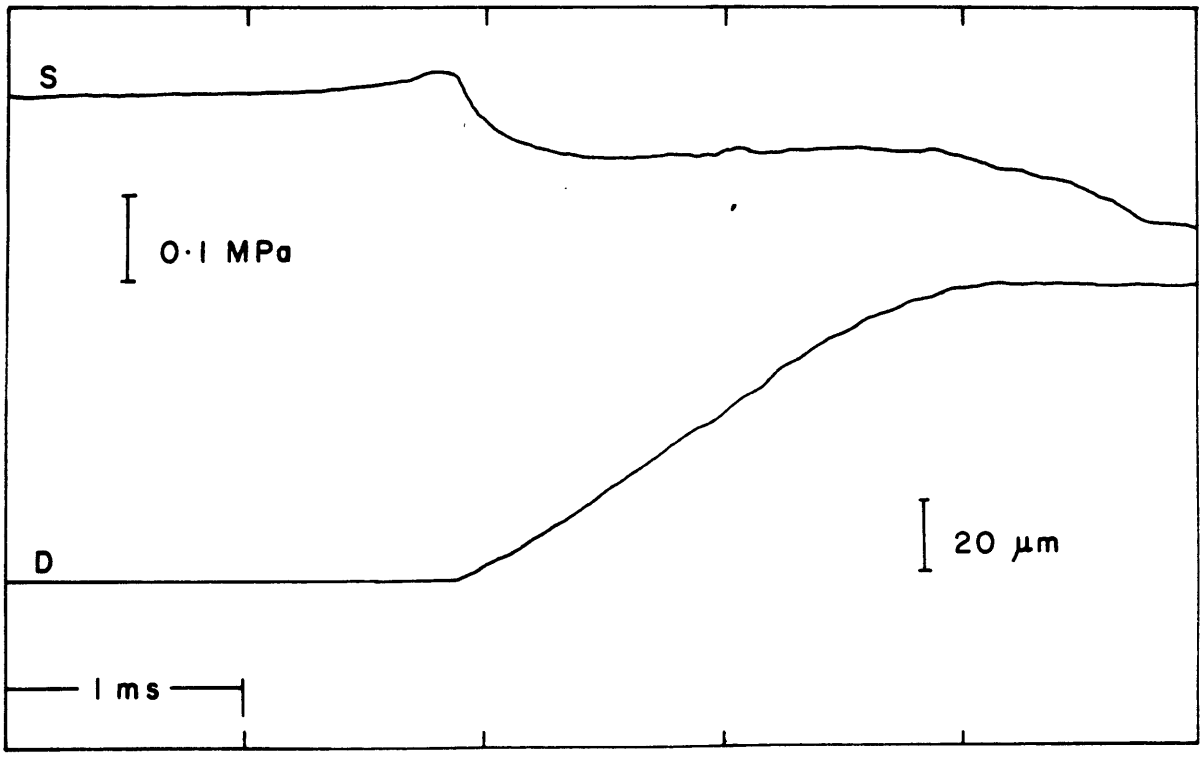
S
0·1 MPa
D
20 μm
1 ms

Figure 2.4

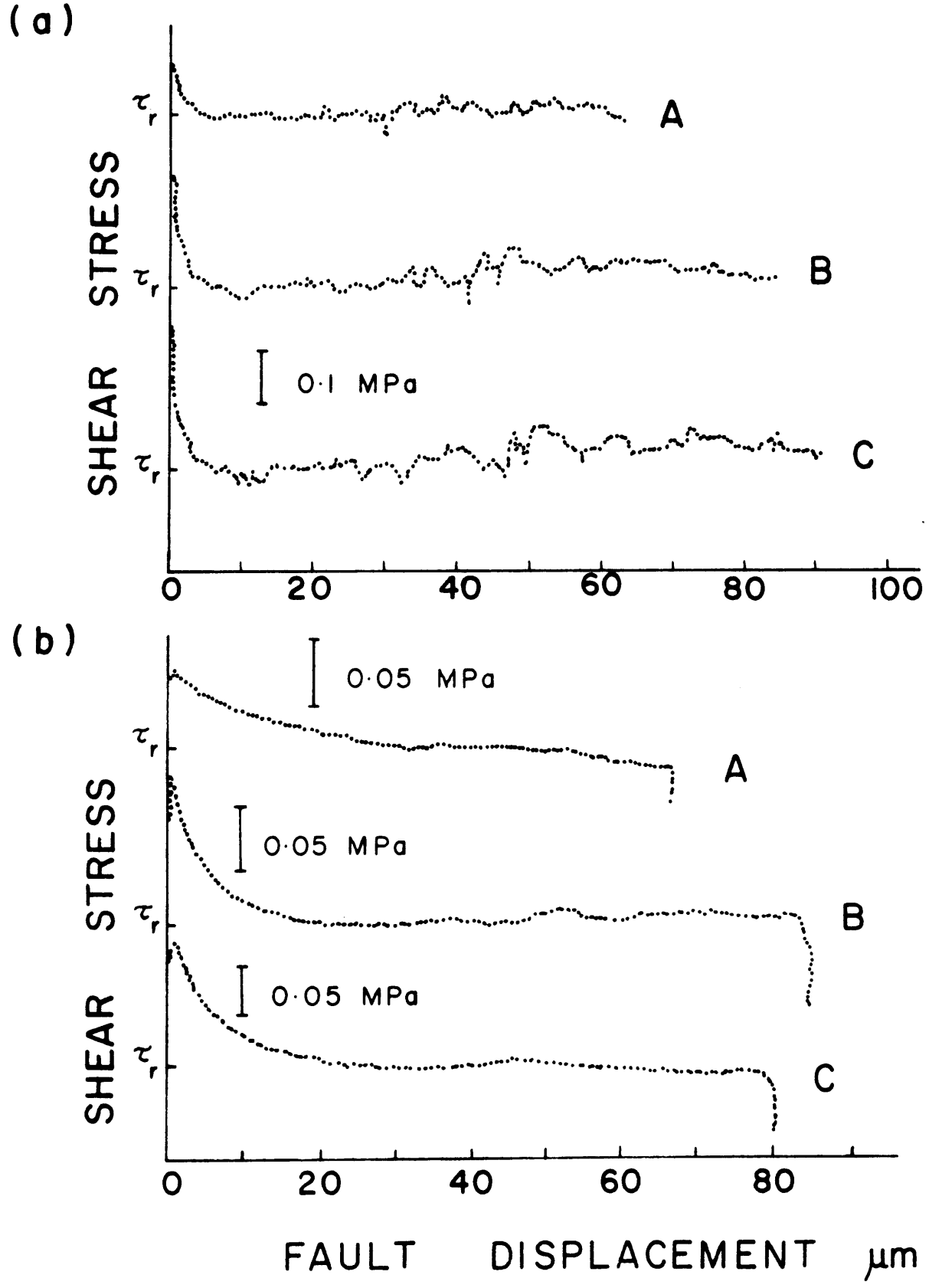
(a)
SHEAR STRESS
τ_r
A
B
C
0·1 MPa
0
20
40
60
80
100
(b)
0·05 MPa
0·05 MPa
0·05 MPa
0
20
40
60
80
FAULT DISPLACEMENT μm

Figure 2.5

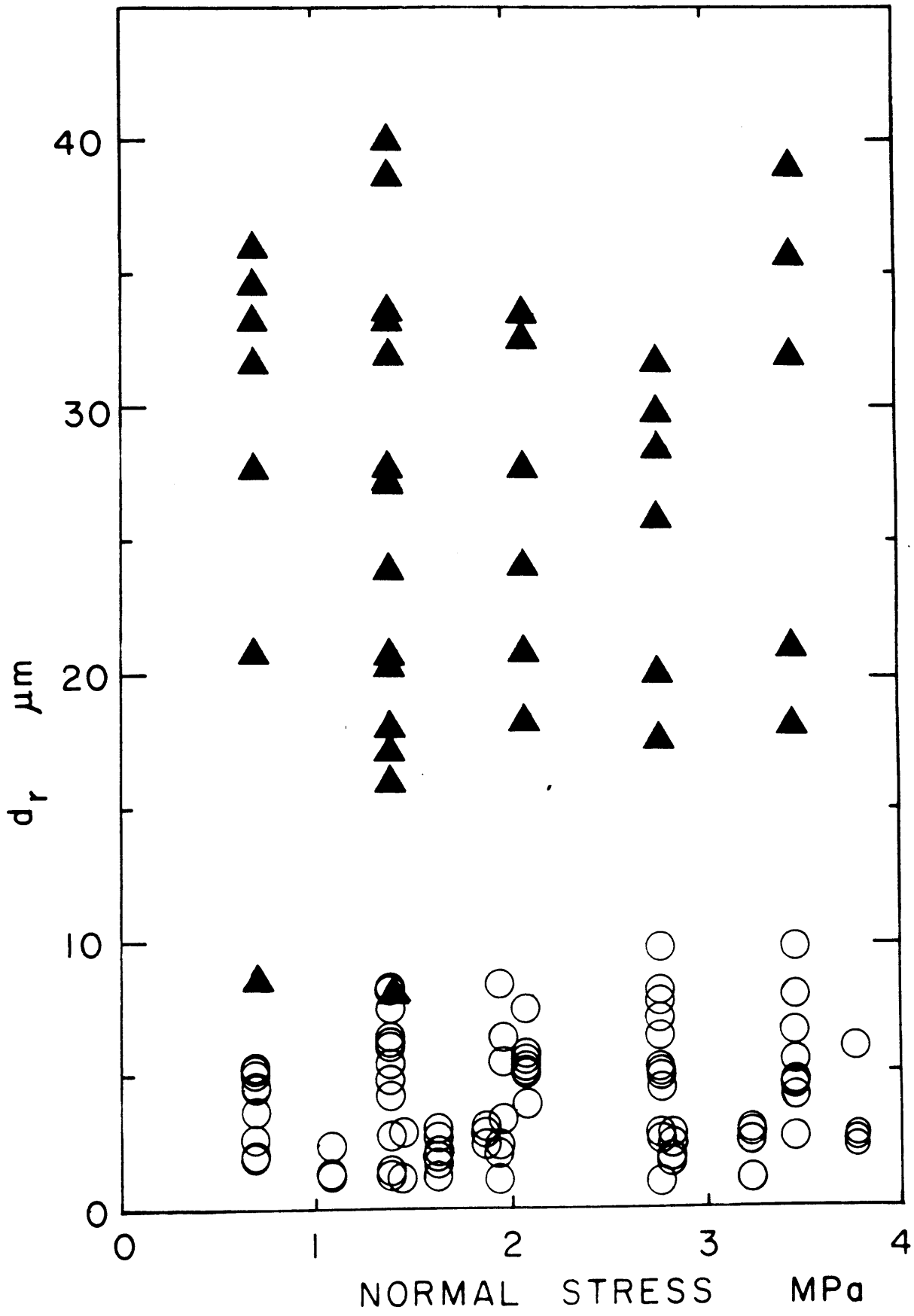

Figure 2.6

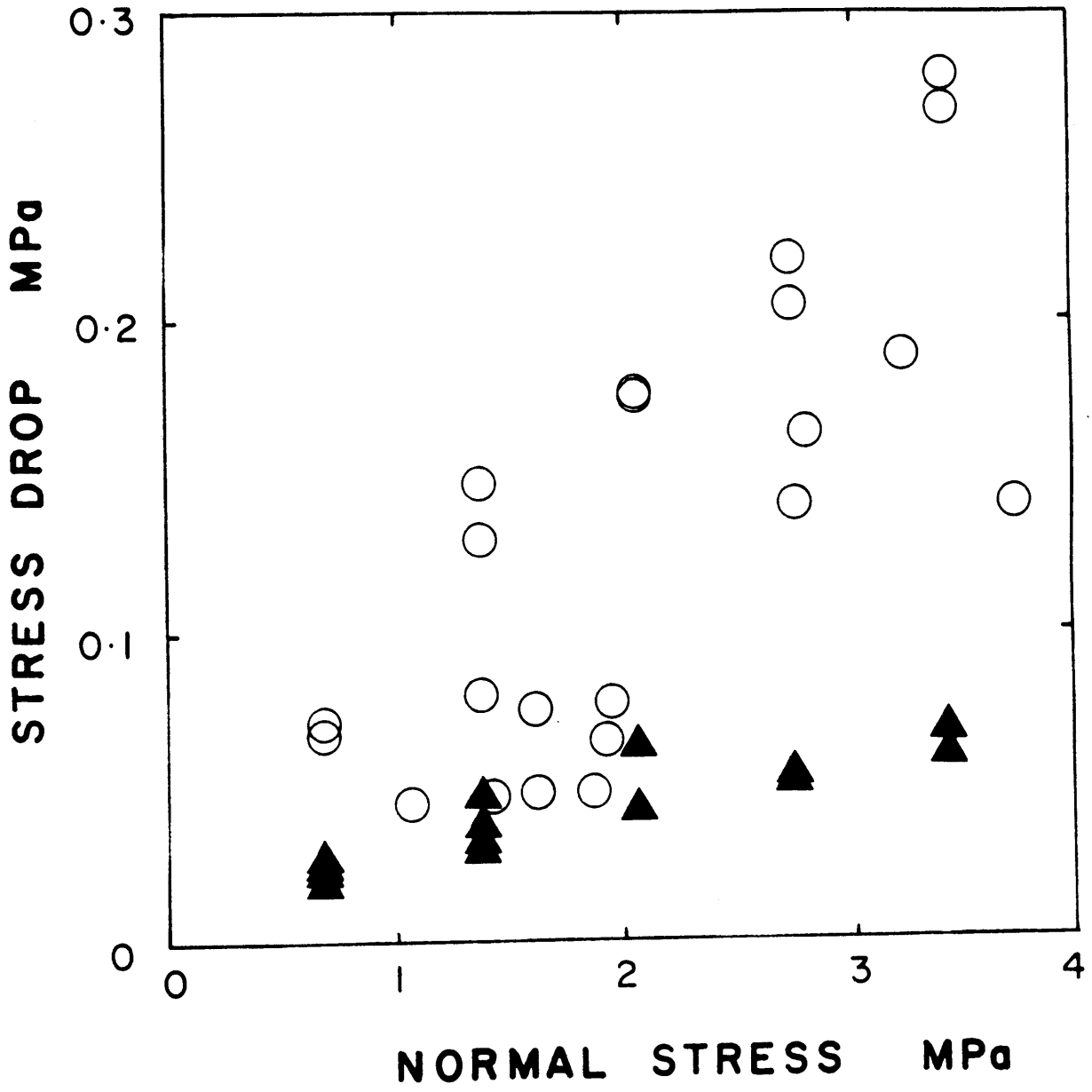

Figure 2.7

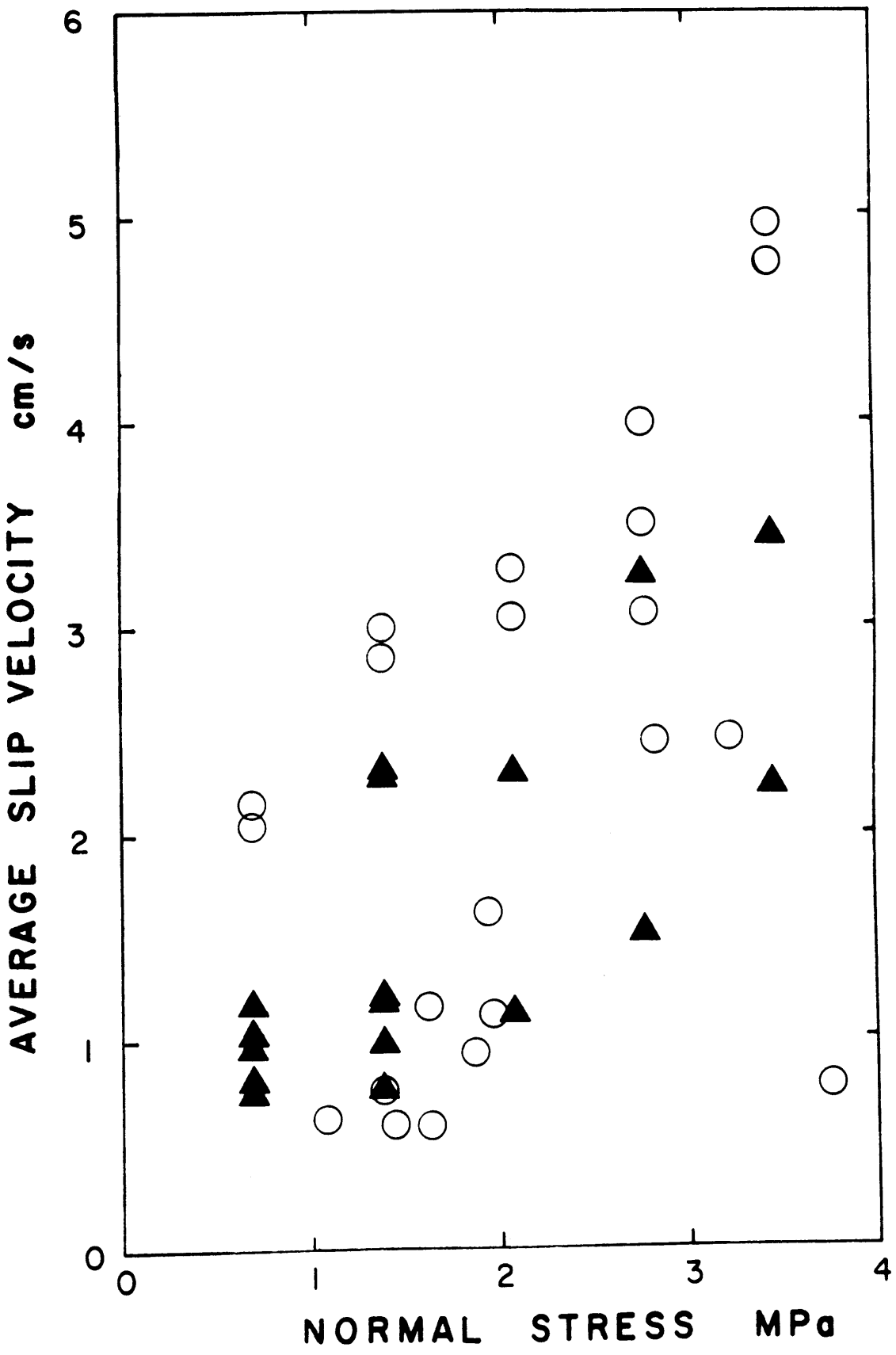

Figure 2.8

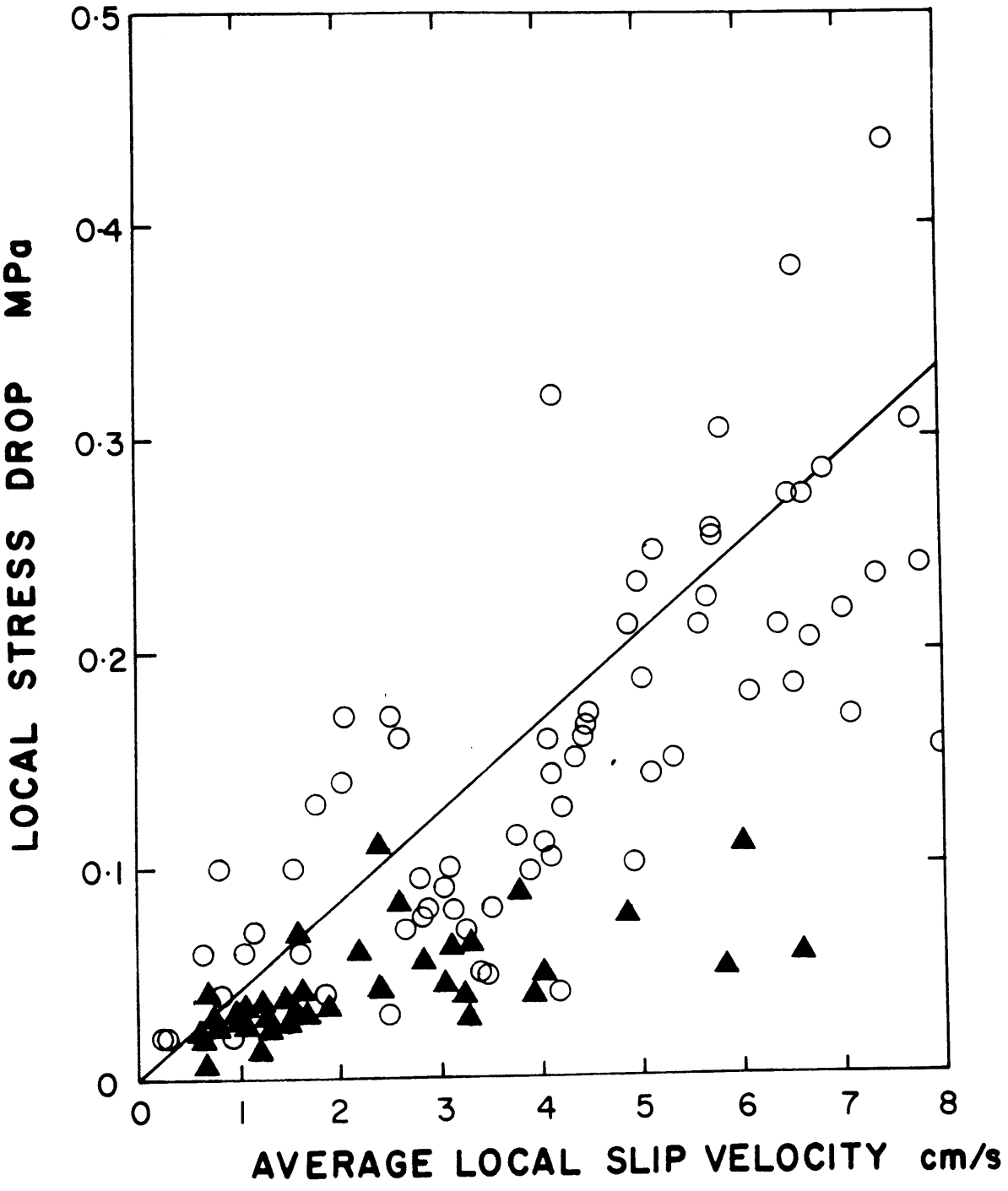
0·5
0·4
0·3
0·2
0·1
0
LOCAL STRESS DROP MPa
0
1
2
3
4
5
6
7
8
AVERAGE LOCAL SLIP VELOCITY cm/s

Figure 2.9

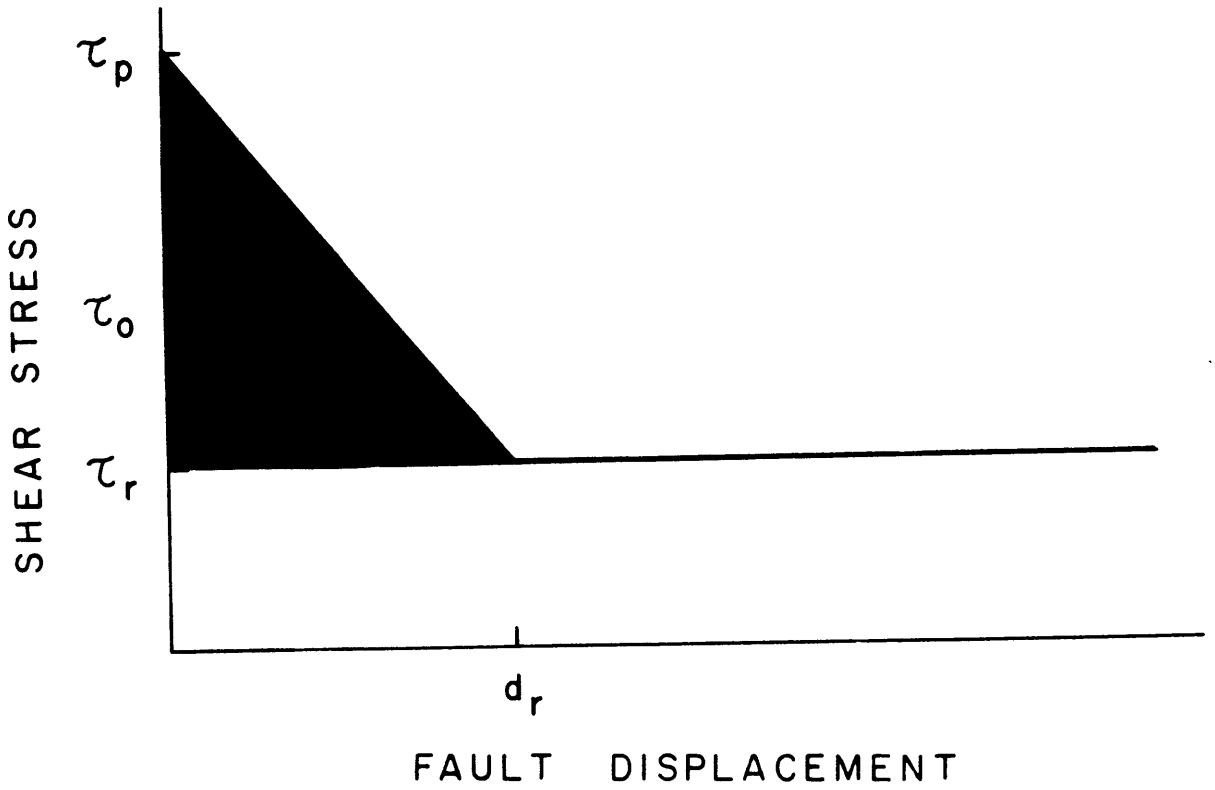

Figure 2.10

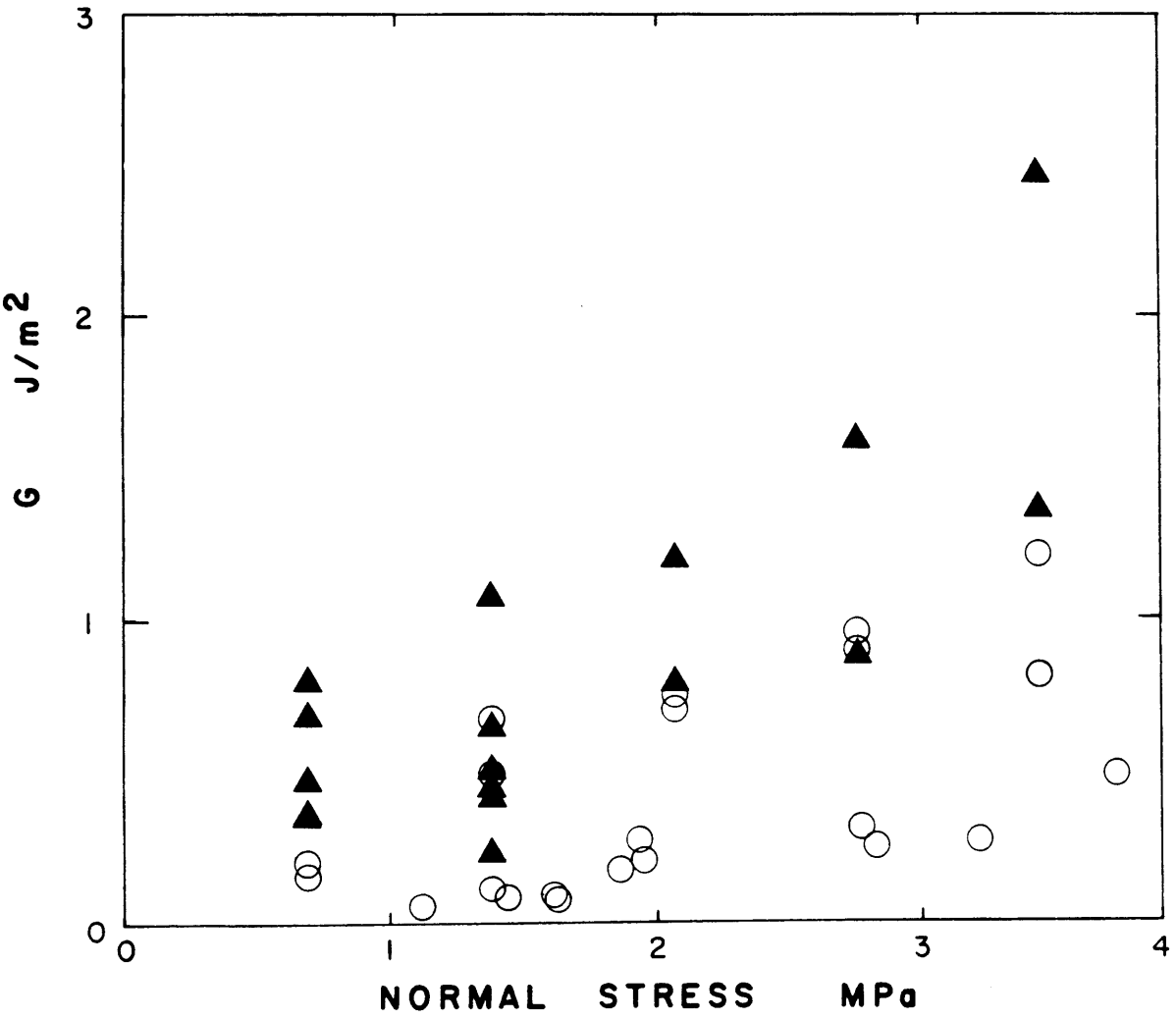

Figure 2.11

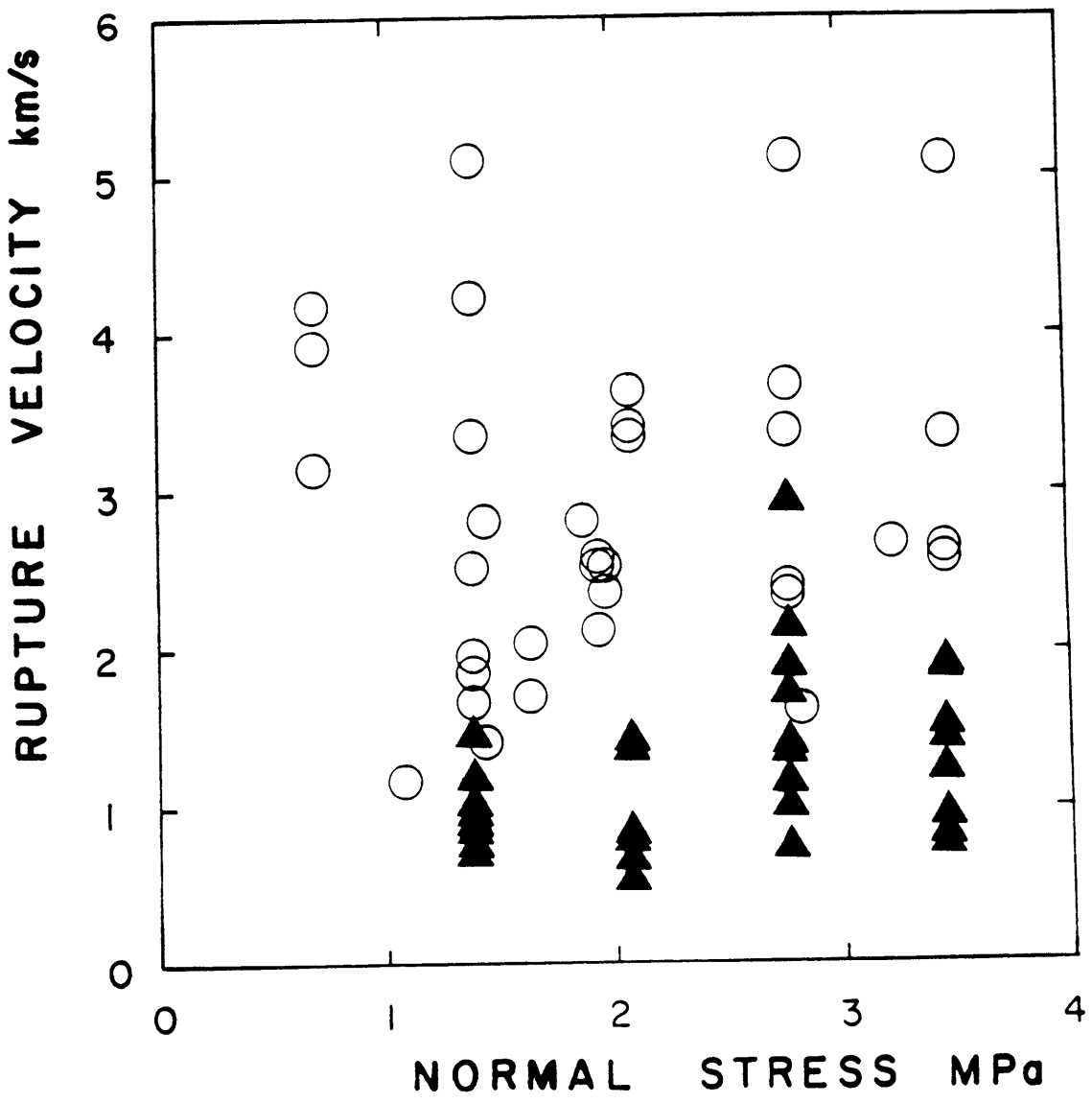

Figure 2.12

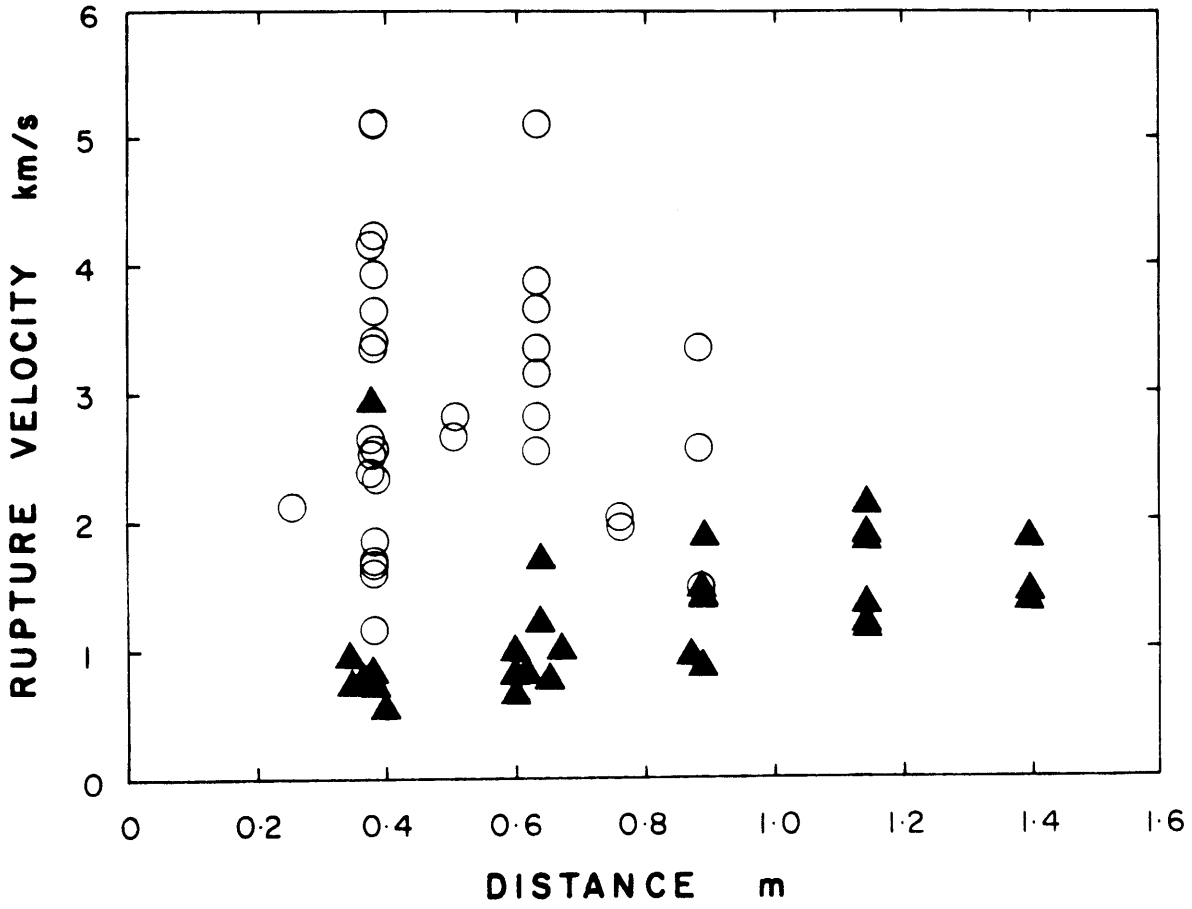
RUPTURE VELOCITY km/s
6
5
4
3
2
1
0
0
0·2
0·4
0·6
0·8
1·0
1·2
1·4
1·6
DISTANCE m

Figure 2.13

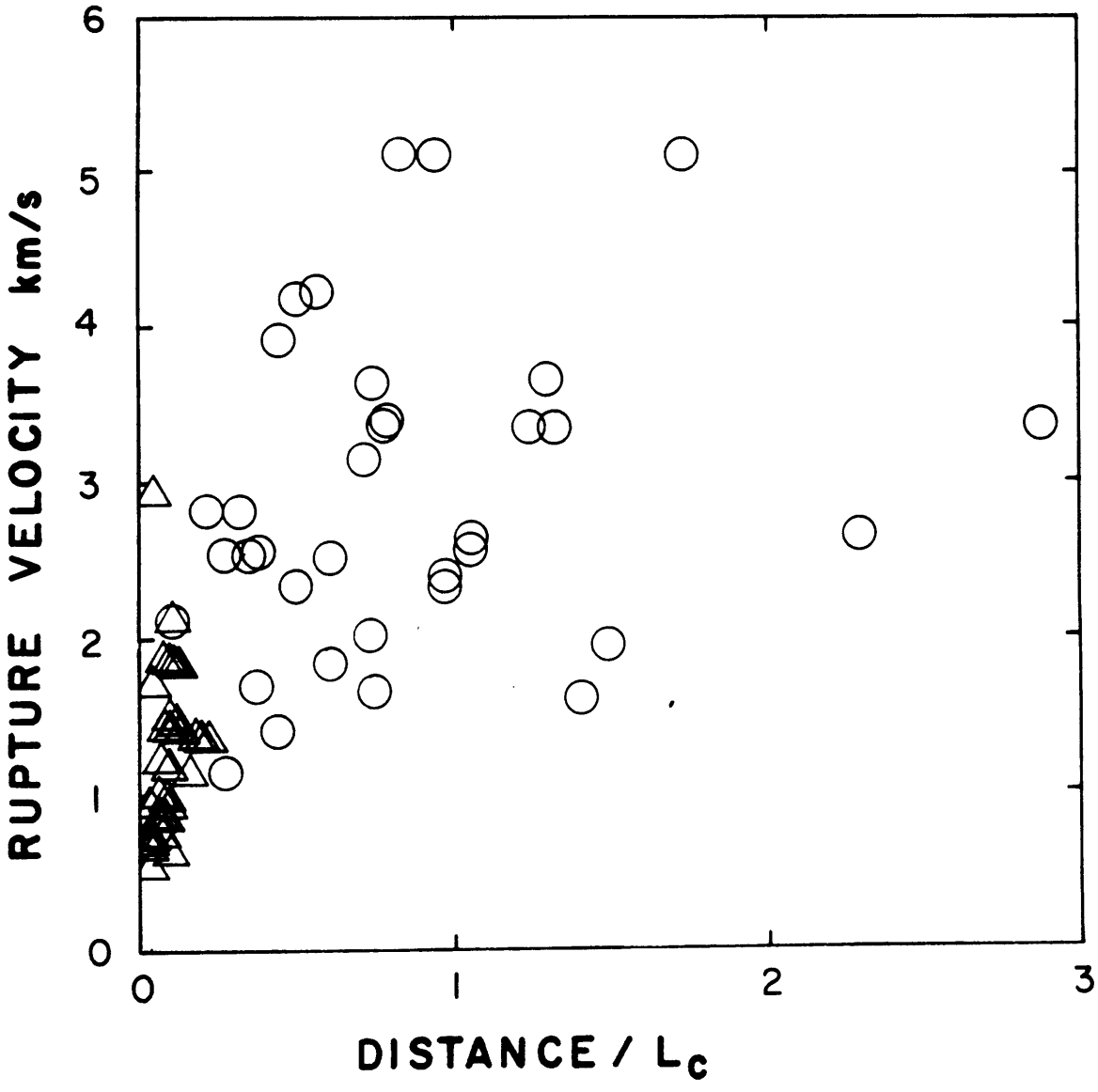

Figure 2.14

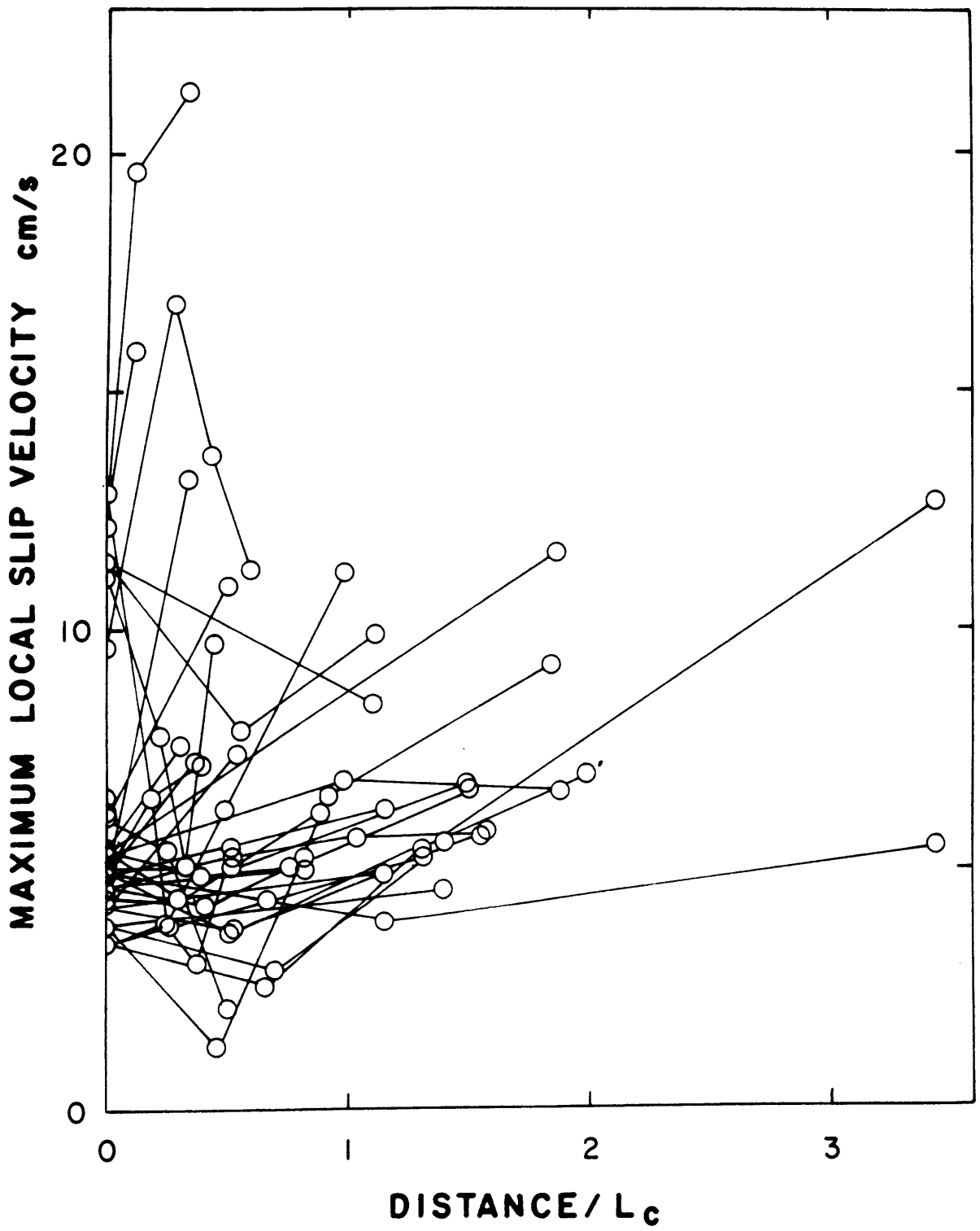

Figure 2.15

Chapter 3 - State Variable Fault Constitutive Relations for Dynamic Slip

3.1 Introduction

Using the concept of a crack-tip cohesive zone introduced by Barenblatt [1959] for tensile cracks, Ida [1972] proposed that earthquake sources be modeled as dynamically supported shear cracks governed by a fault slip-weakening constitutive model. As noted by Ida, this modeling approach allows the use of physically motivated failure criteria in determining details related to the growth of the fault rupture surface without requiring that *a priori* assumptions with regard to the rupture history be made. Cohesive zone models are free of the problem of crack-tip singularities which characterize elastic-brittle solutions for crack tip stress fields. Furthermore, Ida [1973] has used the slip weakening-type of cohesive zone model to determine seismic ground motion parameters and to demonstrate the effects of fault model parameters on ground motion.

Slip-weakening modeling has been extended to investigate shear rupture propagation behavior in two- [Andrews, 1976] and three-dimensional [Day, 1982] dynamic crack simulations using simple linear slip-weakening constitutive models for fault response in finite difference calculations. In particular, Day [1982] has investigated the effects of non-uniform prestress distributions on the rupture growth of a dynamic shear crack and has identified circumstances under which the rupture velocity of the extending crack is significantly affected. Simulations of rupture processes based on specified rupture speeds as in a kinematic modeling procedure clearly would not reveal the effects of prestress on rupture velocity.

With increasingly detailed and advanced seismic strong ground motion recording and analysis capabilities, the importance of dynamic shear crack modeling to earthquake studies is emphasized. Archuleta [1984] used a kinematic forward modeling procedure to

match details of the recorded strong ground motions from the 1979 Imperial Valley, California earthquake. He inferred a strong correlation between fault slip rate and fault rupture velocity, and his final model included locally supersonic rupture velocity. While his modeling effort was not based on a dynamic crack formulation, his results, including the possibility of supporting locally supersonic rupture velocity which depends in the dynamic modeling upon the distribution of fault prestress, are in qualitative agreement with Day's theoretical results for fully spontaneous dynamic shear crack propagation along a slip-weakening fault.

It has been previously noted, for example, by Dieterich [1979a] and Rice [1983], that fault constitutive relations of a strictly slip weakening-type are not appropriate for characterizing repeated seismic slip along a given fault reach. Because any fault displacement would be associated with weakening, the displacement or slip weakening makes no provision for fault restrengthening. Thus, seismicity would ultimately be expected to cease or to give way to steady quasistatic fault slip as the means for accommodating imposed strains. In addition, slip-weakening models do not account for experimental observations of velocity-dependent frictional sliding behavior. Constitutive relations which incorporate rate- and sliding surface state-dependent frictional sliding behavior have been developed to account for the laboratory observations and to overcome these limitations to the slip-weakening framework. It has been demonstrated the the rate- and state-dependent friction constitutive models predict a wide range of frictional sliding behavior as well as describe laboratory observations of quasistatic fault slip [e. g., Dieterich, 1979a and b, 1980, 1981; Ruina, 1983; Gu *et al.*, 1983; Tullis and Weeks, 1985].

In the previous chapter, it is noted that, for stick-slip instabilities generated on simulated fault surfaces, the onset of the unstable fault slip is characterized by a slip-weakening stage during which the shear stress at a position on the fault surface decreases from a peak, or yield, stress level to a residual level as a critical fault displacement

is achieved. This critical displacement, beyond which the unstable sliding proceeeds at a relatively constant shear stress level, is strongly dependent on fault surface roughness. It is also noted that this behavior is at least qualitatively similar to that observed during experiments in which fault slip rate is suddenly increased under quasistatic loading conditions. Insofar as the observations presented in the previous chapter and these observations of quasistatic fault sliding, from which the rate- and state-dependent friction constitutive models were developed, are obtained from similarly prepared simulated fault surfaces, it might be expected that similar constitutive relations could be used for both the quasistatic sliding and the stick-slip sliding. In this chapter, following a discussion of rate- and state-dependent friction models, model calculations are presented to explore the applicability of rate- and state-dependent friction models to stick-slip.

3.2 State Variable Friction Models

Rate- and state-dependent, or state variable, rock friction models were developed to account for details of laboratory observations of quasistatic sliding along simulated fault surfaces. Their development can be traced through Dieterich [1972, 1978a, 1979a and 1981b] and Ruina [1983]. The essential elements of the state variable rock friction model are:

(1) A direct velocity effect. When a sudden change in fault slip rate v is introduced, the frictional resistance changes in the same sense as that of the change in slip rate. That is, suddenly imposed increases in slip rate result in sudden increases in friction. Likewise, sudden decreases in slip rate are accompanied by sudden decreases in frictional resistance.

(2) A steady-state effect. For sliding at a constant slip rate and under constant normal load, friction tends toward a steady-state value which depends on that slip rate.

(3) Characteristic slip distances. The evolution of friction toward the steady-state value at a given slip rate is controlled by an exponential decay over a characteristic or critical displacement. This critical displacement is related to fault roughness and is relatively insensitive to fault slip rate and applied normal stress.

The formulation for coefficient of friction μ proposed by Dieterich [1979a] to account for these observed effects in the quasistatic experiments is:

$$\mu = C F^{-1} \qquad (3.1)$$

where:

$$C = c_1 + c_2 \log_{10}(c_3\theta + 1)$$

and

$$F = f_1 + f_2 \log_{10}(f_3/v + 1).$$

Coefficients c_1, c_2, c_3, f_1, f_2, and f_3 are empirically determined constants. The evolution of the state is contained in the formulation of the state variable θ which is also empirically determined in order to best fit the shape of the evolution toward steady state. As mentioned above, the forms of θ which have been proposed typically contain an exponential decay of θ as a function of fault displacement.

Ruina [1983] elaborated on the interpretation of θ as a state variable and he also proposed a simpler form for μ, based on his own laboratory experiments which were carried out with low slip rates. While Dieterich [1981] attempted to identify the variable θ which appears in his formulation as an effective lifetime of a contacting asperity, Ruina [1983] suggests that state variables need not be identified with specific physical quantities. From this perspective, the rate- and state-dependent friction models are viewed as

phenomenological descriptions of the frictional sliding process and specific formulations can be adopted in order to closely match experimental observations. In order to account for his own laboratory observations of quasistatic frictional sliding [Ruina, 1983] and, later, to serve as a starting point for the theoretical analysis of the stability of a sliding system governed by a state variable friction law [*e. g.*, Gu *et al.*, 1984], Ruina proposed the following simplified form of the friction law proposed by Dieterich:

$$\mu = \mu_0 + A \ln \left(\frac{v}{v^*}\right) + \Theta, \qquad (3.2)$$

where the quantities in his model [Ruina, 1983] have been normalized by normal stress σ to yield equation (3.2) . The parameters μ_0 and A are empirical constants and μ_0 may be regarded as a nominal value of friction. Ruina's state variable is Θ, and v^* is an arbitrary reference slip rate. In this formulation, the evolution of Θ is separated from the direct velocity effect.

Both of the formulations (3.1) and (3.2) have been used in theoretical calculations to simulate the mechanics of one- and two-dimensional model faults, and, because of this, the discussion that follows will focus on these specific forms. For the low slip rates which are characteristic of the quasistatic sliding experiments, the reduction of (3.1) to (3.2) is straightforward, but it is presented in some detail here in order to clearly establish the relationship between these two formulations and to indicate how they overlap or predict different behavior, particularly at the high rates of sliding which are achieved during stick slip. This is apparently the same reduction used by Mavko [1983] who assigned values to the parameters in (3.2) based on the empirically determined values presented in Dieterich [1981b] and used a friction model of the same form as (3.2) for a numerical simulation of creep on a large-scale fault.

In reference to the parameters appearing in equation (3.1), it is generally observed [Dieterich, 1980 and 1981b] that

$$c_1 >> c_2, f_1 >> f_2,$$

$$\text{and } c_1 \approx f_1, c_2 \approx f_2 .$$

From the values of the parameters presented in Dieterich [1981b], it also follows that

$$c_1 >> c_2 \log(c_3\theta + 1)$$

and (3.3)

$$f_1 >> f_2 \log(\frac{f_3}{v} + 1).$$

We rewrite (3.1) as

$$\mu = \frac{X + x}{Y + y} \qquad (3.4)$$

where

$$X = c_1$$

$$Y = f_1$$

$$x = c_2 \log(c_3\theta + 1)$$

$$y = f_2 \log(\frac{f_3}{v} + 1).$$

Using inequalities (3) and neglecting higher order terms in x and y, expression (3.4) can be rewritten as

$$\mu \approx \frac{c_1}{f_1} + \frac{c_2}{f_1} \log(c_3\theta + 1) - \frac{c_1 f_2}{f_1^2} \log(\frac{f_3}{v} + 1). \qquad (3.5)$$

In (3.5), the direct velocity effect has been separated from the state evolution effect. If θ is interpreted as being related to an effective time of asperity contact for sliding at slip rate v, then θ and v are inversely related. For low slip rate v which typifies the quasistatic experiments, both $c_3\theta$ and f_3/v are large compared to unity so that (3.5) can be reduced to a form which is identical to (3.2), namely,

$$\mu \approx \mu_0 + A \ln\left(\frac{v}{v^*}\right) + \Theta,$$

if

$$\mu_0 = \frac{c_1}{f_1} + \frac{c_2}{f_1}\log(c_3)$$

$$A \approx \frac{1}{(2.303)}\frac{c_1 f_2}{f_1^{\,2}} \qquad (3.6)$$

$$v^* = f_3$$

$$\Theta = \frac{c_2}{f_1}\log(\theta)\,.$$

From this discussion, it is seen that, under conditions of low rates of slip which are typical of quasistatic experiments, formulations (3.1) and (3.2) converge and are fully equivalent. However, at large v, the additive constant terms in the logarithms dominate in (3.1). As v increases, θ will decrease until $c_3\theta << 1$, and $f_3/v << 1$. As a result, both the direct velocity effect and the state-related effects encounter cutoffs such that further increases in v or decreases in θ do not affect μ. Because no such cutoffs are present in (3.2), the constitutive laws could predict rather different results when v is large, as during stick-slip.

From this point, the focus will be on two questions. First, are state variable constitutive laws compatible with dynamic stick-slip observations ? Second, if they are compatible, is the simpler form (3.2) adequate, or is it necessary to employ the full form (3.1) and incorporate the high-speed cutoffs to the velocity- and state-related effects ? Model calculations will be presented based on two rate- and state-dependent friction models, one which includes the velocity cutoffs

$$\mu \approx \frac{c_1}{f_1} + \frac{c_2}{f_1} \log(c_3\theta + 1) - \frac{c_1 f_2}{f_1^2} \log(\frac{f_3}{v} + 1). \qquad (3.7a)$$

and one which admits no cutoffs at high slip rate,

$$\mu \approx \frac{c_1}{f_1} + \frac{c_2}{f_1} \log(c_3\theta) - \frac{c_1 f_2}{f_1^2} \log(\frac{f_3}{v}). \qquad (3.7b)$$

Note that (3.7a) is identical to relation (3.5), which is the first-order simplification of Dieterich's original friction law. If conditions (3.6) are met, then (3.7b) is identical to the Ruina formulation (3.2).

Equations (3.7a) and (3.7b) for μ, then, are the forms of the rate- and state-dependent friction constitutive model that are considered. Both forms feature a constant term which, given the smaller magnitudes of the coefficients c_2 and f_2 (see inequalities 3.3), can be considered as a nominal value of frictional resistance. The state- and velocity-dependent terms in (3.7) are appropriately viewed as second-order terms in these models. The differences between (3.7a) and (3.7b) are readily seen in Figure 3.1. Figure 3.1a is a plot of coefficient of friction μ as a function of log θ , calculated according to equation (3.7a) for selected values of slip rate v ranging from 10^{-12} m/s to 1 m/s using the

model coefficients indicated which are a combination of the published values of Dieterich [1981b] and parameters c_3 and f_3 which are discussed later in this chapter. Figure 3.1b is the same as 3.1a, but using (3.7b) instead of (3.7a). Looking first at Figure 3.1b, the linear relationship between μ and $\log_{10}\theta$ predicted by (3.7b) appears such that the μ-vs- $\log_{10}\theta$ relations for different slip rates plot as parallel straight lines for all v and θ . For the friction model with cutoffs, represented by (3.7a), the lower portion of Figure 3.1a for large θ and/or small v shows a μ-vs-$\log_{10}\theta$ relationship which is identical to that in Figure 3.1b. That is, at low slip rate and large θ, the Dieterich and the Ruina formulations are equivalent. In the case of sufficiently small θ , this "low slip rate" equivalence of (3.7a) and (3.7b) breaks down, and the additive constant "plus one" term dominates over the evolution of θ and friction is independent of θ . The range of θ over which the θ-dependence of μ flattens out is clearly related to the value of parameter c_3. For large v, the direct velocity term in (3.7a) is dominated by the "plus one" that appears there and the coefficient of friction is not affected by increases in slip rate. This cutoff is determined by the value of parameter f_3.

3.3 Data and Analysis

In the previous chapter, it was noted that high-frequency observations of stick-slip instabilities exhibited characteristics which resemble those which are observed during quasistatic sliding experiments. Beyond presenting stick-slip source parameters, it was suggested there that the qualitative similarities between these two types of experiments might be substantiated quantitatively, if records of the quasistatic fault behavior preceding the stick-slip events were included in the analysis.

The quasistatic sliding experiments which were used to develop the rate- and state-dependent friction models by Dieterich and others typically employ controlled constant shear displacement loading histories under constant normal load conditions, so that the fault constitutive response to v can be directly monitored. Although tests are currently being

designed to investigate possible normal stress history effects on the constitutive behavior of simulated faults, it is generally felt that a varying normal load during frictional sliding will affect the evolution of the state of the sliding surface. Therefore, it is important to strive to maintain conditions of constant normal stress throughout a given sliding history. Unlike the small-scale quasistatic sliding tests, the stick-slip experiments are conducted with a loading history which is prescribed in terms of constant remote shear stress loading rate under constant normal stress. The loading machine was designed such that the stiffnesses in the two principal stress directions are roughly equal and the 45° orientation of the sliding surface with respect to these directions ensures that the normal load across the sliding surface remains constant during sliding [Goodman and Sundaram, 1978]. This evaluation of the state variable friction models depends on being able to measure the fault slip rates both quasistatically and dynamically and thus follow the evolution of the sliding state through the entire course of the experiment.

It was noted that, in the series of stick-slip experiments performed on smooth and rough sliding surfaces, stick slip on the smooth fault is preceded by relatively little measurable fault creep compared to the rough fault. On the rough fault, an interval of appreciable stable fault creep always preceded the stick-slip event, often to offsets comparable to the fault displacement associated with the dynamic fault slip. Because of the difficulty in measuring the small amounts of precursory creep on the smooth fault, it is difficult to estimate fault slip rates immediately prior to the stick-slip event. Therefore, this present analysis is limited to a discussion of the rough fault data.

The procedure that is followed is shown schematically in Figure 3.2. From two DCDT displacement transducers mounted across the simulated fault and digitally recorded at a rate of 1 Hz, fault displacement d is measured with respect to a zero offset corresponding to the start of shear loading. These displacement records are differentiated once in the time domain to provide estimates of fault slip rate. From this information, the evolution of the

state variable θ is calculated according to an evolution law which is adopted from Dieterich [1979a],

$$\theta = \frac{d_c}{v}\left(\theta_0 \frac{v}{d_c}\right)^{\exp\left(\frac{d_0 - d}{dc}\right)} \qquad (3.8)$$

for the evolution of θ . This is the solution to the differential equation :

$$\frac{d_c}{v}\frac{d(\log \theta)}{dt} = -(\log \theta) + \log \frac{d_c}{v} \quad . \qquad (3.9)$$

The parameter d_c controls the evolution of the state variable and gives rise to the characteristic slip distances discussed previously.

An initial θ_0 value of 300 s is assumed to begin this first evolution calculation at times corresponding to time t_1 in Figure 3.2 . The stick-slip event appears in the 1 Hz displacement records as a step-like feature at time t_2. After each time step, θ_0 is reset to the most recent update of θ, d_0 is reset to 0, and the calculation using equation (3.8) is repeated. This calculation is carried out through the accelerating creep stage indicated in the sketch up to the time t_2 of the stick-slip event.

To make what might be the best possible estimate of the fault state at the onset of stick slip, rather than taking the v and θ values determined from this procedure at time t_2 as the final pre-instability state values, estimates of the fault state evolution up to the time of the stick-slip event are continued by using the high-frequency shear stress and fault slip data recorded at 200,000 Hz which are plotted in Figure 3.2b. The displacement records generally do not reflect substantial amounts of fault movement in the few milliseconds immediately prior to the stick-slip event, so that these displacement records are not used to evaluate fault state between times t_2 and t_3 in the high-frequency data set. Instead, it is

assumed that, because the offsets which can be achieved during these last fractions of a millisecond before stick slip are small compared to d_c, the changes in shear stress can be attributed primarily to the direct velocity effect and not to the evolution of the state variable. Thus, the fault slip rate v from t_2 up to the time of stick slip t_3 is estimated from the recorded shear stress, normalized by normal stress σ , by solving equations (3.7) for slip rate v. Once stick slip begins at time t_3, the fault slip rate is set to the measured values $v_{S\text{-}S}$ and equations (3.7) and (3.8) are used to calculate the remainder of the friction-time history.

Stress and slip data from a stick-slip event are shown in Figure 3.3. Stress data are marked with an S and slip data with a D. This event began to rupture near one end of the fault and then propagated over the remainder of the fault surface. Near the nucleation area, from which the top traces are recorded, there is a relatively smooth acceleration from creep into the unstable slip event, and the assumption that the changes in frictional resistance result solely from the direct velocity effect is more questionable. State variable θ might be rapidly changing. Away from this part of the fault, the changes in slip rate are more pronounced so that records at the lower part of the figure more closely reflect the conditions used in the quasistatic tests where slip rate changes are suddenly introduced so that they are achieved without significant evolution of the state variable θ . In this study, only those data for which there is the suggestion that the change in slip rate to stick slip was achieved rapidly and without appreciable evolution of θ are included. Such data resemble traces S4 and S7 in Figure 3.3.

3.4 Results

This fitting procedure is illustrated with the stick-slip record shown in Figure 3.4a; the left side of 3.4a is friction μ obtained by dividing recorded shear stress by normal stress σ and the right side is fault displacement versus time. The curves in Figure 3.4b and c are

calculated friction histories from (3.7a) and (3.7b), respectively . The model parameters that are used in the calculations are based on those reported in Dieterich [1980] for clean, gouge-free, rough granite surfaces. They are : $f_1 = 1.0$, $f_2 = 0.010$, $f_3 = 25.0$ μm/s, $c_2 = 0.013$, and c_3=0.5/s . For $f_1 = 1.0$, the parameter c_1 can be interpreted as a nominal value for the friction coefficient at high-slip rate, and this value is determined from the data to be $c_1 = 0.56$. Parameter d_c which controls the evolution of the state variable corresponds to the observed "slip-weakening" displacements of approximately 25 μm. With the model parameters listed above, the calculated friction history is shown in Figure 3.4b from (3.7a) with cutoffs and in 3.4c from the model without cutoffs (3.7b). As might have been expected because of the cutoffs, the simulation based on (3.7a) is truncated with respect to the simulation based on (3.7b), and it under-predicts the variations in frictional resistance μ that are exhibited in the data. On the other hand, the simulation based on (3.7b) over-predicts the changes in μ . Without either of the cutoffs, it predicts too large a value of peak friction and too low a value of residual sliding friction, and important stress diference parameters (peak to initial) and (initial to residual) are correspondingly over-predicted.

The velocity cutoffs in (3.7a) introduce additional degrees of freedom to the fitting of the stick-slip data which are not available when using (3.7b). Because the cutoffs are felt under conditions where $c_3\theta << 1$ and $f_3/v << 1$, by varying the values of parameters c_3 and f_3, the peak and residual stress levels can be adjusted. Maintaining constant values for the parameters c_1, c_2, f_1, and f_2, the effects of changing the values of f_3 and c_3 are shown in Figures 3.5a and 3.5b, respectively, in the model calculations of μ using the formulation with cutoffs (3.7a). As seen in this figure, increasing the direct velocity cutoff f_3 allows the peak shear stress to increase. Similarly, increasing the steady-state cutoff c_3 allows the residual shear stress to drop to lower and lower values. In Figure 3.5c, data and a good-fitting calculation which used values of $c_3 = 15$ /s and $f_3 = 50$ μm/s are shown. The results of all of the comparisons of the data with these model calculations are listed in Table

3.1 . For this procedure leading to the values presented in Table 3.1 , only the parameters c_3 and f_3 are adjusted; all other parameters are held constant. Calculations using (3.7b), the friction model without the high-speed cutoffs, are illustrated in Figure 3.6 . Varying the values of c_3 and f_3 does not affect the shapes of the computed friction time histories and the friction changes are consistently overestimated. The fit to another record from the same stick-slip event is shown in Figures 3.7 and 3.8 .

3.5 Discussion and Summary

Observations of dynamic stick-slip frictional instabilities can be matched by model calculations based on a rate- and state-dependent friction constitutive relation of the form proposed by Dieterich [1979a] in order to account for laboratory observations of quasistatic sliding of simulated fault surfaces. Besides the introduction of a state memory effect which is realized by introducing a state variable which evolves with fault displacement, important features of this type of frictional constitutive relation are cutoffs at high slip rates to both the rate- and state-related effects. Identical numerical values of friction model parameters, except, importantly, for the cutoff parameters which have to be greatly increased over those estimated from earlier quasistatic sliding experiments in order to fit the dynamic observations, can be used to satisfy the data.

There is a large discrepancy between the estimates of the cutoff parameters presented here and those presented by Dieterich [1978a; 1979a] , as well as a large variation among the estimated values. The fitting procedure that is used in this study assumes that all of the variability within a friction history is due to the level of slip rate at which the effects of the cutoffs are felt, and, indeed, adjusting the values of the cutoff parameters is sufficient to approximately match the observed friction history. On the other hand, it is generally agreed that a number of factors affect measured values of "nominal" friction. A varying c_1 would,

given a specific slip rate history, be expected to trade off with resultant estimates of parameters c_3 and f_3.

The slip rates, while they are, admittedly, uncontrolled because they are measured during an instability, are large enough that the effect of a cutoff at the high speeds is clearly expressed. While it is possible that Dieterich's low estimates of c_3 and f_3 are reliable and would imply that important effects are not being considered in this study, it is also possible that his estimates more accurately represent lower bounds because of an inability to control sliding at short times of contact θ or high speed. It is clearly desirable to be able to control slip and specify v even at the (very) high speeds.

While the formulations proposed by Dieterich [1979a] and Ruina [1983] are equally appropriate for describing frictional slip at low slip rates, at which the cutoff parameters are not important, frictional sliding at high slip rates associated with dynamic shear instabilities is best described by a state variable friction model which includes the high-speed cutoffs. With these high-speed cutoffs, fault frictional behavior is rate-independent at very high slip rates, so that a slip-weakening fault constitutive relation, not applicable over the entire range of slip rates nor strictly appropriate for describing more than one episode of dynamic slip, is indeed capable of describing a stick-slip frictional instability. The analysis of the spreading of the surface of rupture then follows the analysis of a dynamic shear crack. Rice and Tse [1985] have already noted this is connection with their use of a rate- and state-dependent friction model in calculating the dynamic motions of a spring and point sliding mass system. Additional experimental work is required to provide more detailed insights into the high-speed cutoffs.

Table 3.1 . Estimates of velocity cutoff parameters. v_{sta} is last value of slip rate calculated by matching μ with direct velocity effect before setting slip rate to v_{stick} for unstable slip. $c_1 = 0.56$, $c_2 = 0.013$, $f_1 = 1.0$, $f_2 = 0.01$ [Dieterich, 1981b].

record	v_0(μm/s)	v_{stick}(cm/s)	$\mu_p - \mu_0$	$\mu_p - \mu_r$	v_{sta}(μm/s)	c_3(/s)	f_3(μm/s)
44-4	0.33	5.48	0.0116	0.0507	26	100	40
44-7	0.33	15.50	0.0275	0.0493	1.1×10^4	65	2.5×10^4
45-7	0.04	7.54	0.0304	0.0464	1.2×10^4	12	1×10^4
46-7	0.02	1.90	0.0294	0.0417	474	5	3500
47-4	0.17	6.15	0.0138	0.0457	54	15	50
47-7	0.06	18.54	0.0221	0.0482	98	15	500
48-4	0.42	6.76	0.0055	0.0397	2.5	10	5
48-7	0.22	8.02	0.0209	0.0397	70	6	1200
49-4	0.14	7.93	0.0122	0.0496	16	25	20
49-7	0.06	18.83	0.0218	0.0479	43	15	500
50-1	0.31	4.33	0.0058	0.0471	0.7	60	5
57-1	0.42	11.87	0.0210	0.0747	1040	3100	2500
57-4	0.25	5.98	0.0058	0.0450	1.3	15	5

average $\log f_3 = (2.29 \pm 1.38) \Rightarrow f_3 \approx 200$ μm/s ,

average $\log c_3 = (1.44 \pm 0.73) \Rightarrow c_3 \approx 30$ /s .

Figure Captions.

Figure 3.1 . Calculated values of μ as a function of θ for different values of slip velocity. $c_1 = 0.56$, $c_2 = 0.013$, $c_3 = 30$ /s, $f_1 = 1.0$, $f_2 = 0.01$, $f_3 = 200$ μm/s . (a) μ calculated from equation (3.7a), the friction model with cutoffs. (b) μ calculated from equation (3.7b), the friction model without cutoffs. Dashed lines represent steady-state values of μ where $v = d_c/\theta$.

Figure 3.2 . (a) Plots of quasistatic fault displacement history for stick slip. (b) High-frequency shear stress and fault displacement. Times t_1, t_2, and t_3 signifying stages in the analysis are indicated in the figure.

Figure 3.3 . Rough fault stick-slip data. Traces marked with S are fault shear stress; those marked with D are fault displacement.

Figure 3.4 . Example of the fitting procedure to record 47-4 to determine values of high-speed cutoffs. (a) Normalized stress and fault displacement data. (b) Calculated μ using equation (3.7a). (c) Calculated μ using equation (3.7b). In all calculations $c_1 = 0.56$, $c_2 = 0.013$, $c_3 = 0.5$ /s, $f_1 = 1.0$, $f_2 = 0.01$, $f_3 = 25$ μm/s.

Figure 3.5 . Effects of adjusting cutoff parameters c_3 and f_3 in equation (3.7a); $c_1 = 0.56$, $c_2 = 0.013$, $f_1 = 1.0$, $f_2 = 0.01$. (a) Different f_3. (b) Different c_3. (c) Final choices of c_3 and f_3.

Figure 3.6 . Plots of μ vs time for model without cutoffs, equation (3.7b); $c_1 = 0.56$, $c_2 = 0.013$, $f_1 = 1.0$, $f_2 = 0.01$. c_3 and f_3 values indicated.

Figure 3.7 . Same as Figure 3.4, but for record 47-7.

Figure 3.8 . Same as Figure 3.5, but for record 47-7.

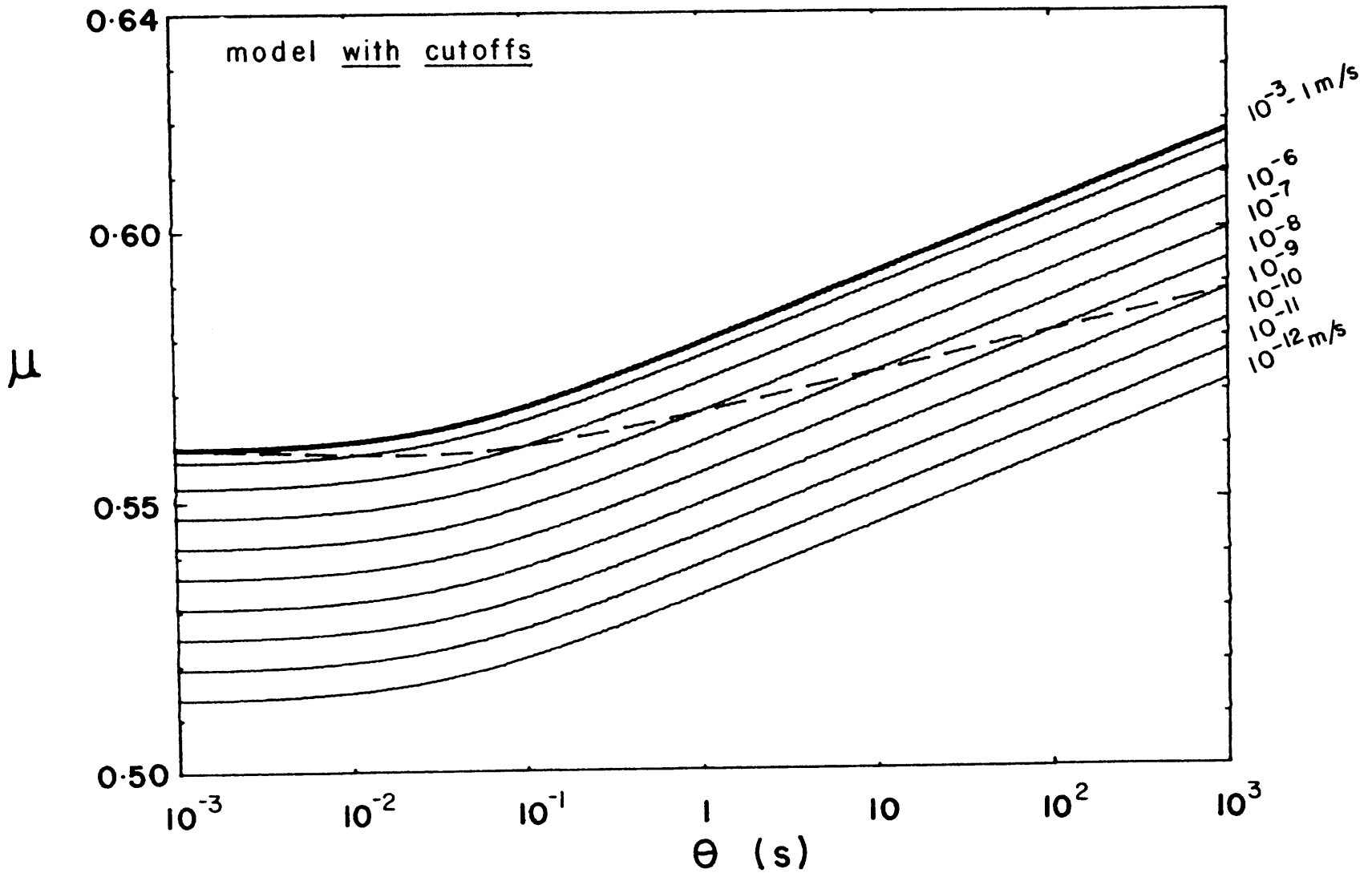
model with cutoffs
0·64
0·60
0·55
0·50
μ
10^-3
10^-2
10^-1
1
10
10^2
10^3
θ (s)
10^-3 m/s
10^-6
10^-7
10^-8
10^-9
10^-10
10^-11
10^-12 m/s

Figure 3.1a

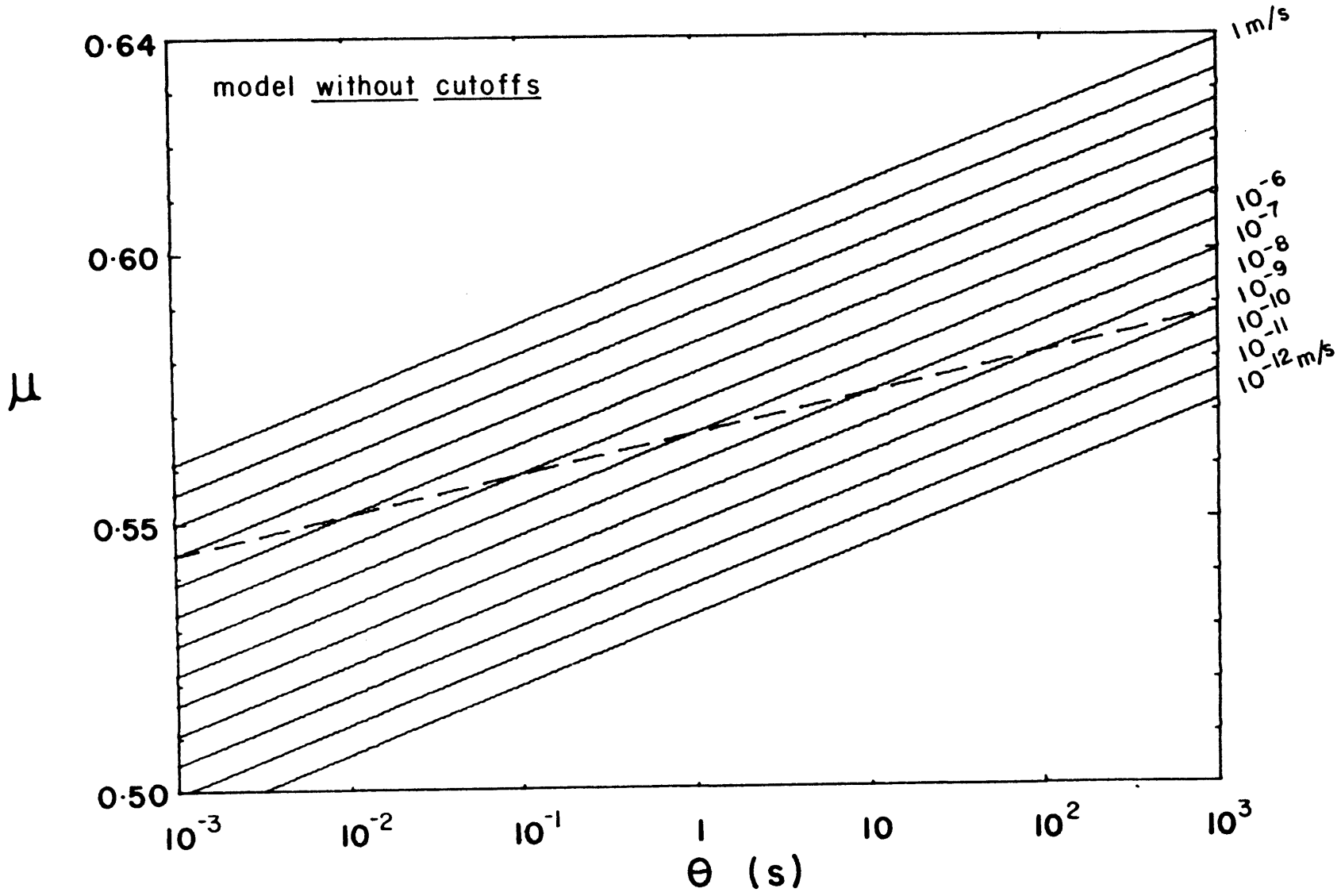
model without cutoffs
0·64
0·60
0·55
0·50
μ
10^-3
10^-2
10^-1
1
10
10^2
10^3
θ (s)
1 m/s
10^-6
10^-7
10^-8
10^-9
10^-10
10^-11
10^-12 m/s

Figure 3.1b

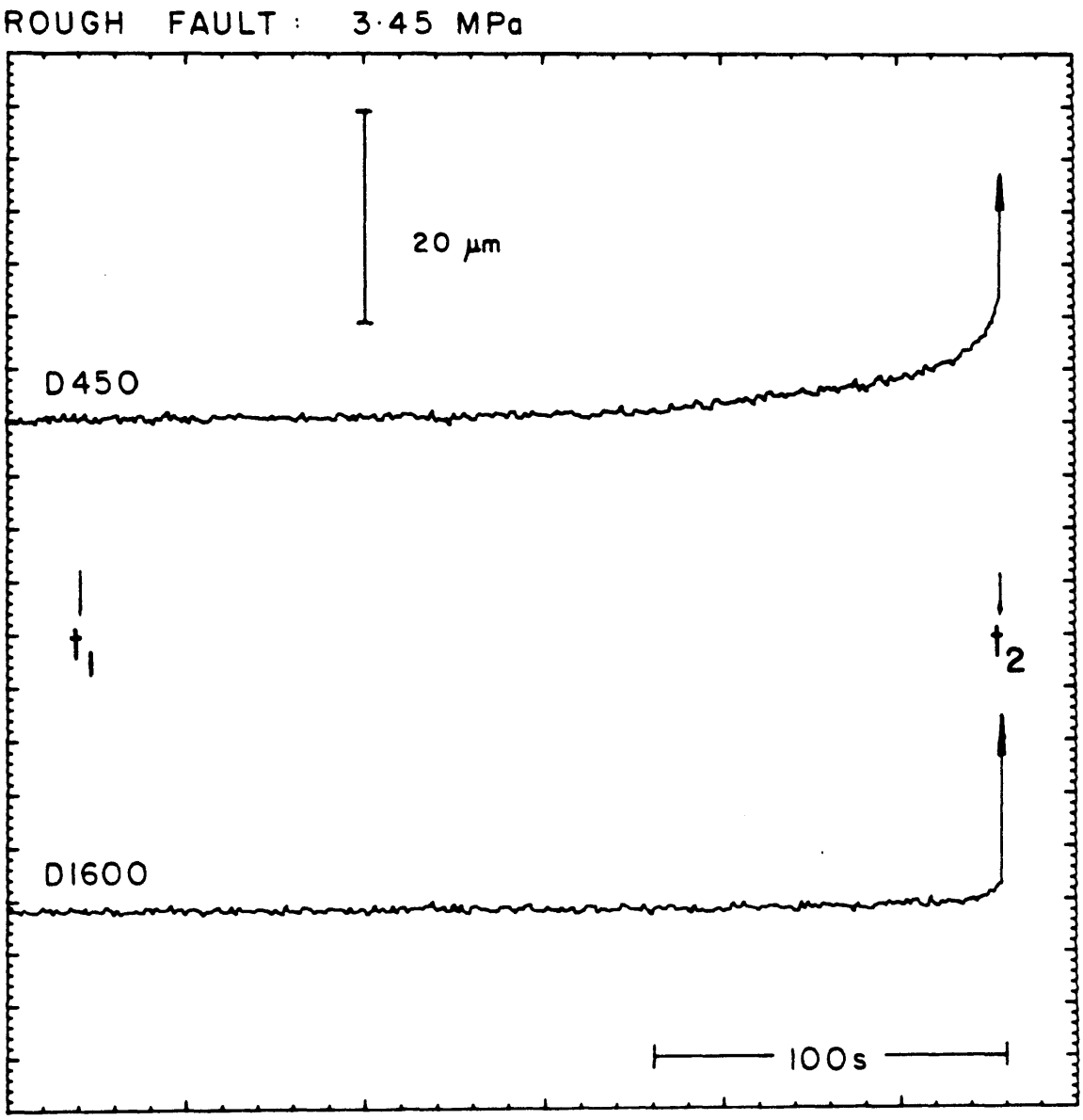

Figure 3.2a

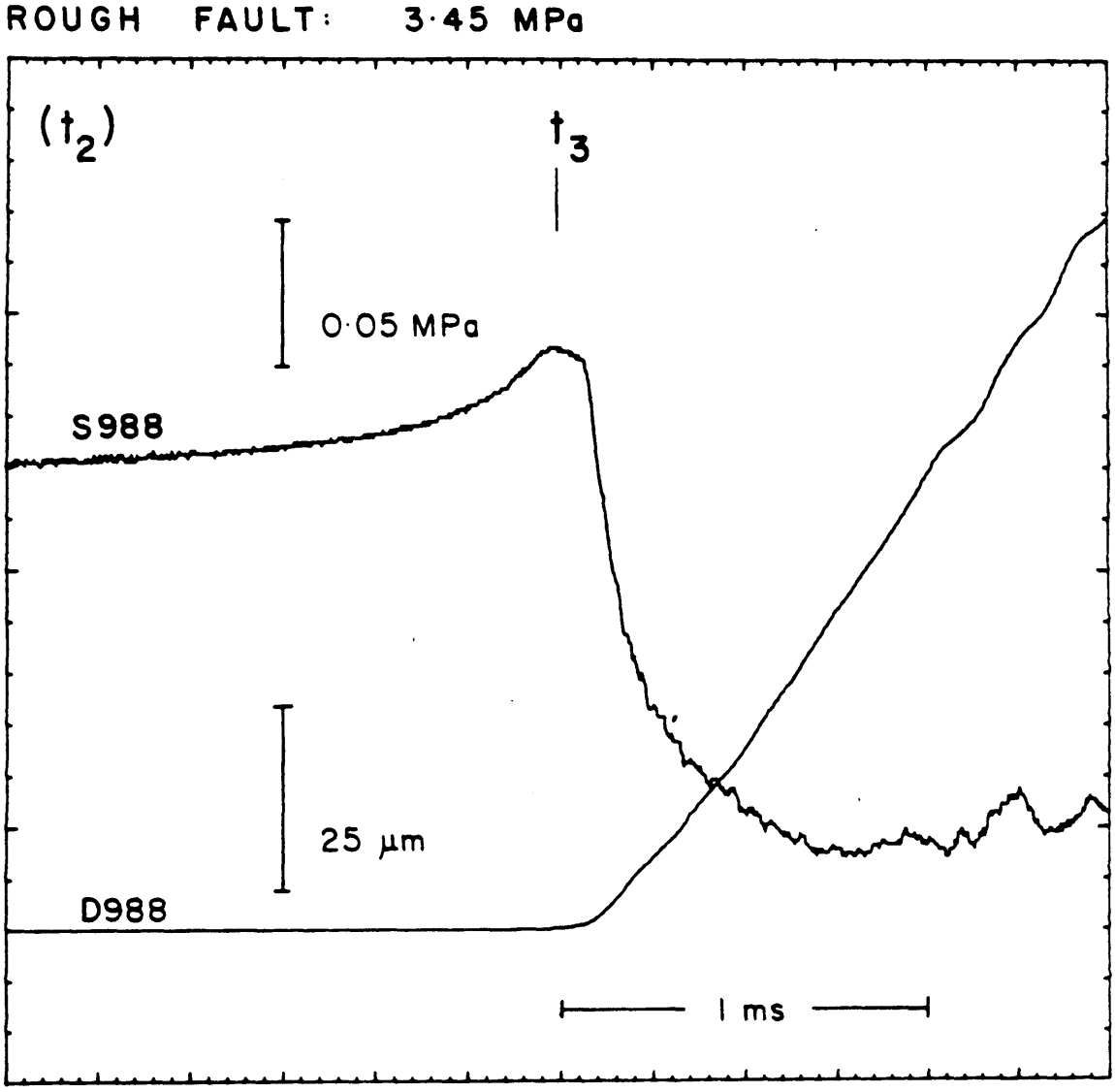

Figure 3.2b

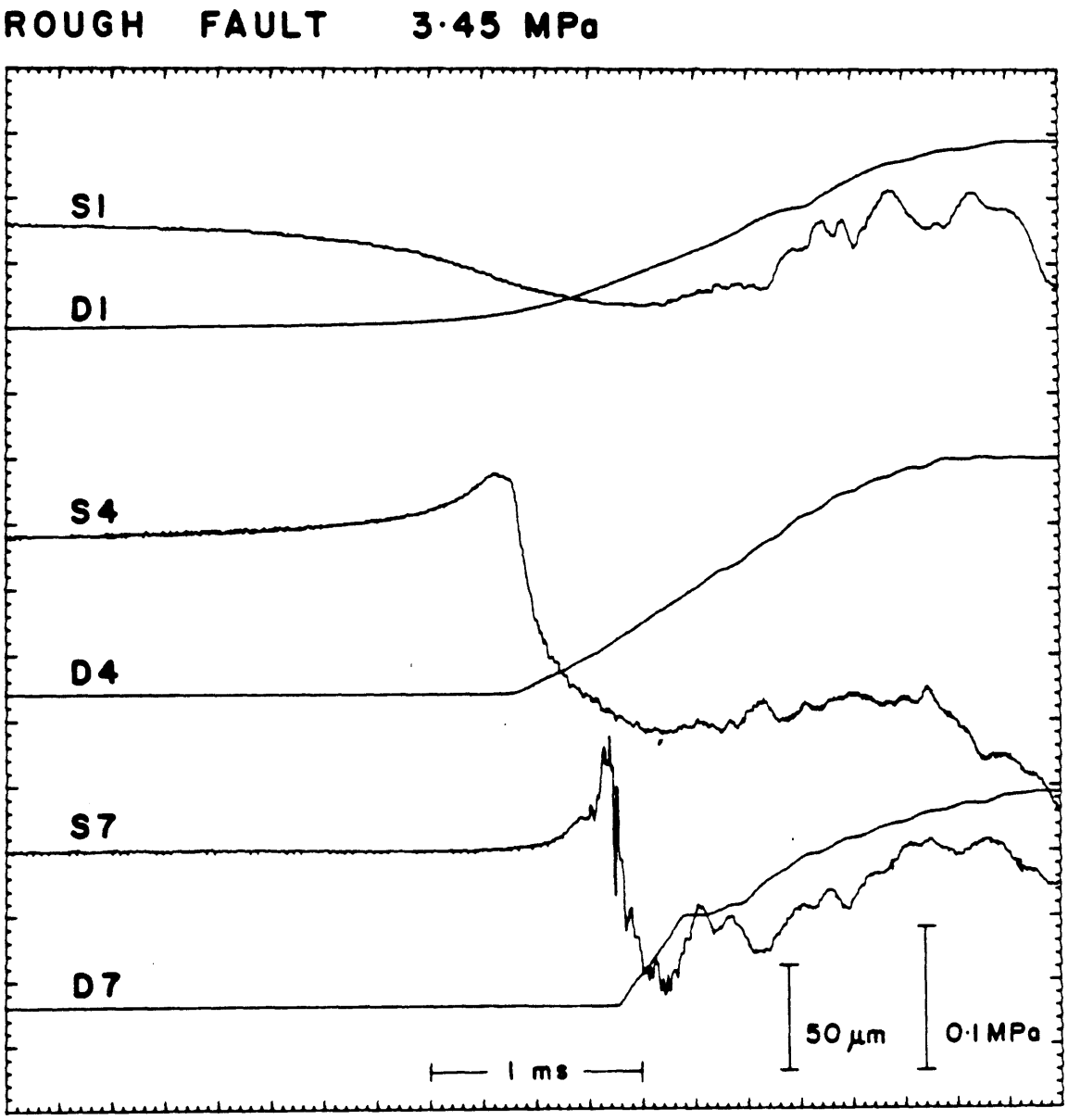

Figure 3.3

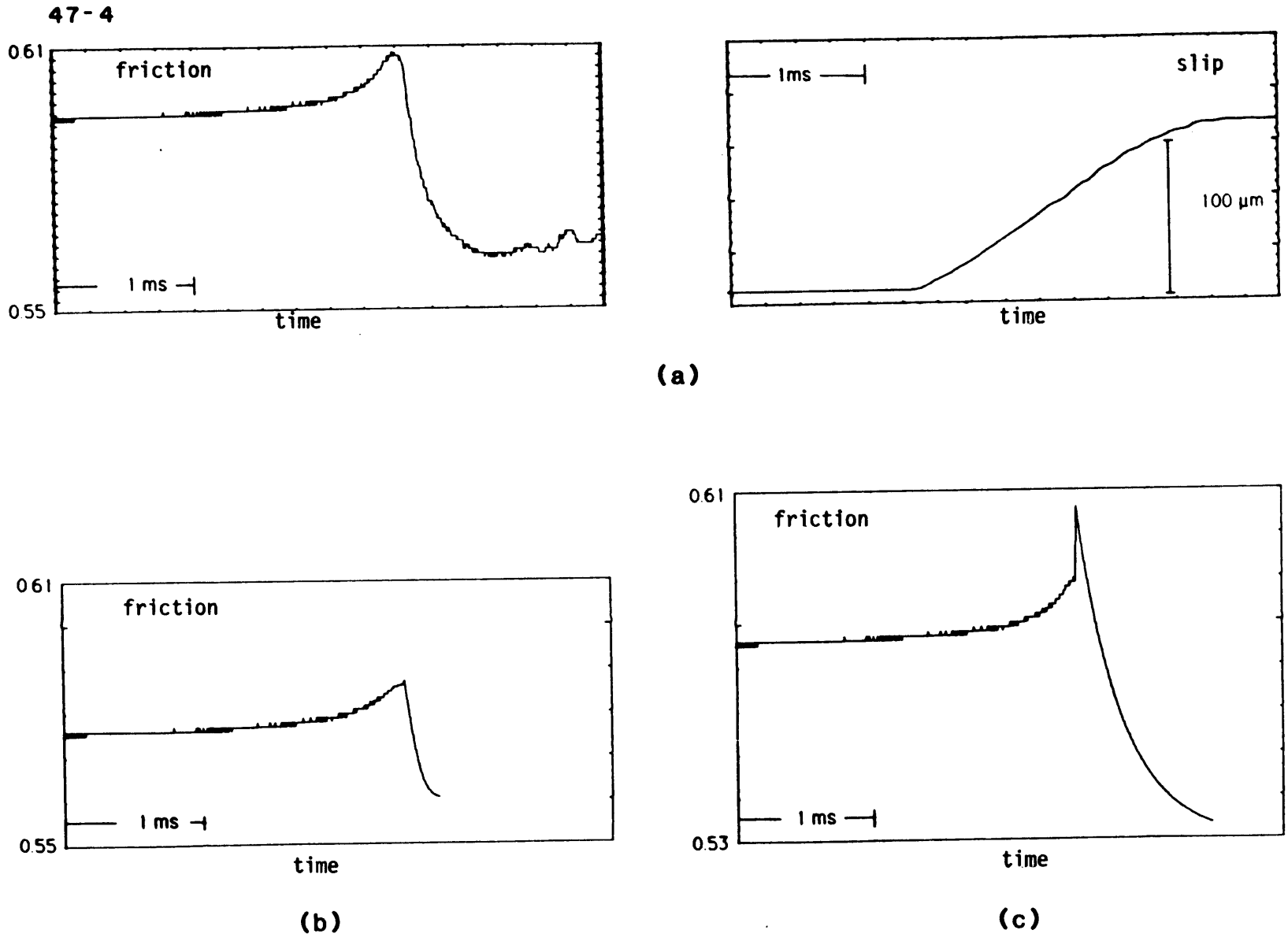
47-4
0.61
friction
1 ms
0.55
time
1ms
slip
100 µm
time
(a)
0.61
friction
1 ms
0.55
time
(b)
0.61
friction
1 ms
0.53
time
(c)

Figure 3.4

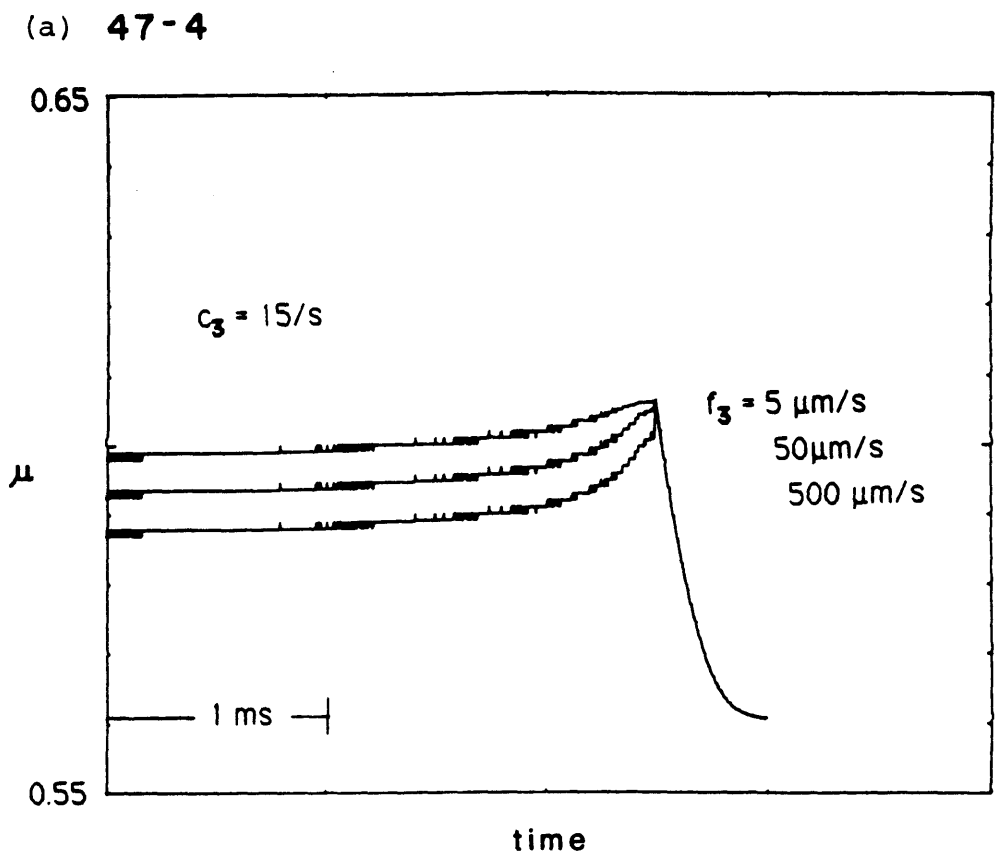
(a) 47-4
0.65
c_3 = 15/s
f_3 = 5 μm/s
50μm/s
500 μm/s
μ
1 ms
0.55
time

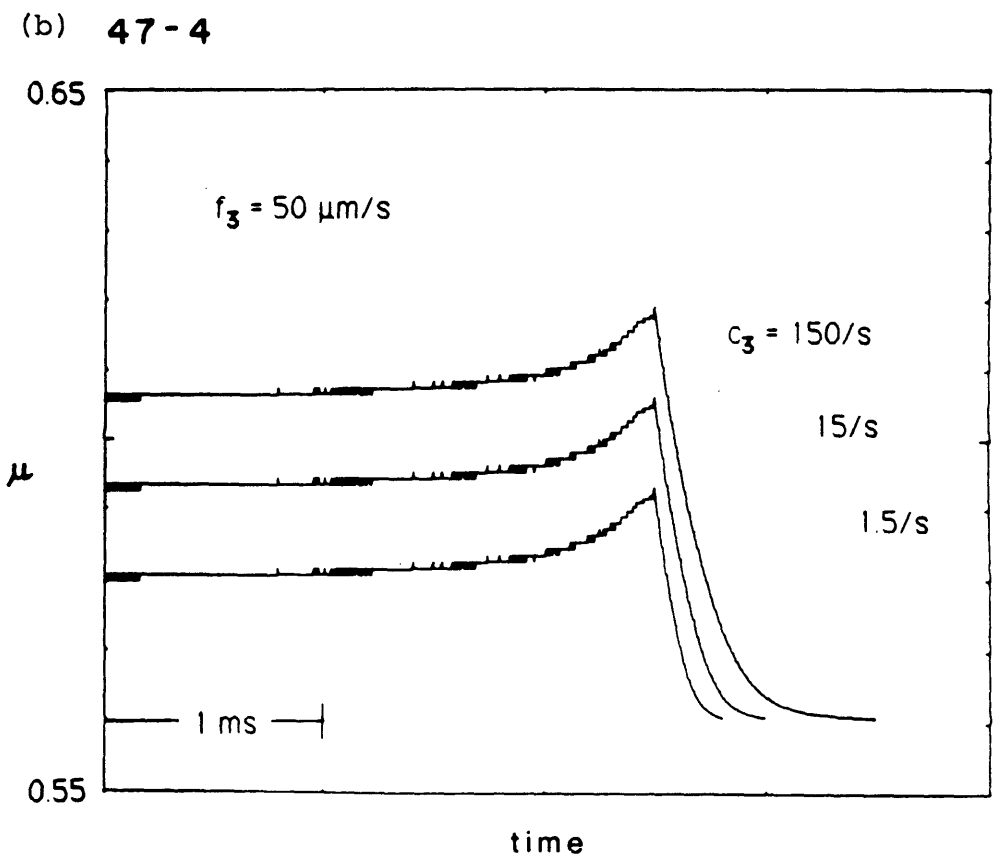
(b) 47-4
0.65
f_3 = 50 μm/s
c_3 = 150/s
15/s
1.5/s
μ
1 ms
0.55
time

Figure 3.5

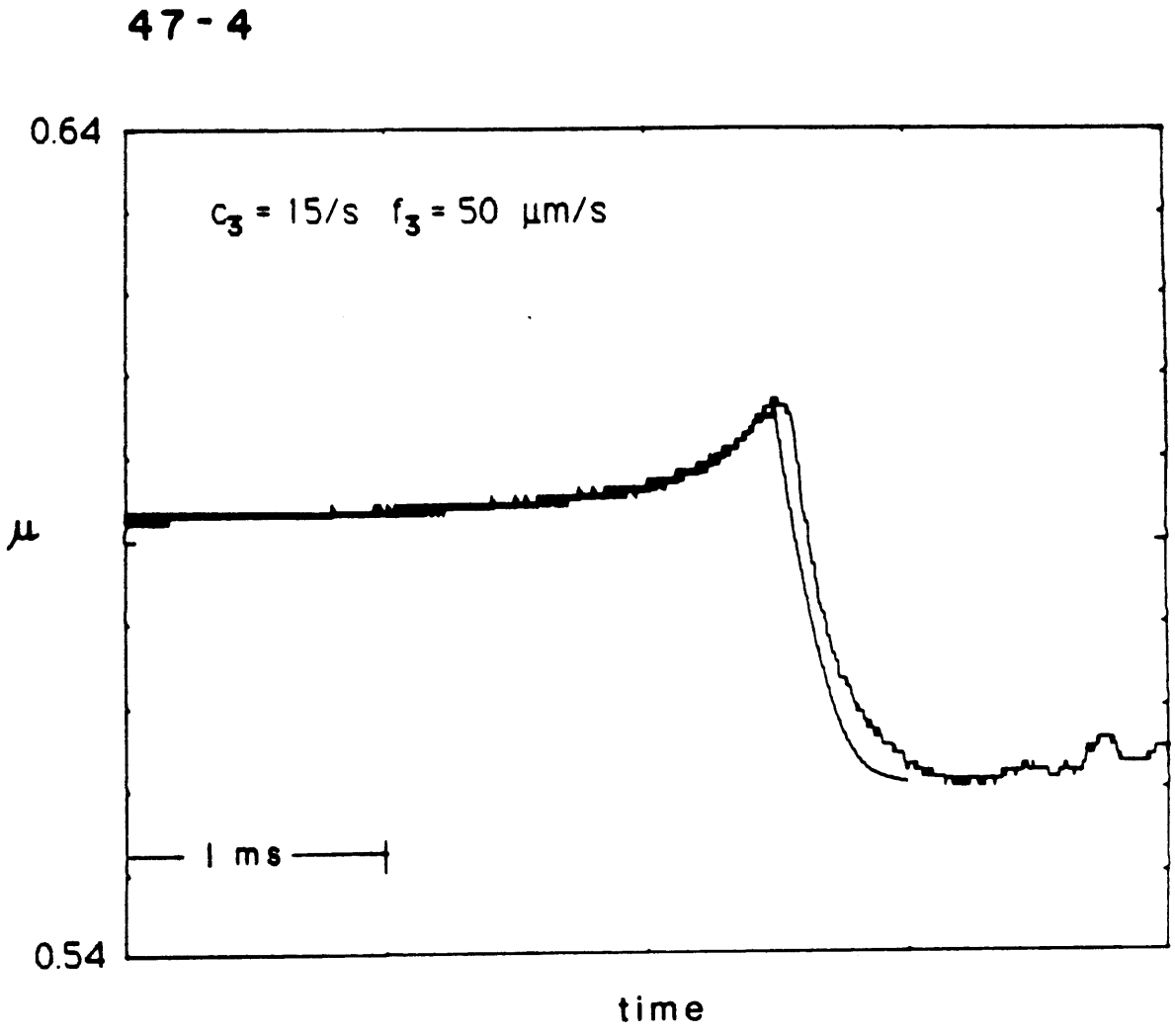

Figure 3.5c

47-4 Calculated μ vs time - no cutoffs

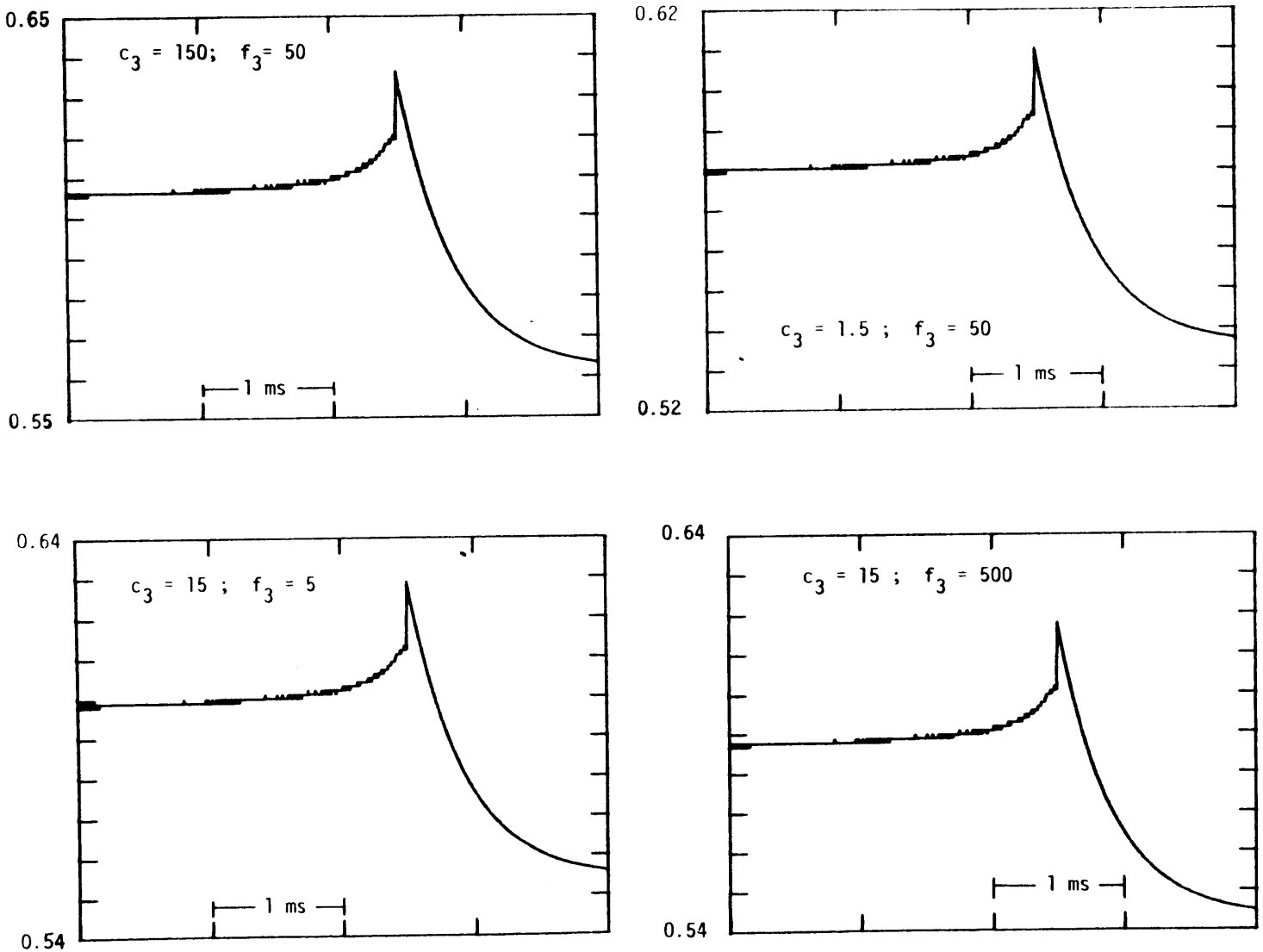

Figure 3.6

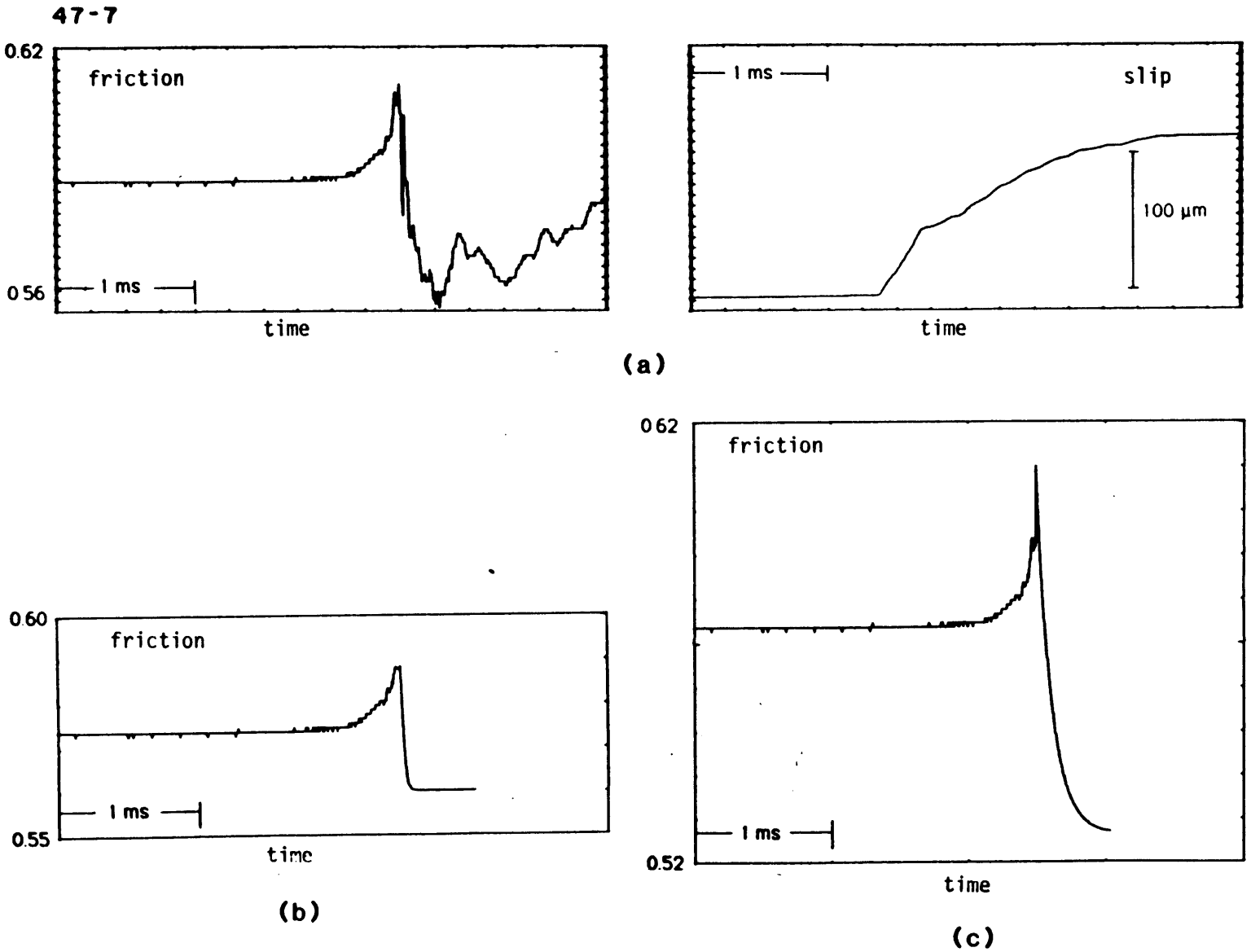
47-7
0.62
friction
0.56
1 ms
time
1 ms
slip
100 µm
time
(a)
0.62
friction
1 ms
0.52
time
(c)
0.60
friction
1 ms
0.55
time
(b)

Figure 3.7

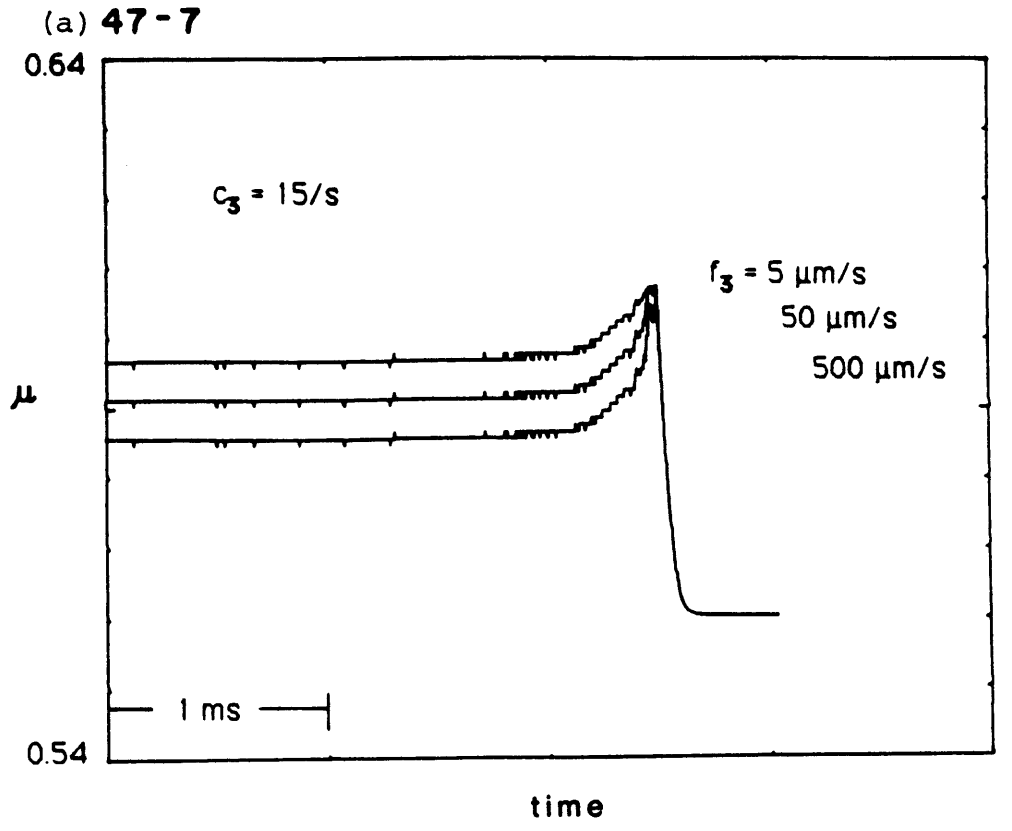
(a) 47-7
0.64
c_3 = 15/s
f_3 = 5 µm/s
50 µm/s
500 µm/s
µ
1 ms
0.54
time

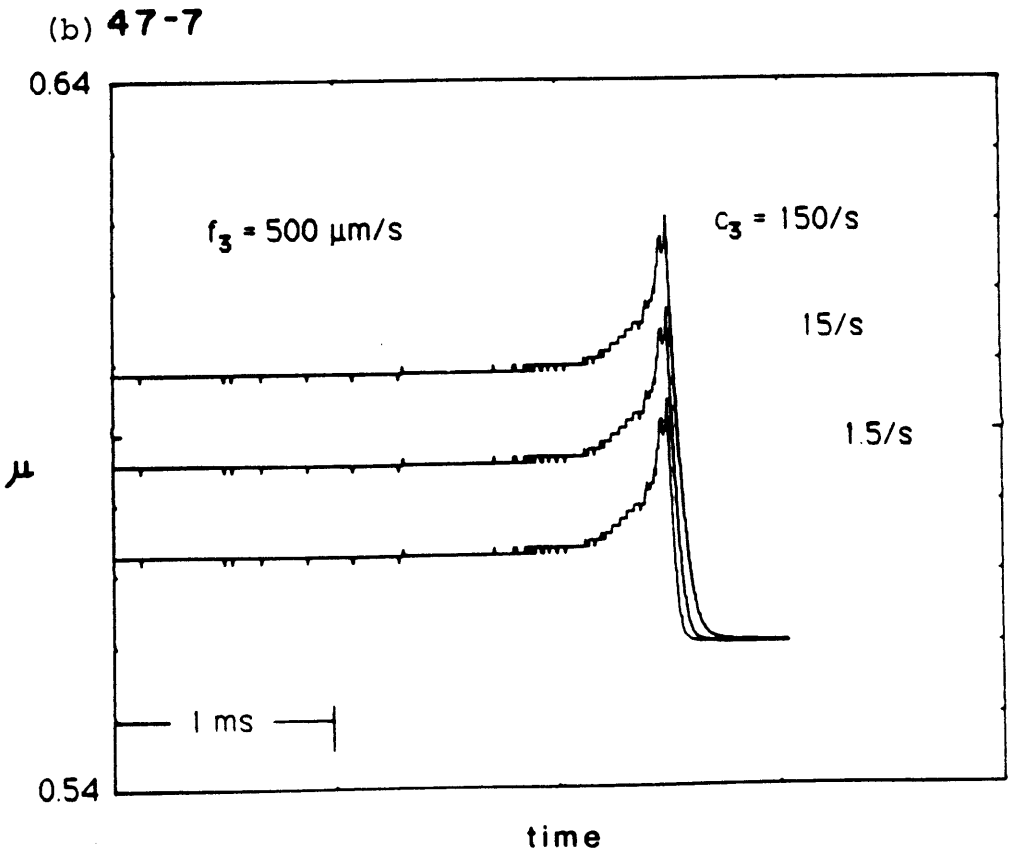
(b) 47-7
0.64
f_3 = 500 µm/s
c_3 = 150/s
15/s
1.5/s
µ
1 ms
0.54
time

Figure 3.8

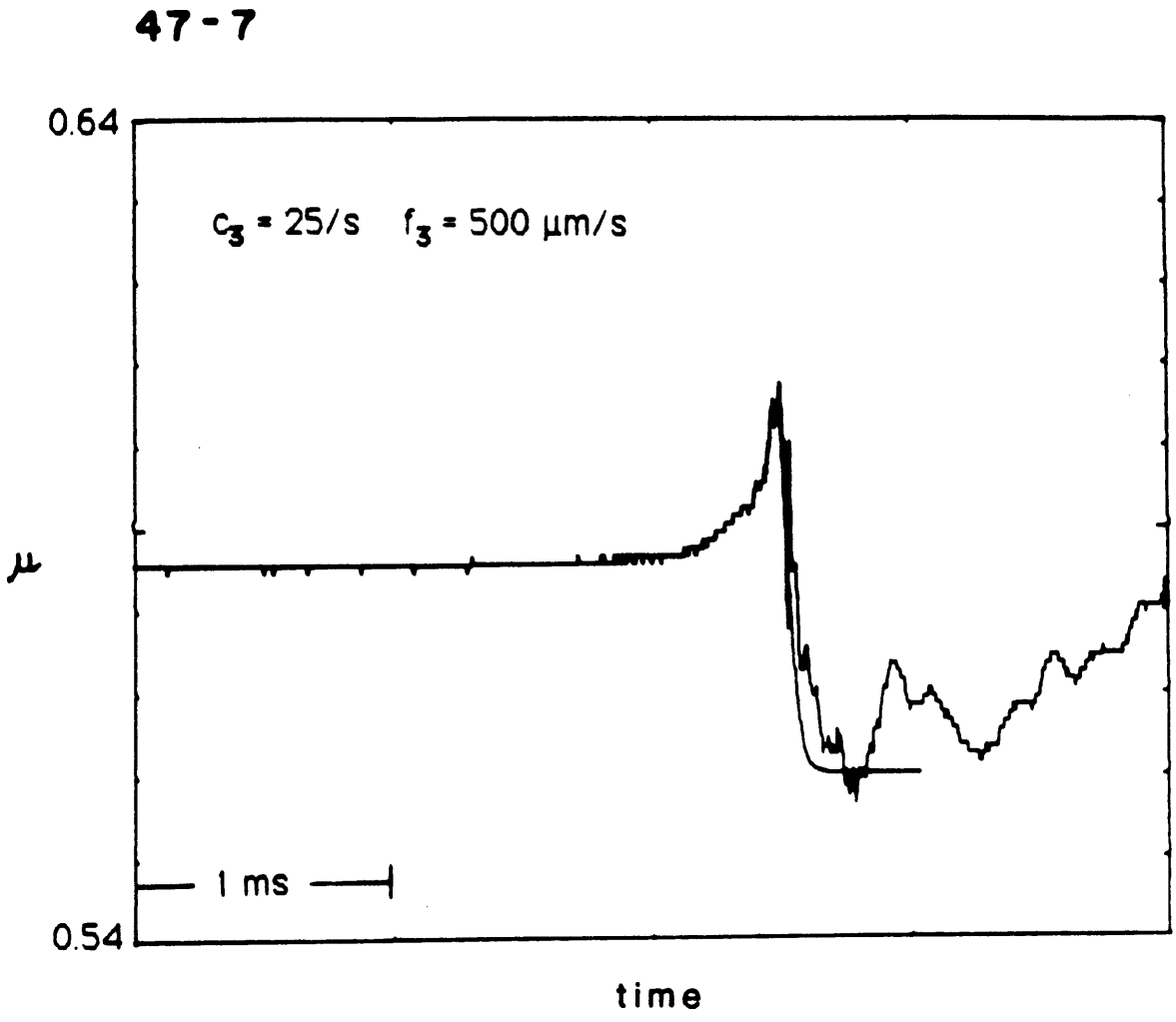

Figure 3.8c

Chapter 4 - Numerical Modeling of Frictional Instabilities

4.1 Introduction

The development of a physical understanding of earthquake failure processes remains as one of the classical problems in geophysics. In the interests not only of predicting the recurrence times and locations of earthquakes over regional scales but also of predicting the ground motion response generated during a single earthquake, this understanding assumes a great deal of practical importance as well. If it were possible to set up and solve the dynamic fault rupture problem, *i. e.*, to determine the way in which the fault rupture nucleates and extends over the fault surface according to specified fault constitutive properties in response to initial stress conditions, then the powerful representation theorems developed by Maruyama [1963] and Burridge and Knopoff [1964] are available to calculate the ground displacement response throughout the medium surrounding the fault.

Much of the background for dynamic earthquake source modeling is taken from the theory of fracture and is generalized or extended from tensile crack models to dynamic shear crack models, as in the case of the slip weakening cohesive zone fault model which has been discussed earlier in this thesis. Of course, the underlying assumption is that the earthquake rupture can be modeled as a dynamic, or spontaneously self-supporting, shear crack. For this assumption to be justified, non-elastic rupture processes on the fault surface must be confined to a region which is small compared to the total fault length. Failure to meet this criterion of small-scale yielding restricts the direct application of many laboratory observations to studies of earthquake source dynamics. Seismological insights have been provided by analyses of some of the relatively few known solutions for dynamic crack growth, for example, those of Kostrov [1964 and 1966] and Richards [1976], which require simplifying assumptions - usually involving specifying constant rupture velocity - in order to obtain the solution.

Many authors have studied dynamic shear rupture processes using numerical modeling methods. The general approach is to specify a fault constitutive relation or failure criterion and initial and boundary conditions for the medium containing the fault, and then solve the equations of motion for the fault response, including all details of rupture growth as part of the complete crack solution. These studies have addressed a range of questions, from the effects of different fault failure criteria and different prestress or fault strength distributions on the dynamics of a single earthquake, to the effects of distributed fault strength and stress on the development of earthquake sequences. From this body of research, the work of Ida [1972, 1973b], Andrews [1976a and b, 1985], Das [1976] and Das and Aki [1977a and b], Mikumo and Miyatake [1978, 1979], and Day [1982] are cited as examples.

A key element in the dynamic crack model is the fault constitutive relation which is selected to govern the fault response to the applied loads, and, thus, the way in which the fault rupture will spread over the fault surface. The critical stress intensity factor failure criterion [Irwin, 1958] was adapted for numerical modeling procedures by Hamano [1974]. Hamano's procedure defined a finite critical stress level by averaging the crack-tip stress singularity which arises in the analytic solution over the fault grid point spacing. Hamano's method was fully developed by Das [1976] and Das and Aki [1977a] for two-dimensional cracks and by Das [1980] for three-dimensional crack problems. It is demonstrated in Das and Aki [1977a] that the critical stress level adaptation is indeed approximately equivalent to the critical stress intensity factor criterion.

Slip weakening fault models and cohesive zone fault models in general, discussed in the preceding chapters, are felt to be physically more reasonable because they require that stresses at the tip of the crack are always finite, limited by a peak yield stress. As used by Ida [1972], who initially proposed the extension of the concept of cohesive zones at the tips of tensile cracks to slip-weakening models for shear cracks, and Andrews [1976b],

parameters of the fault slip-weakening model were not directly related to laboratory friction data, although there is always sort of an implicit correspondence between peak and residual shear stress levels in the slip-weakening models to "static" and "dynamic friction." Day [1982] used laboratory stick-slip data presented in Dieterich [1980] and similar to that presented in Chapter 2 of this thesis to specify a fault strength ratio s

$$s = \frac{(\tau_p - \tau_0)}{(\tau_0 - \tau_r)} . \qquad (4.1)$$

but he did not use other laboratory-based estimates for assigning values to other slip weakening parameters.

In Chapter 2, some basic laboratory observations were presented from experiments which afforded detailed examination of the dynamic stick-slip frictional failure process on simulated fault surfaces. One of the most significant of those observations was that, at the onsets of unstable stick-slip sliding at different locations along the fault, the fault would exhibit a slip weakening-like character, such that the fault frictional shear strength would decrease as fault displacement increases during a stick-slip event. A characteristic fault slip parameter, a critical slip-weakening displacement, was identified such that, at this critical slip increment, the decreasing fault shear strength would achieve a residual level and further slip during the instability would occur at this constant residual shear stress level. It was also noted in that chapter that this slip weakening-like behavior closely resembles that which is observed during laboratory studies of quasistatic sliding along similarly prepared simulated fault surfaces when the rate of sliding of the rock samples is suddenly and stably forced to change. The quasistatic sliding experiments inspired the development of a family of frictional constitutive relations which is rate- and sliding state-dependent so that no explicit displacement dependence of frictional resistance is admitted. In Chapter 3, the applicability of this family of constitutive relations to stick-slip frictional sliding is considered in detail. It

was found there that such a constitutive description of the frictional sliding is consistent with the stick-slip observations as long as the models include features which essentially turn off the dependence of friction on slip rate at very high rates of sliding which characterize the stick-slip events.

The rate- and state-dependent class of friction models has been used on numerous occasion in theoretical calculations. In a sense it is this modeling capability which gives the state variable friction modeling approach an additional degree of usefulness beyond merely fitting laboratory data. Extensive analysis has been done on the single degree-of-freedom sliding system governed by a state variable friction model, including much work on the nature of the frictional sliding process leading up to fault instability [*e. g.*, Dieterich, 1980, 1981 and 1985; Ruina, 1983; Rice and Ruina, 1983; Gu *et al.*, 1984]. Modeling of a fault in a continuum has also been conducted [Dieterich, 1979b; Mavko, 1983; Tse, 1985] to consider a more realistic idealization of a fault. In these studies, when the condition for instability is reached, dynamic slip is simulated by prescribing slip at a very high maximum rate until equilibrium is restored. Tse [1985] and Rice and Tse [1985] have studied the full dynamic response of a single degree-of-freedom sliding system governed by a state variable friction model.

In this chapter, theoretical calculations are presented from a numerical model of a dynamic shear crack with a state variable frictional constitutive relation. Aspects of these numerical solutions as they relate to features of the state variable friction model will be discussed.

4.2 Crack Modeling Procedure

The calculations which are presented below were performed using the code RUPTWO, written and generously provided by Dr. D. J. Andrews of the U. S. Geological

Survey. For the purposes of the present discussion, the original version of RUPTWO provided by Dr. Andrews has been modified to incorporate the slip rate- and state-dependent fault constitutive relation which was found in Chapter 3 to match the stick-slip stress drops. Full details of the numerical modeling procedure, except for the implementation of the rate- and state-dependent friction law, are given in Andrews [1985]. Only a general outline of the procedure is given here.

A numerical Green function, or boundary integral, method is used to determine displacements on the fault surface through numerical convolution of past values of traction on the fault plane with the appropriate Green function. This boundary integral procedure was introduced by Hamano [1974] and subsequently developed by Das and Aki [1977a] to perform simulations of two-dimensional rupture propagation. Andrews [1985] demonstrates how this modeling procedure can be used to model faults governed by a slip-weakening friction law as well as the critical stress level approximation to elastic-brittle cracks used in the earlier boundary integral fault models. Andrews [1985] reports greater numerical precision and faster computational results compared to finite difference fault simulations, at least for planar fault surfaces, with the boundary integral method. He also suggests that the boundary integral method could be used with other types of fault constitutive relations besides a slip-weakening law.

Following the development in Andrews [1985], the fault surface is defined as the x_3-plane in an infinite, homogeneous, isotropic elastic whole-space. Shear displacement $\mathbf{u} = (u_1,u_2)$ across the fault is related to traction change $\mathbf{T} = (T_1,T_2)$ on the fault through the convolution

$$\mathbf{u}(x_1,x_2,t) = \iiint \mathbf{G}(x_1 - \xi_1, x_2 - \xi_2, t - \tau)\, \mathbf{T}(\xi_1,\xi_2,\tau)\, d\xi_1\, d\xi_2\, d\tau \,. \qquad (4.2)$$

where $\mathbf{G}$ is the impulse response Green function tensor for a half-space. Reducing the

problem to two dimensions - spatial coordinate x_1 and time t - and assuming plane strain, equation (4.2) simplifies to

$$u(x,t) = \iint g(x - \xi, t - \tau)\, T(x,\tau)\, dx\, d\tau \quad . \qquad (4.3)$$

where vector subscripts have been dropped and g(x,t) is the component of the two-dimensional Green function tensor corresponding to the impulse respone in the x_1-direction due to a force applied in the x_1-direction.

The problem is discretized by dividing the fault into elements of size Δx and considering time steps Δt in duration and assuming that traction T is constant within each fault element. The convolution can be written in terms of the double summation:

$$u(j, m) = \sum_k \sum_n F(k, n)\, T(j - k, m - n), \qquad (4.4)$$

where u(j, m) and T(j, m) are slip and traction values at time step m and fault element j such that

$$T(x, t) = T(j, m) \text{ and } u(x, t) = u(j, m)$$

for $x_j - \Delta x/2 < x < x_j + \Delta x/2$ and $t_m - \Delta t/2 < t < t_m + \Delta t/2$.

F(j, m) is the discretized form of g:

$$F(j, m) = \int_{t_m-\Delta t/2}^{t_m+\Delta t/2} \int_{x_j-\Delta x/2}^{x_j+\Delta x/2} g(x, t)\, dx\, dt \quad . \qquad (4.5)$$

Given the discretized Green function F, equation (4.4) expresses the relationship between present values of fault slip to present and past values of traction. If the spatial grid

point spacing is equal to (or greater than) v_p times the time grid point spacing, the zero-lag terms in (4.4) can be isolated in such a way that (4.4) can be rewritten

$$u(j, m) + C\, T(j, m) = L(j, m) \qquad (4.6)$$

where $C = - F(0, 0)$ can be regarded as a local compliance and

$$L(j, m) = \sum_{k} \sum_{n>0} F(k, n)\, T(j - k, m - n)\,. \qquad (4.7)$$

is the loading at (j, m) which is only dependent on past values of traction. This linear relationship (4.6) between slip and traction is the basic result of the boundary integral solution which is required by the elastic response of the two sides of the fault. As mentioned earlier, the full details of this development are given in Andrews [1985] and, in places, the following discussion will closely parallel that found there.

4.3 Implementation of the State Variable Friction Model

Through the specification of a fault constitutive relation, the complete solution to this problem can be found. Andrews [1985] used a fault slip-weakening model in order to compare those results with his earlier calculations of fault rupture using a finite difference procedure. The rate- and state-dependent frictional fault constitutive relation which is discussed in Chapter 3 is used in the calculations presented here.

Uniform frictional properties and initial conditions are assumed over the entire fault. The constitutive equation used is the simplified form of the state variable constitutive friction relation introduced by Dieterich equation (3.7.a) and the evolution law for the state variable θ is (3.8) from Dieterich [1979a] which is observed to fit the observed evolution of the state at

high slip rates [Dieterich, 1981]. It should be noted that this evolution law has the feature that the displacement parameter governing the decay of θ to steady-state value can be closely identified with the critical displacement that would appear in a slip-weakening model. These equations, then, completely characterize the frictional response of the fault.

$$\mu \approx \frac{c_1}{f_1} + \frac{c_2}{f_1} \log(c_3\theta + 1) - \frac{c_1 f_2}{f_1^2} \log(\frac{f_3}{v} + 1)$$

$$\theta = \frac{d_c}{v} (\theta_0 \frac{v}{d_c}) \exp(\frac{d_0 - d}{d_c}) \quad . \tag{4.8}$$

Frictional strength S is the product of μ with normal stress σ, that is, $S = \mu \sigma$. Several features of the state variable friction model distinguish the occurrence of the dynamic rupture process from that which would be governed by a slip-weakening model. A fundamental difference between a rate- and state-dependent friction model and a slip-weakening model is that a state variable friction model assumes that there is always some sliding taking place at non-zero slip rate v. The fault is initially assumed to be slipping uniformly at slip rate $v = v_0$, where, in the cases calculated here, v_0 is assigned values of either 10^{-7} or 10^{-8} m/s. To completely specify the initial fault state, initial values of $\theta = \theta_0$ must also be specified. Initial stress on the fault is $T_0 = \sigma \mu_0$, where initial fault friction μ_0 is given by:

$$\mu_0 \approx \frac{c_1}{f_1} + \frac{c_2}{f_1} \log(c_3\theta_0 + 1) - \frac{c_1 f_2}{f_1^2} \log(\frac{f_3}{v_0} + 1). \tag{4.9}$$

The velocity cutoff in the "direct" velocity term in equation (4.8) imposes a maximum, limiting value of frictional strength $S_{max} = \sigma\mu_{max}$ which depends on the value of

θ, when $v >> f_3$. S_{max} corresponds to the peak yield stress parameter in a slip weakening model. As friction μ approaches μ_{max}, where

$$\mu_{max} = \frac{c_1}{f_1} + \frac{c_2}{f_1}\log(c_3\theta_0 + 1)\,, \qquad (4.10)$$

small increases in μ can be associated with large increases in v, with v taking on "infinitely" large values. For $\mu < \mu_{max}$, if the applied load $T_t = T_0 + T$ exceeds friction S, the fault responds quasistatically, by slipping at increasing $v > v_{0,}$ through a period of accelerating fault creep. The applied loads are balanced by increased friction due to the direct velocity dependence [Dieterich, 1985]. With a slip weakening model, the fault is locked and slip does not occur until $T_t \geq S$.

Unstable fault slip occurs as the energy available to advance the crack tip is greater than that required to overcome frictional resistance and create freshly faulted surface, when the decrease in friction with fault slip proceeds at a rate which is greater than the rate of stable unloading of the fault. During stick-slip, friction decreases with increasing fault displacement through the evolution of θ to a steady-state value θ_{ss} at which most of the unstable slip occurs [Tse, 1985; Rice and Tse, 1985]. It is presumed that unstable fault slip occurs at $v >> f_3$ so that the direct velocity cutoff takes effect and, through slip on the fault and the evolution of θ, traction is prevented from exceeding the frictional resistance and $T_t = S$.

Due to the finite fracture energy which can be associated with a state variable friction model [Dieterich, 1980], stick-slip sliding cannot initiate from a single point. A crack with a minimum critical length must be developed before the rupture can propagate freely [Dieterich, 1985]. An analogous critical crack length is required for dynamic rupture along a slip weakening fault, and this concept is discussed in Andrews [1976, 1985] and Day [1982]. Similar to the approaches taken by Andrews [1976, 1985] and Day [1982], in the initial

stages of the calculation, rupture extension is forced at a constant rupture velocity until the critical crack is developed. The rate of this forced crack nucleation is chosen to be $(0.5)v_R$. Behind the tip of the forced crack, traction is prescribed. Forced slip rate is assumed to be above the f_3 cutoff so that friction is matched to the prescribed traction by adjusting state variable θ.

RUPTWO requires that the fault state information from the immediately preceding time step be saved. For element j, at the current time step m, a trial value of traction T^{tr} is calculated assuming no additional fault slip. Following that assumption, fault frictional strength is calculated using the previous value of θ (no evolution) and reverting the trial fault slip rate to v_0. If friction is greater than traction, this trial solution is accepted as the solution for the current time step. That is, if $| T^{tr} + T_0 | < S$,

$$\begin{aligned} T(j, m) &= T^{tr}(j, m) \\ u(j, m) &= u(j, m - 1) \\ \theta(j, m) &= \theta(j, m - 1) \\ v(j, m) &= v_0(j) \ . \end{aligned} \qquad (4.11)$$

If $T^{tr} + T^0 \geq S$, then the fault state must change in such a way that the traction is equal to the friction. The system of equations

$$\begin{aligned} T(j, m) + T_0(j) &= S(j, m) \\ u(j, m) + C\, T(j, m) &= L(j, m) \end{aligned} \qquad (4.12)$$

are solved for the traction and slip at (j, m) with an iterative procedure until a convergence

criterion $|T_t - S| \leq \varepsilon$ is met. A trial solution using the fault state values at step (j, m-1) is the initial guess. Under circumstances where $S < S_{max}$ the procedure is based on balancing the traction by increasing friction through the direct velocity effect. State variable θ is evolved through incremental displacement $\Delta u^{tr} = (v^{tr} + \Delta v^{tr})\Delta t$. For $S \geq S_{max}$ a displacement increment Δu^{tr} is supposed from which trial slip rate $v^{tr} = (\Delta u^{tr})/\Delta t$ and trial $\theta = \theta^{tr}$ are determined. When the convergence criterion is satisfied, the trial values are taken as the solution for that time step.

4.4 Numerical Test Cases

With the procedure outlined above, a number of different numerical simulations have been performed. In Chapter 3, it was noted that the high-speed cutoffs in the friction model (3.7.a) or (4.8) leads to essentially slip-weakening behavior at high slip rates beyond the cutoffs. In this chapter, a comparison is made between a slip-weakening fault model and a state variable fault model. Slip-weakening model calculations have demonstrated the effect of varying prestress levels expressed in terms of a strength ratio s given by equation (4.1) [Andrews, 1976, 1985; Day, 1982]. With a state variable fault friction model, the prestress or initial stress in a problem is established by specification of the initial fault slip rate and the initial state variable, or time of contact. A given value of s does not uniquely define a fault initial condition, but, rather, it can be established through an infinite number of initial conditions. Calculations using two approximately equal s values, determined from two distinct sets of initial conditions, are presented to demonstrate this nonuniqueness. Finally, the effects of different applied normal stresses and of different friction model parameters d_c are considered in a general way. Except for parameter d_c, friction model parameters are identical in all of the calculations, as are the seismic wave speeds. The assigned parameter values are given in Table 4.1, along with graphical estimates of length L_c beyond which the crack growth is not forced.

4.4.1 Slip Weakening Calculations

The numerical simulations of dynamic plane-strain slip weakening fault rupture presented in Andrews [1976 and 1985] provide reference points for the model calculations discussed here. As noted in Andrews's discussions, the rupture velocity of a slip weakening crack is determined by the fault length referred to the critical crack length L_c given in equation (2.1) and by the peak yield stress characterized by the parameter s defined in equation (4.1). Because of the finite peak yield stress defined in a slip-weakening fault constitutive relation, the cohesive zone crack tip can propagate at speeds greater than the terminal rupture speed for an elastic-brittle crack. If s is greater than 1.77 a dynamic plane-strain crack will always propagate at rupture velocity v_c less than Rayleigh wave speed v_R. If s is less than 1.77 and if the crack tip has propagated a sufficient amount, values of v_c greater than v_R are possible as the traction build-up associated with the S-wave reaches τ_p [Burridge, 1973; Andrews, 1985].

Analysing the possibility of super-Rayleigh rupture speeds, Andrews [1976 and 1985] highlights the transition in the growth of the crack, beginning when the crack tip first begins to propagate at $v_c > v_R$ and ending when the trailing edge of the cohesive zone begins to propagate with speeds near v_p. Specifying a small value of s is analogous to imposing the initial stress condition that τ_0 is nearly τ_p and the fault is initially close to failure. At small s, the transitional crack behavior occurs at crack lengths slightly greater than L_c. With larger values of s, the crack has to propagate over a longer crack length before this transition occurs. For s less than about 0.5, the rupture transition from sub-Rayleigh to super-shear is overshadowed by the forcing of the crack tip advance used to establish the critical crack length, and, at s greater than about 1.0, grid resolution was found to be inadequate [Andrews, 1976 and 1985].

The first two model calculations are performed with a slip weakening friction model identical to that used in Andrews's calculations and sketched in Figure 4.1 . Elastic

whole-space parameters are those listed in Table 4.1 . Initial stress is assumed to be 58.7 bars and normal stress is 100 bars. Peak stress and residual stress in the model are 61.1 bars and 56 bars, respectively, so that **s** = 0.9 . The calculations feature different values of d_r: a "laboratory smooth" 5 μm and a "laboratory rough" 20 μm, and numerical grid spacings are adjusted in order to maintain resolution of the cohesive zone.

The rupture propagation histories from these two calculations are pictured in Figure 4.2 , as time-vs-position plots showing the position of the crack tip cohesive zone. At times and positions below the shaded area, the fault is locked. In the shaded area, the fault is slipping with non-zero slip rate and fault slip has not yet reached d_r; this area can be interpreted as the cohesive zone or the crack end zone. Above this area, fault slip has reached d_r and the fault is sliding at residual stress level τ_r.

The direct scaling effect of the critical fault slip weakening displacement is readily seen. The two sets of results are plotted on axes with scales that differ by a factor of 4, both on the vertical and horizontal. Otherwise, the plots are identical. L_c is directly dependent on d_r: values are estimated to be 30 - 35 cm for the "smooth" calculation and about 120 -140 cm for the "rough" calculation. At $L \approx 11\ L_c$ in both simulations, rupture velocity achieves v_R. At $L \approx 16\ L_c$ the crack tip skips ahead and accelerates from v_s. Beyond $L \approx 21\ L_c$, the trailing edge of the end zone advances at v_p.

4.4.2 Rate- and State-Dependent Calculations

With the velocity cutoffs included in the rate- and state-dependent friction model (4.8), slip weakening-like fault behavior is expected at fault slip rates greater than the cutoffs and a similar rupture transition to that discussed above might reasonably be expected. If an initial value $\theta_0 = 300$ s is assumed, then **s** = 0.88 is realized by assuming an initial $v_0 = 10^{-8}$ m/s. Simulations TH300A and TH300B are carried out using these uniformly imposed initial conditions with σ = 100 bars acting on a "smooth" fault, that is, with constitutive

parameter $d_c = 20 \times 10^{-6}$ m, and a "rough" fault $d_c = 5 \times 10^{-6}$ m. In all of these calculations, the grid sizes are adjusted to allow resolution of the crack end zone.

The results from these simulations are displayed in Figures 4.3 and 4.4, in the same fashion as those from the slip weakening calculations. As mentioned earlier, a basic difference between slip weakening and fault response governed by a state variable friction model is that the state variable model used in this study assumes that there is always some amount of sliding taking place along the fault. In Figures 4.3 and 4.4, the areas below the hatched areas in the figures include those "locked" positions on the fault at which slip rate is still at the initial value of v_0. The shaded areas are regions where the fault is sliding with slip rate v greater than v_0. The lightly shaded areas indicate the region in which slip is accelerating from the initial slip rate v_0 to balance increases in traction with the direct velocity frictional response. The darker areas represent the dynamic crack end zone. The onset of dynamic slip, or the end of quasistatic sliding as used in some of the quasistatic numerical models [Dieterich, 1981; Mavko, 1983; Tse, 1985], is understood as the time when fault slip rate first exceeds a specified limiting slip rate. We interpret the end zone of the dynamic crack to be that region in which the slip rate is greater than this cutoff, $50\ f_3$ is used here, and where the traction on the fault has not fully dropped to τ_r. Above the shaded areas, the fault is sliding at approximately the "residual" stress level imposed by the high-speed cutoffs in the friction model (4.8). In these calculations, the rate of advance of the leading edge of this dynamic end zone - the dynamic crack tip - is regarded as the crack rupture velocity v_c. Critical crack lengths L_c beyond which the rupture velocity is greater than the forced rupture speed $(0.5)v_R$ are estimated graphically from these time-vs-position plots rather than estimated theoretically from equation (2.1).

In TH300A and TH300B, similarities to the slip weakening calculations are observed. Recall from Section 4.3 that the evolution law governing the state variable θ was chosen so that the constitutive friction model parameter d_c roughly corresponds to the critical

slip weakening displacement parameter d_r appearing in the slip weakening model. It might be expected that d_c in the state variable frictional crack model plays a similar role to that played by d_r in a slip weakening fault model in controlling the size of the critical crack. L_c estimates are ~ 300 cm and ~ 50 cm for TH300A and TH300B, respectively. Critical crack lengths, then, appear to depend directly on the value of d_c used in the state variable friction model.

Time histories of traction, fault slip rate and fault displacement calculated for three positions along the fault in test TH300A are shown in Figure 4.5 . The three positions correspond to locations shortly after the development of the critical crack at $x = 1.2\ L_c$, before the jump, at $x = 3.8\ L_c$, and after the transition to super shear crack velocity at $x = 6.3L_c$. Before the transition in rupture speed, the crack is driven with the traction peak at the time of the Rayleigh wave. Following the transition, the onset of failure coincides with the arrival of the S-wave as shown in the result for the position $x = 6.3\ L_c$.

Features of the rupture growth also bear resemblance to those observed in the slip weakening crack models. In both cases TH300A and B the rupture quickly accelerates toward v_R. Considering test TH300A, in Figure 4.3, the crack accelerates out of the forced nucleation stage and propagates stably at $v_c = (0.87)v_s$, failing to reach $v_R = (0.91)v_s$ before the jump to super-shear v_c. The crack tip suddenly jumps ahead at $L \approx 5.4\ L_c$, and the crack tip begins to propagate with rupture velocity from v_s toward v_p. The jump in the trailing edge of the end zone occurs at $6.2\ L_c$ and the trailing edge propagates at v_p for the remainder of the calculation. In test TH300B, v_c reaches v_R at $L \approx 4.4\ L_c$. At $L \approx 6.2\ L_c$, the crack tip suddenly jumps ahead and begins to accelerate from v_s to rupture velocity approaching the P-wave speed. The trailing edge of the cohesive zone at $L \approx 7.2\ L_c$ jumps ahead and propagates at v_p for the remainder of the calculation.

The specification of a different value of v_0 with the initial value of θ_0 held at 300 s changes the value of the strength ratio s. Both the peak and the residual shear stresses will

remain unchanged, but if v_0 is increased to 10^{-7} m/s the initial stress increases and the value of **s** decreases to 0.56 . The slip weakening models of Andrews [1985] predict that the rupture velocity transition from sub-Rayleigh to super-shear takes place at smaller L. The value of **s** = 0.56 is used in TH300C. It is observed in this calculation that this transition occurs at crack length L such that $2.7\ L_c < L < 3.4\ L_c$ (Figure 4.6).

Another difference between a slip weakening fault constitutive relation and the rate- and state-dependent friction constitutive relation is that, for a given set of slip weakening model parameters, specifying a value of **s** uniquely determines the initial fault stress τ_0. With a state variable friction model, this is not the case, as one **s** can be produced from an infinite number of initial (θ_0, v_0) pairs. This feature of the rate- and state-dependent friction model is displayed in Figure 4.7 which is the same set of μ-vs-log θ relations for specific slip rate values plotted in Figure 3.1a . The dashed line in Figure 4.7 is a curve of constant **s** = 0.88, such that any point on this curve would be a suitable set of initial fault conditions to establish this **s** value. The points labelled A and C indicate the initial conditions assumed for tests TH300A/B and TH300C, respectively.

Because the rupture transition discussed above depends on the value of **s** associated with the calculation, all (θ_0, v_0) pairs along the constant **s** curve should produce similar rupture transition behavior. Test T30D20 was run, assuming $(\theta_0, v_0) = (30\text{ s}, 10^{-7}\text{ m/s})$ indicated by the point labelled D in Figure 4.7 , and the corresponding time-vs-position plot of the end zone is given in Figure 4.8. Following the forced nucleation, the crack tip propagates smoothly at $v_c = (0.86)v_s$. At $L \approx 6\ L_c$, the crack tip jumps ahead and accelerates from the shear wave speed. The results of this calculation are quite similar to those obtained in TH300B, except for the slightly larger L_c in T30D20 due to the smaller absolute stress differences in this calculation.

Two tests TH300E and TH300F were run at normal stresses of 50 and 200 bars, respectively. In terms of the time-position behavior of the cohesive zone, the results from

these two runs are very similar to those from TH300A. With the different normal stresses acting on the fault, however, L_c estimates are larger for lower normal stress.

4.5 Discussion and Conclusion

From these test cases, it appears that the rupture velocity of dynamic plane-strain shear cracks governed by a rate- and state-dependent friction constitutive relation, as in the case of a crack subject to a slip weakening friction law, depends on the initial stress and on the crack rupture length. As the crack grows beyond its critical length L_c, rupture velocity increases, initially toward the Rayleigh wave speed and then, depending on the prestress level, it jumps to the shear wave speed and accelerates toward the P-wave speed. Larger values of d_c in the friction model result in longer critical cracks, so that rough simulated faults, larger d_c, are associated with larger L_c and a crack propagating along a rough fault does not accelerate as rapidly as one along a smooth fault surface. This feature of dynamic crack growth is consistent with the laboratory observations of stick-slip failures generated on smooth and rough simulated faults that were presented in Chapter 2. As noted by Day [1982], **s** is perhaps lower for the laboratory stick-slip events than the value of **s** = 0.88 used here. With lower **s**, the rupture acceleration is observed to be advanced so that higher rupture velocities might be reasonably expected over the same distance intervals. The **s** value was chosen here in order to highlight the unstable transition in rupture velocity as a first indicator of the crack behavior under the state variable friction law.

The unstable transition in rupture velocity for a certain range of the **s** strength ratio (equation 4.1) is interpreted as a strong indicator of the similarity of the behavior of cracks following a rate- and state-dependent fault friction law to that for a crack subject to a slip weakening constitutive relation. The specification of high-speed cutoffs for the velocity-dependent frictional behavior essentially limits the frictional response during rapid stick-slip sliding to one which is slip weakening, and a meaningful interpretation of limiting

maximum and minimum frictional strengths is derived completely from the friction model. This suggests that theoretical analyses of the dynamic fracture process like those presented by Burridge *et al.*, [1979] are applicable to dynamic frictional instabilities.

In the context of the rupture velocity transition, there are important distinguishing features of the state variable friction model. From the slip weakening models, it is noted that a strength-to-prestress ratio s must be less than a critical value before super-Rayleigh rupture propagation can be supported. It is noted above that a given s does not uniquely fix the fault initial conditions in the state variable dynamic calculation as it does in a slip weakening calculation. Numerical tests with two different sets of initial (θ_0, v_0) conditions, both giving the same s, produce similar transitional rupture behavior. The unstable transitions in the state variable calculations, however, apparently occur sooner with respect to L_c than in slip weakening calculations with the same s. Although the criteria used to define the onset of stick-slip and to estimate the size of L_c are probably not sufficient to establish the difference between rupture velocity transitions at lengths 5.4 L_c and 6 L_c in tests TH300A and T30D20, it seems reasonable to interpret these lengths as significantly shorter than 16 L_c where the same jump in rupture velocity occurs in the slip weakening calculation. The state variable friction model assumes that there is always some non-zero slip rate v and, unlike a slip weakening fault, the fault is never truly stationary. The shorter distances to rupture velocity transition in the state variable calculations are possibly related to this assumption.

With the implementation of the laboratory-based friction model into the numerical modeling of dynamic shear cracks, a physical basis for understanding fault unstable behavior is provided, especially for fault conditions which are readily imposed in laboratory tests. This underscores the obvious importance of laboratory studies of the frictional behavior of simulated faults to studies of the behavior of natural faults, not only leading up to the time of unstable failure but also through the episodes of unstable slip. Complete analyses of the mechanical behavior of a fault governed by a rate- and state-dependent friction constitutive

model, such as those in Tse [1985], and of the energetics of shear crack propagation are probably required to fully understand the fault nucleation and propagation processes. With less arbitrary criteria for estimating L_c and for identifying the onset of dynamic slip, additional detail can be provided to the understanding of the stick-slip frictional instability.

Table 4.1 . Parameters of Crack Simulations

test	$d_c(\mu m)$	$\theta_0(s)$	$v_0(m/s)$	$\sigma(bars)$	Lc(cm)
TH300A	20.0	300	10^{-8}	100	~300
TH300B	5.0	300	10^{-8}	100	~ 50
TH300C	20.0	300	10^{-7}	100	~150
T30D20	20.0	30	10^{-7}	100	~350
TH300E	20.0	300	10^{-8}	50	~600
TH300F	20.0	300	10^{-8}	200	~150

$$c_1 = 0.56,\ c_2 = 0.013,\ c_3 = 30.0/s$$

$$f_1 = 1.0,\quad f_2 = 0.010,\quad f_3 = 2.0 \times 10^{-4} m/s$$

$$G = 2.5 \times 10^5 \text{ bars}$$

$$v_p = 5.02 \text{ km/s},\quad v_s = 2.9 \text{ km/s}$$

Figure Captions

Figure 4.1 . Slip weakening fault constitutive relation.

Figure 4.2 . Time-vs-position plot of rupture history of slip weakening fault. Shaded area represents fault cohesive zone. Areas below shaded areas represent unslipped portion of fault during calculation. Above shaded areas, fault is sliding at residual friction stress level. Cases plotted are for d_r = 5 μm and d_r = 20 μm.

Figure 4.3 . Time-vs-position plot of rupture history of fault governed by state variable friction model, case TH300A. Lightly shaded area indicates region of accelerating fault slip preceding instability. Darkly shaded area represents fault cohesive zone. In regions corresponding to the part above the shaded areas, fault is sliding at "residual" stress level.

Figure 4.4 . Same as 4.3 for TH300B, for which only parameter d_c is changed to 5 μm.

Figure 4.5 . (a) Stress as a function of time in test TH300A for positions at 1.2 L_c, 3.8 L_c, and 6.3 L_c. (b) Slip rate time histories for same three positions in TH300A.
(c) Fault slip histories for same three positions in TH300A.

Figure 4.6 . Same as 4.3 for TH300C. Initial fault slip rate is uniformly changed to 10^{-7} m/s, decreasing s to 0.56.

Figure 4.7 . μ-vs- log θ diagram for friction model and parameters used in dynamic modeling. Points labeled A, C, and D represent initial fault state conditions for tests TH300A/B, TH300C, and T30D20, respectively. Dashed line represents initial conditions for which s = 0.88 .

Figure 4.8 . Same as 4.3 for T30D20. Initial fault slip rate is increased to 10^{-7} m/s and initial θ is changed to 30 s so that s = 0.88 as in TH300A and TH300B.

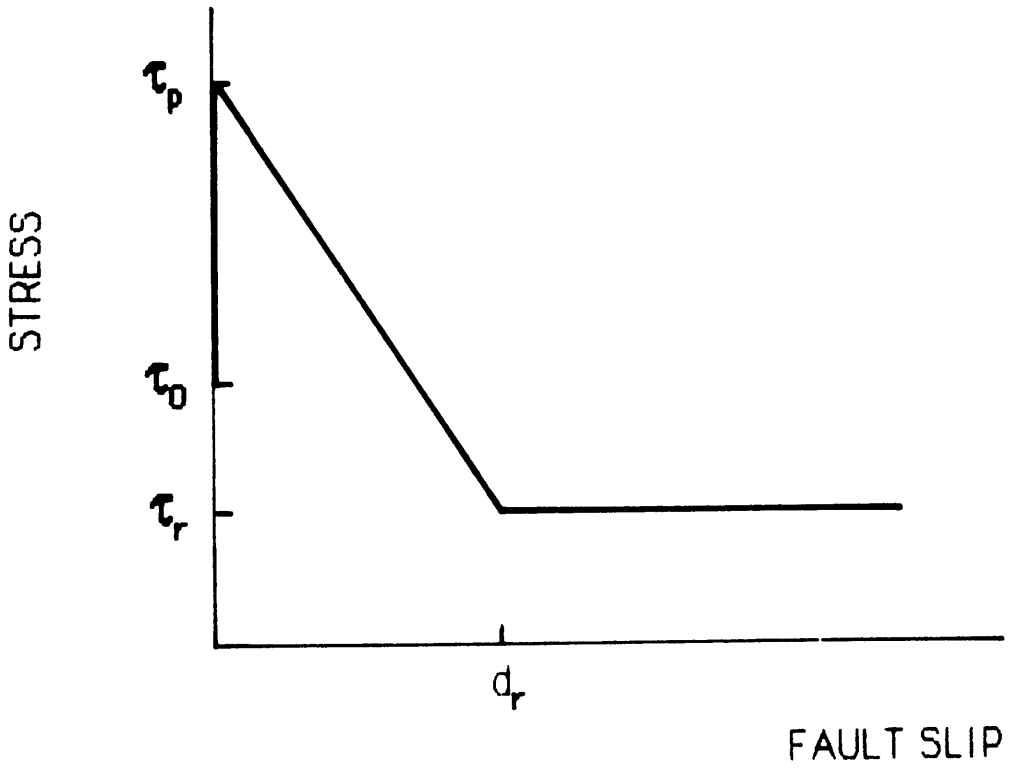

$$S = \frac{\tau_p - \tau_0}{\tau_0 - \tau_r}$$

Figure 4.1

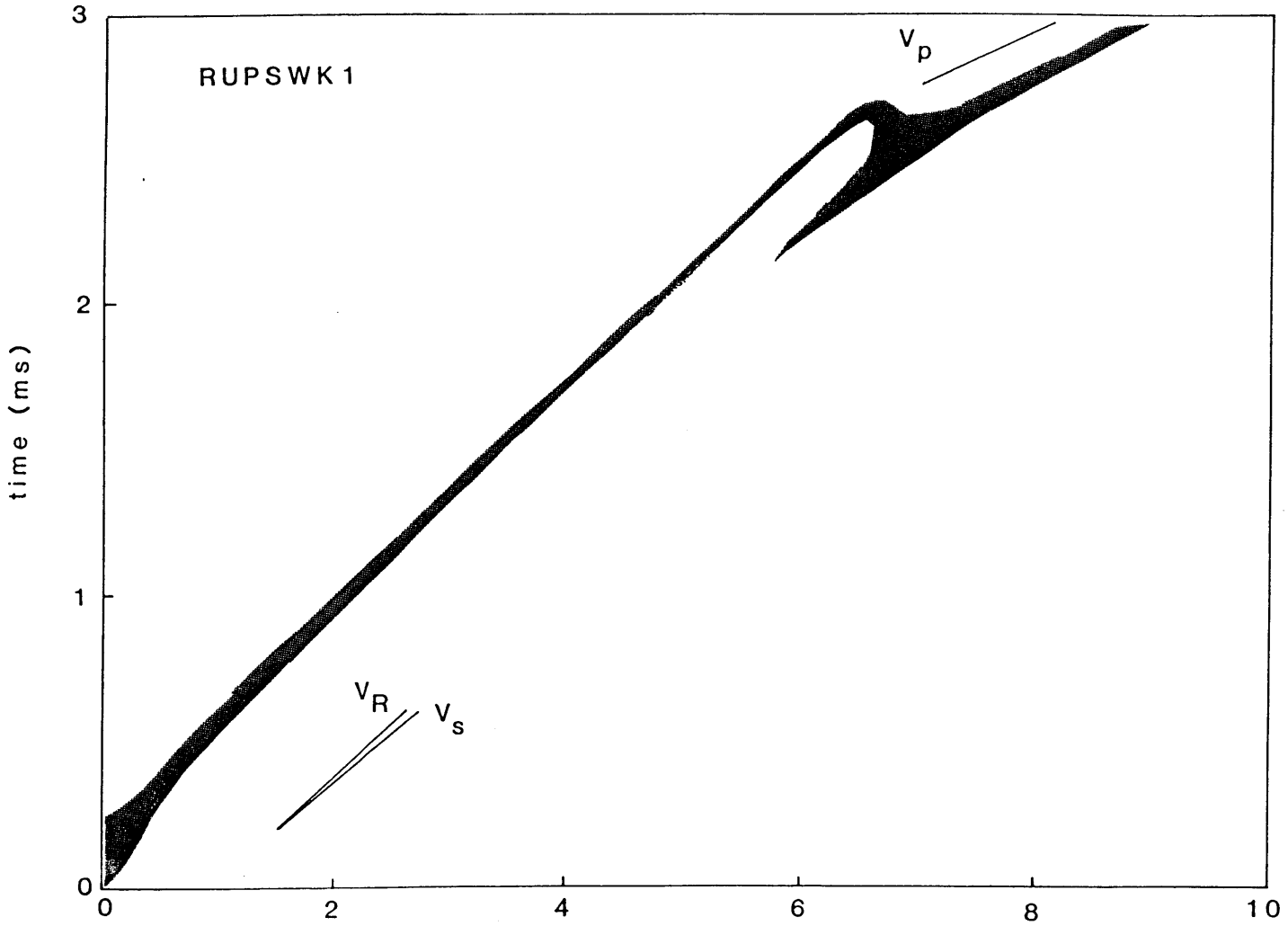

Figure 4.2

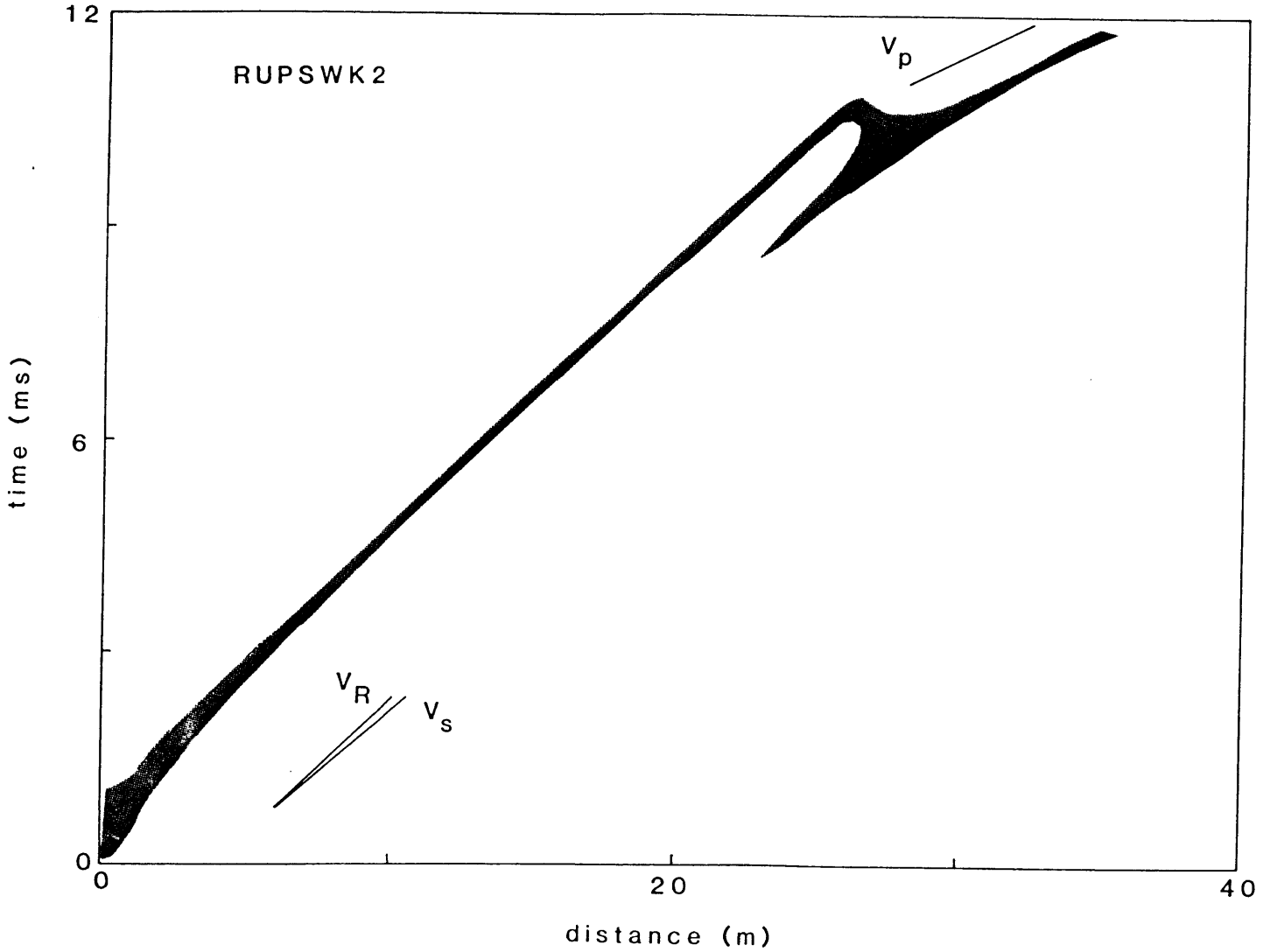

Figure 4.2

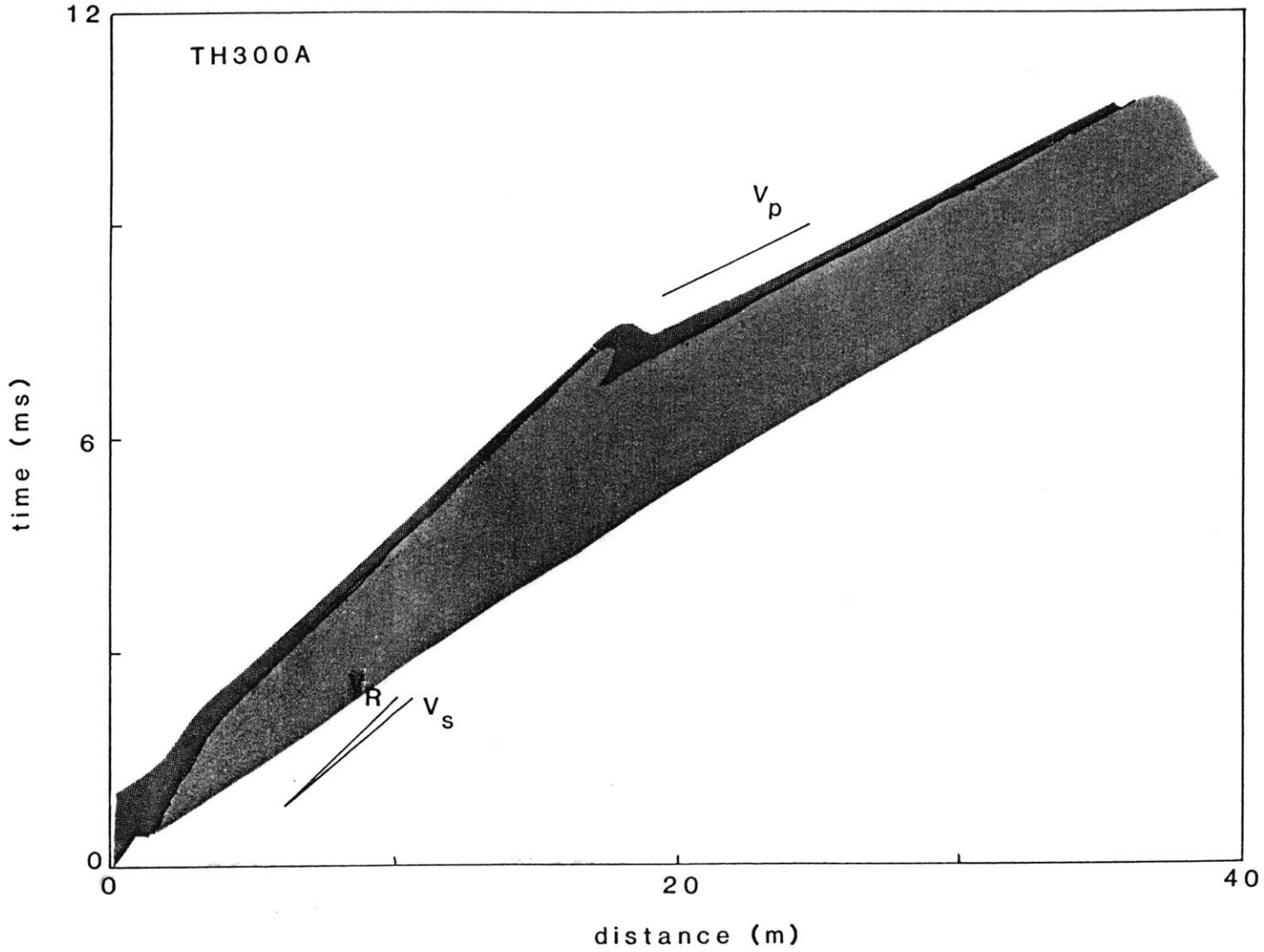

Figure 4.3

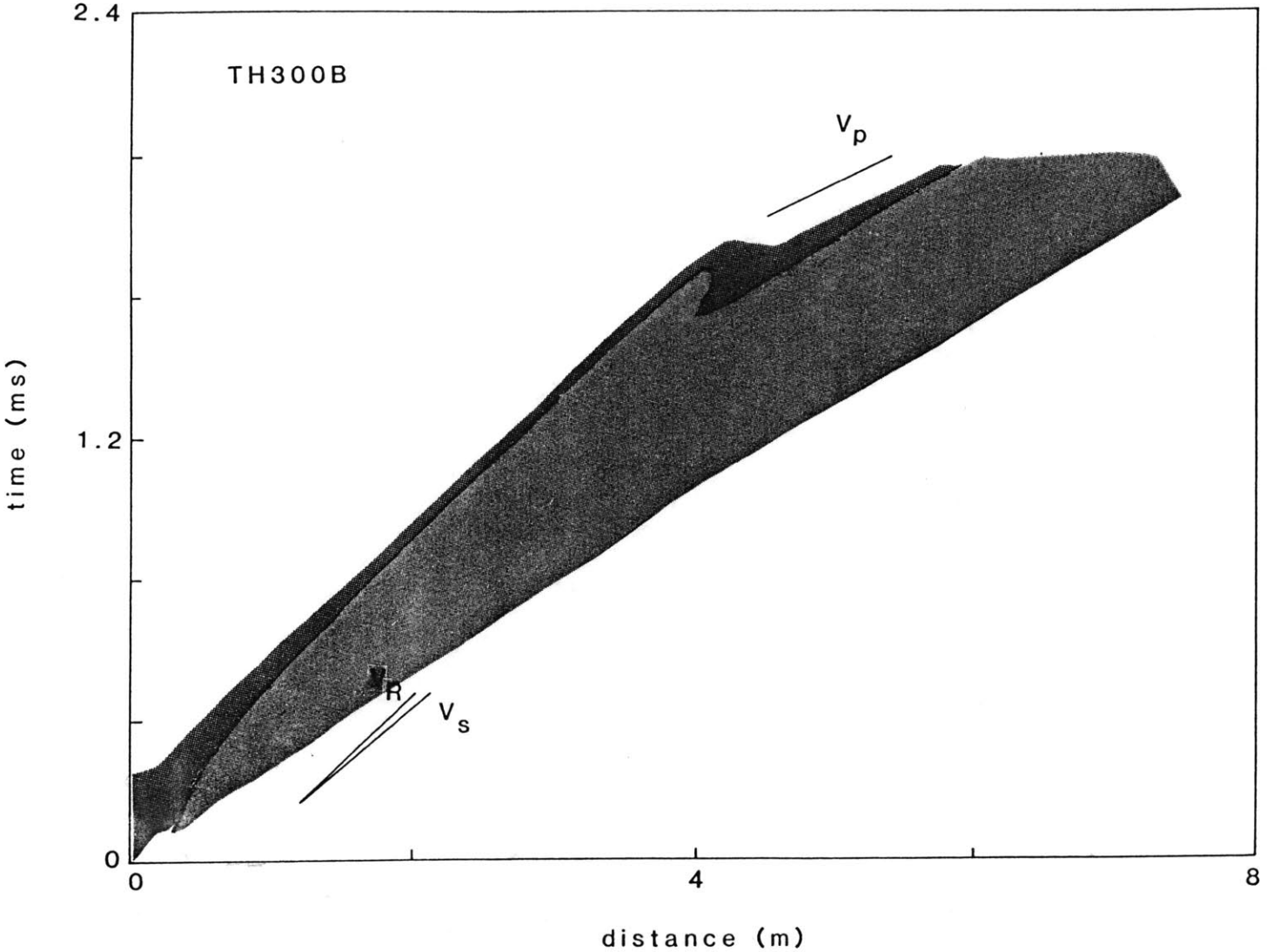

Figure 4.4

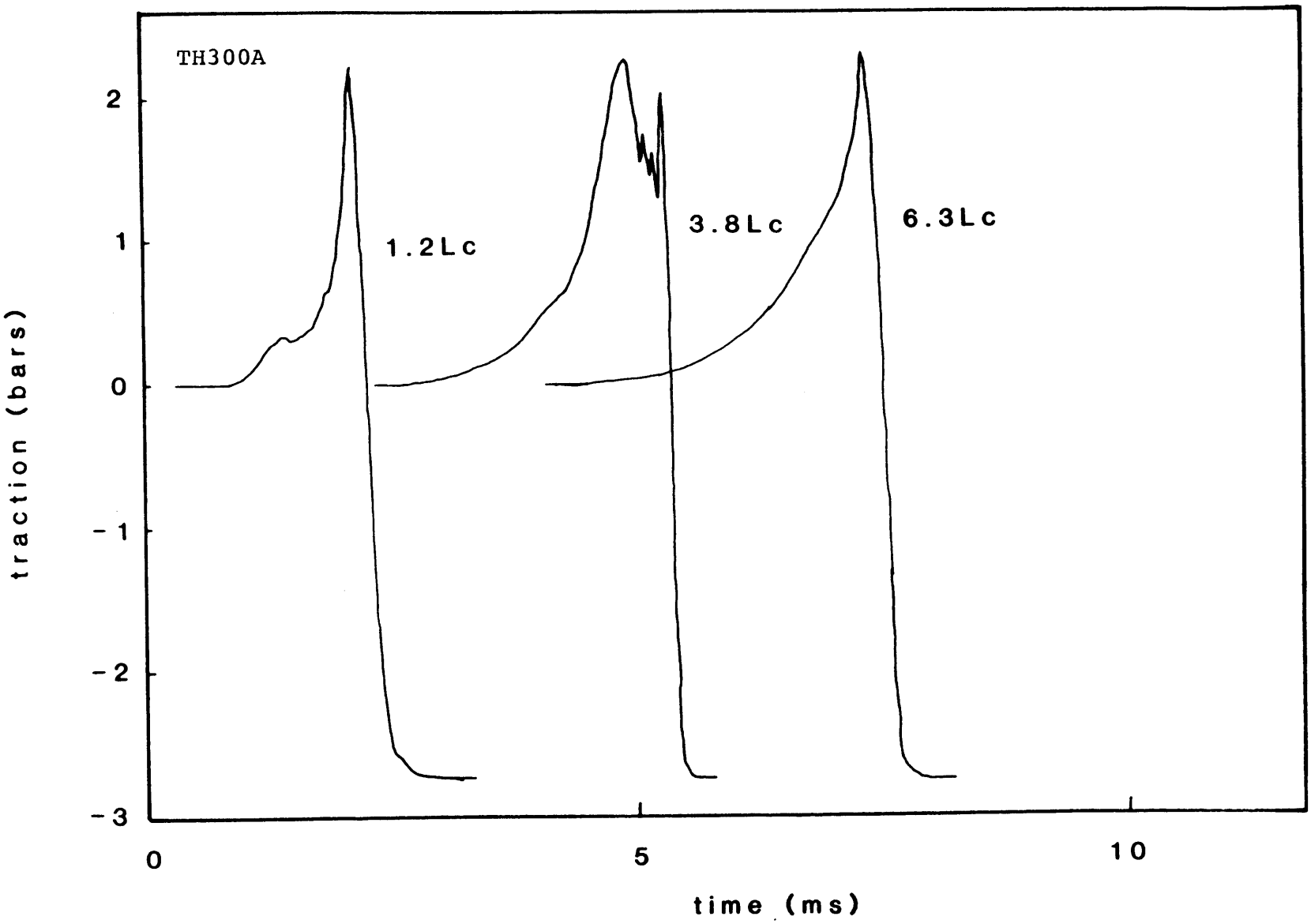

Figure 4.5a

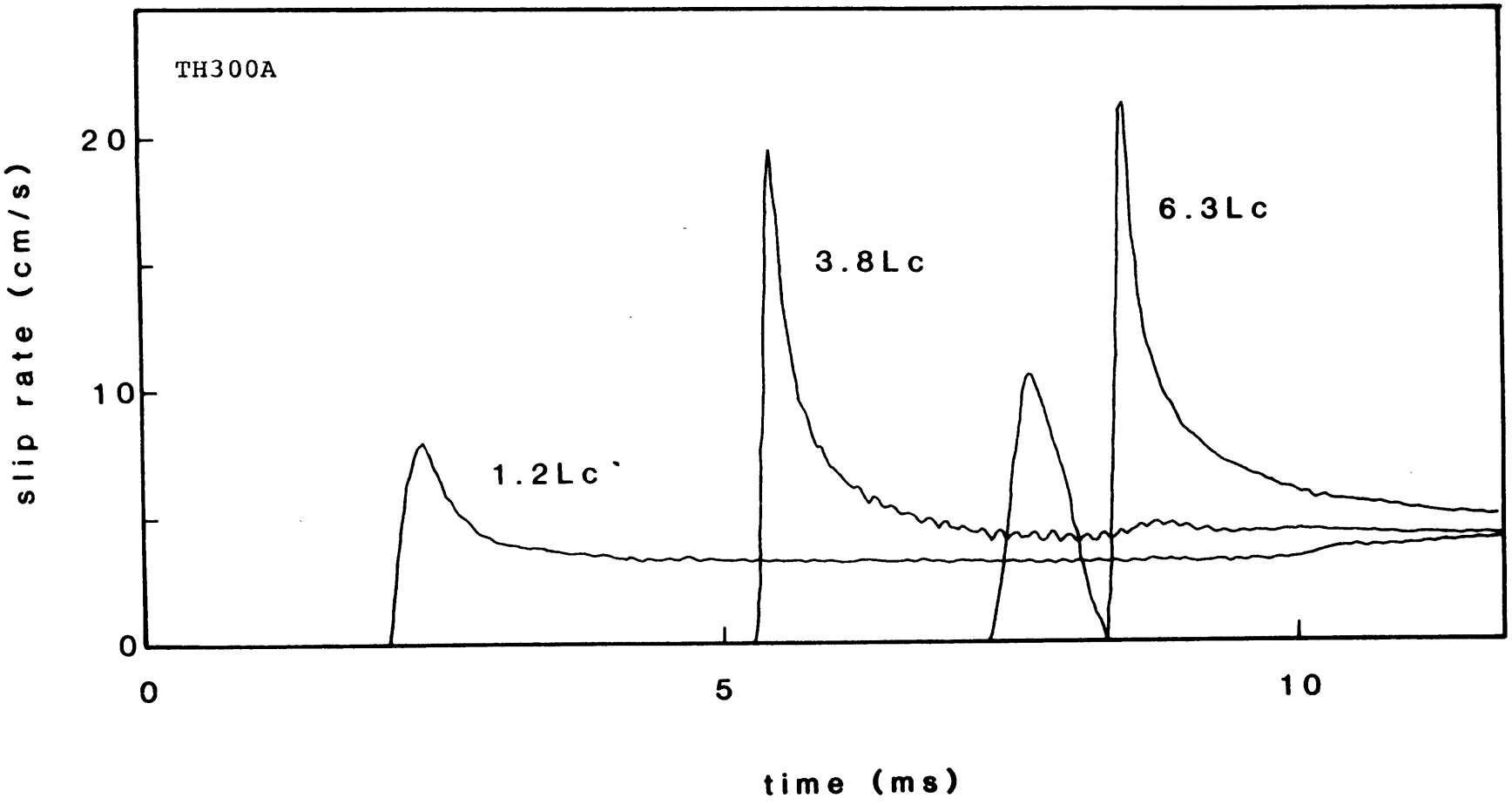

Figure 4.5b

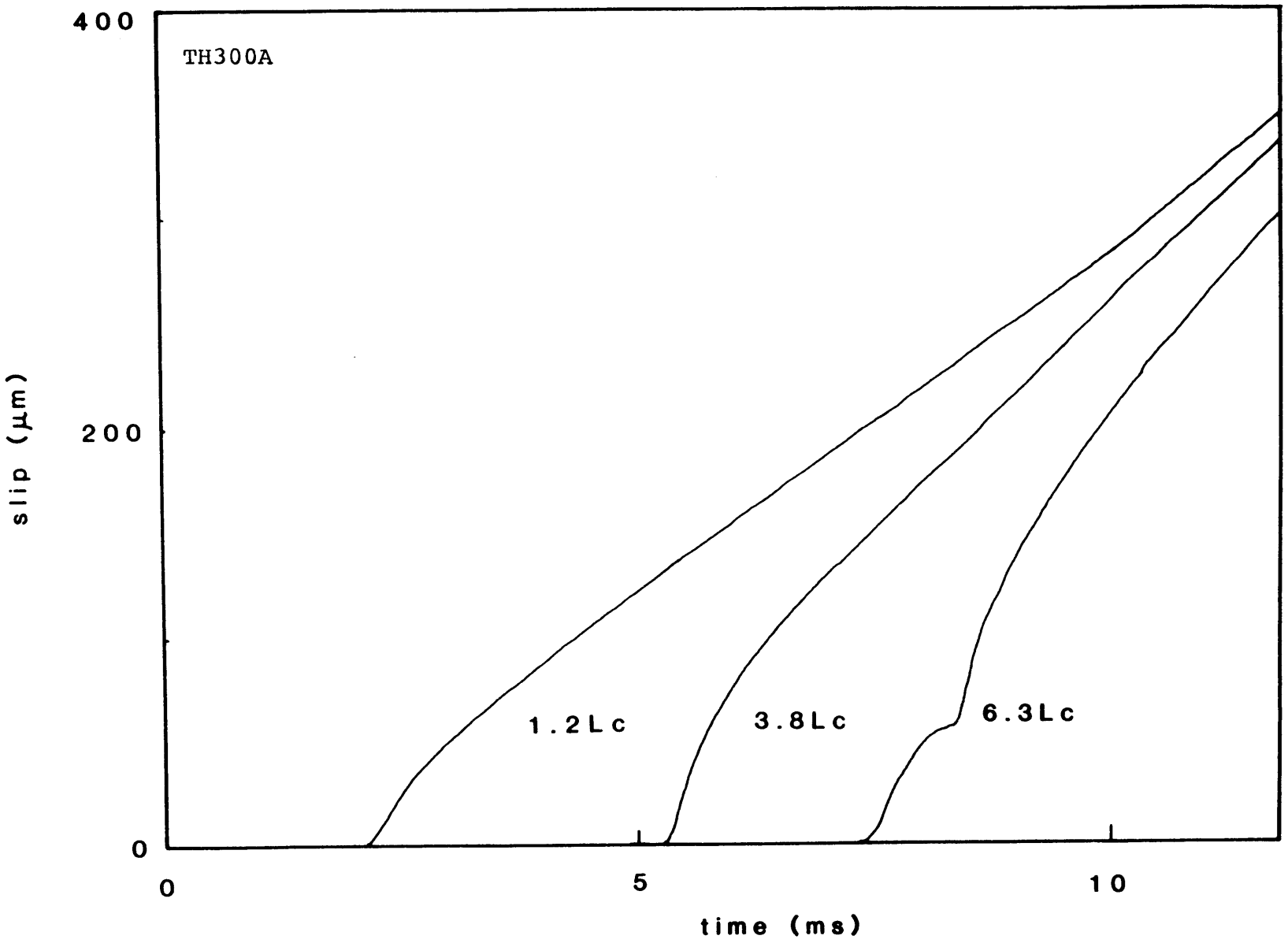

Figure 4.5c

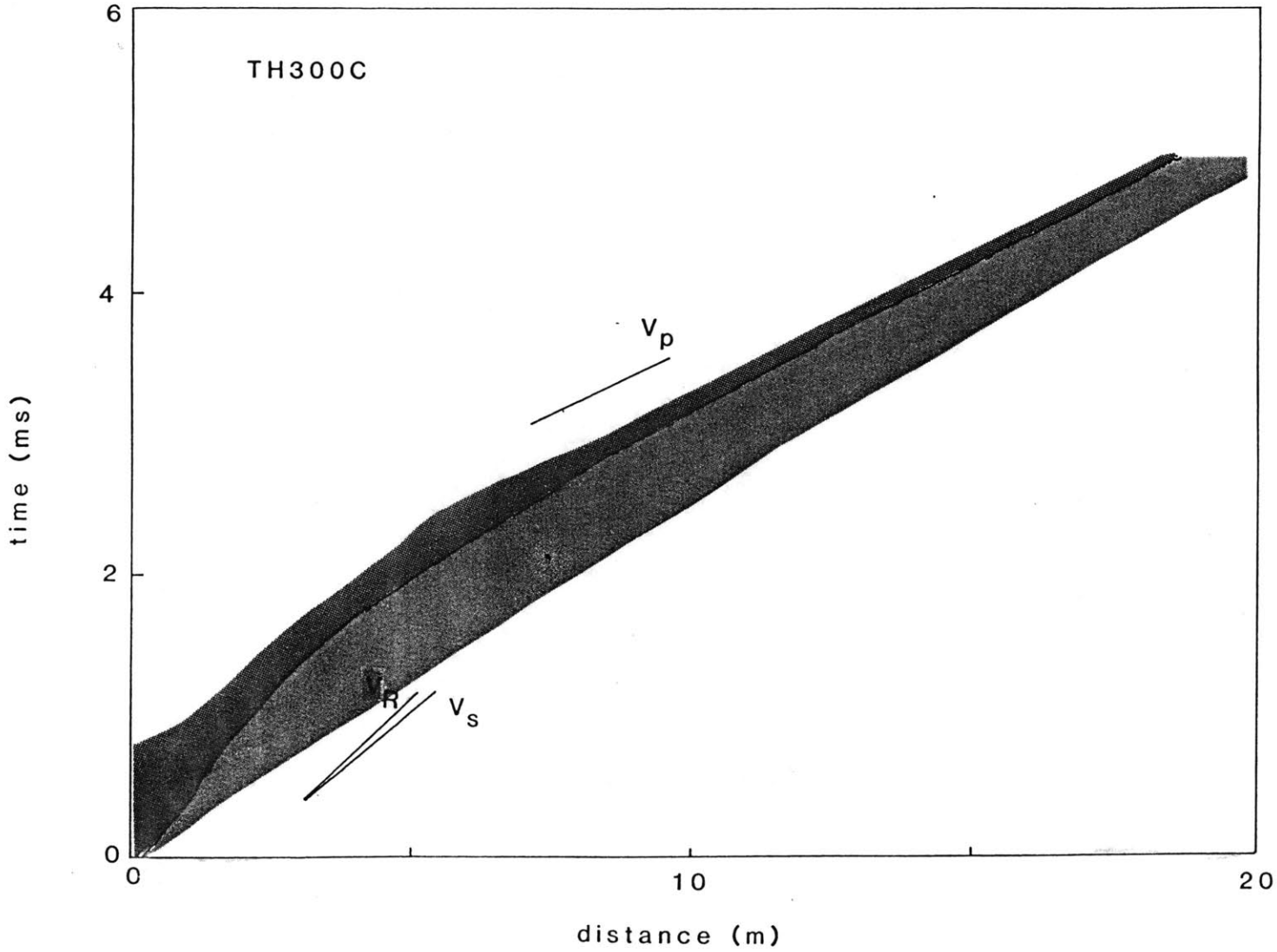

Figure 4.6

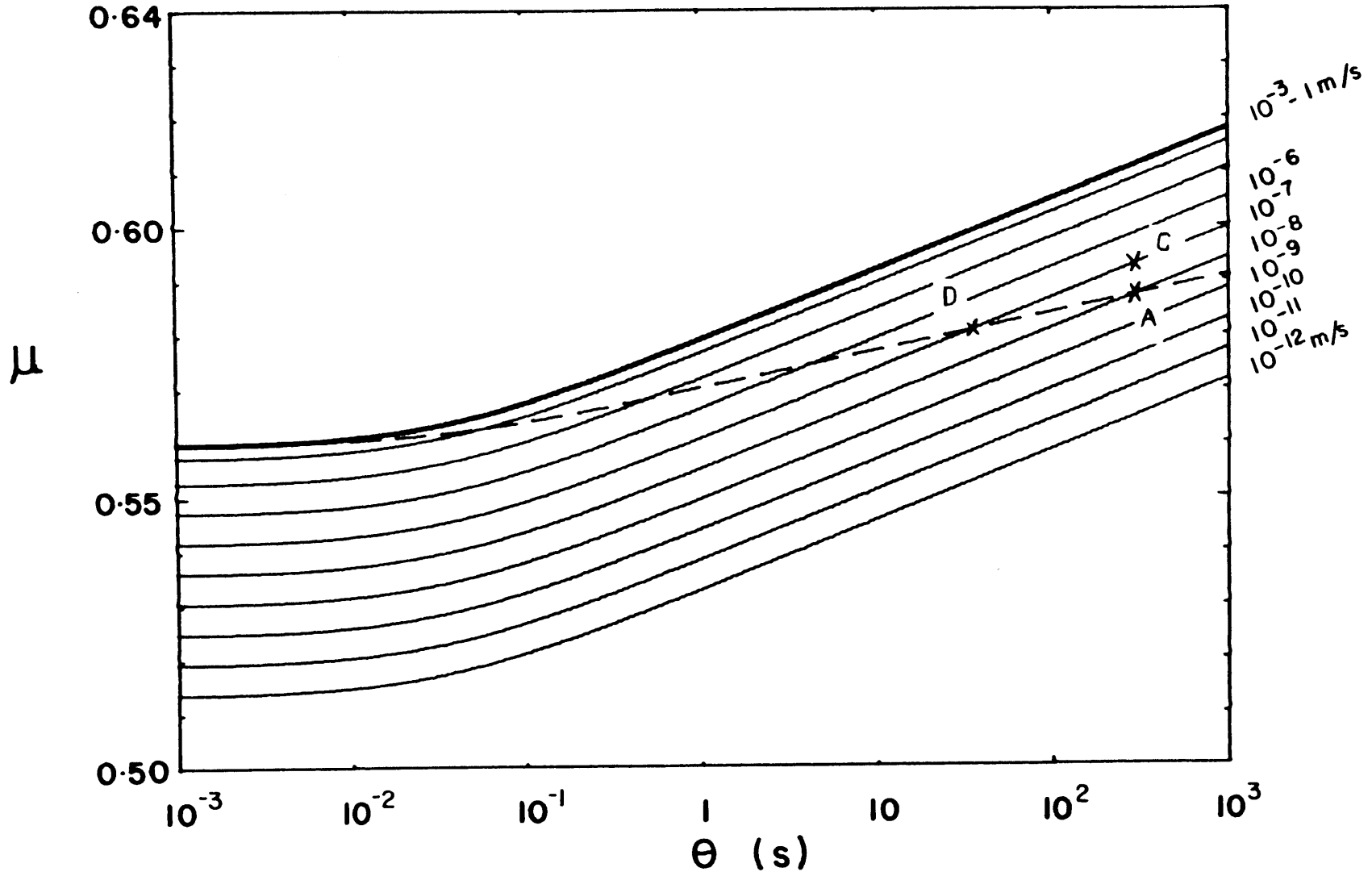
0·64
0·60
0·55
0·50
μ
10^-3
10^-2
10^-1
1
10
10^2
10^3
Θ (s)
10^-3 m/s
10^-6
10^-7
10^-8
10^-9
10^-10
10^-11
10^-12 m/s
A
C
D

Figure 4.7

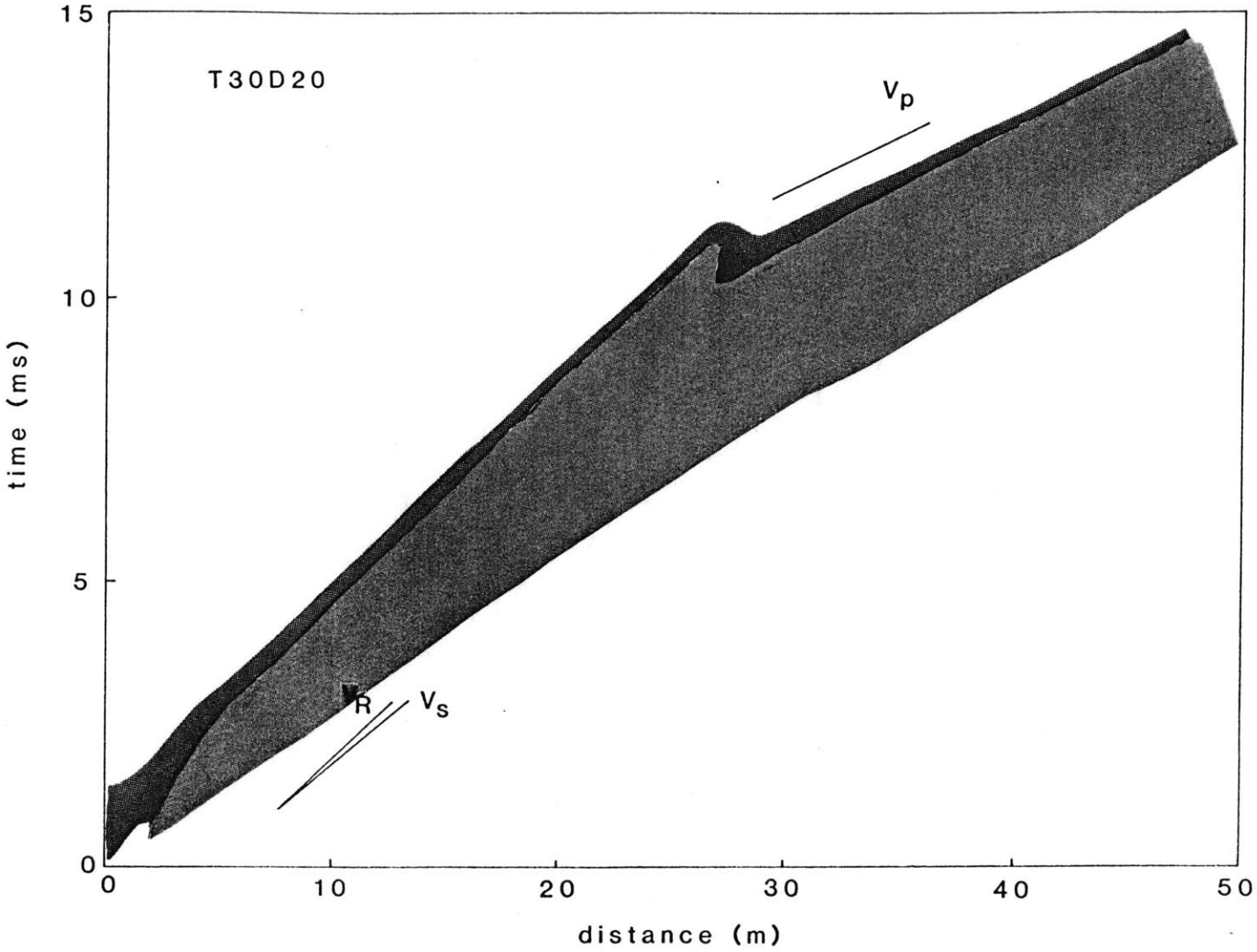

Figure 4.8

Chapter 5 - Length Scales for Earthquakes

5.1 Introduction

Experimental and numerical models of dynamic frictional instability have been discussed in the preceding chapters of this thesis. The laboratory experiments afford detailed observations of frictional instabilities, stick-slip events, that were generated on simulated fault surfaces. Due to the large size of the test samples and high-speed recording capability of the electronics, it is possible to clearly observe characteristics of unstable frictional sliding which suggest that stick-slip sliding can be appropriately considered as a dynamic shear crack extension process. In addition to providing estimates of various stick-slip source parameters and suggesting possible scaling relations among these parameters, the stick-slip observations also suggest a more general applicability, to conditions of high-speed slip on sliding surfaces spreading dynamically over a pre-existing fault surface, of laboratory-based friction constitutive relations which were motivated by observations of sliding along simulated fault surfaces under quasistatic conditions. Despite differences which arise from features of these slip rate- and state-dependent friction constitutive relations, when a friction model of this type is used to specify the fault response in numerical simulations of dynamic crack growth, the numerical results do exhibit similarities to those obtained with a widely used cohesive zone crack model, *i. e.*, a slip weakening model.

The dynamic rupture calculations using a state variable friction model indicate that there exists a critical length for initiating dynamic rupture on frictional faults. Using such a critical length as a scaling factor for experimental observations, it is possible to provide a common general interpretation to data taken from different experiments and with different fault conditions. The critical length is related to a characteristic fault slip parameter d_c in the friction model. As in a fault slip weakening model, this characteristic slip is a displacement measure of the duration of the evolution toward constant frictional resistance under constant-

velocity slip. At this point, we begin to address the question of, if there are analogous critical lengths for earthquakes, what might suitable values of L_c, or equivalently d_c, be for natural faults?

For simulated faults, d_c is affected by fault roughness and, if gouge is introduced onto the sliding surface, it is also affected by the nature, i. e., particle size or gouge type, of the gouge layer. In general, the rougher the fault surface and the coarser the fault gouge are, the larger the observed d_c value is. It is generally suggested that, because the simulated faults are extreme idealizations of natural faults, even larger values of d_c might be appropriate for modeling natural faults. In numerical simulations of crustal fault behavior, values of d_c as large as 10 cm are required to match observations of earthquake recurrence [Mavko, 1983; Tse, 1985].

5.2 Spectral Properties of Stick-Slip Sliding

To begin looking into the notions of identifying and evaluating possible physical length scales for earthquakes, we return to the laboratory to take one last look in this thesis at data from the stick-slip instabilities generated on the simulated faults. In the initial presentation of the laboratory data in Chapter 2, it was suggested that the observation of the fault slip weakening-like behavior at the onset of stick-slip sliding indicated that the stick-slip instability is appropriately included in the general classification of cohesive zone fault models. In this discussion, we will elaborate on that earlier suggestion and discuss ways in which cohesive zone crack tip behavior can also be expressed.

Considering the fault cohesive zone to be that part of the fault surface on which the stress at any given time is at a level between its peak value and its residual value. This is pictured on the left side of Figure 5.1 with hypothetical distributions of stress and fault displacement sketched as a function of position along the fault. The cohesive zone has length ω_c, where, in the theoretical development of the cohesive zone crack models, ω_c is chosen in

order to cancel the $r^{-1/2}$ crack tip stress singularity. Assuming that the crack is propagating steadily at a constant rupture velocity v_c, the weakening time required for the entire cohesive zone to propagate past the position X is obviously

$$t_\omega = \omega_c / v_c. \qquad (5.1)$$

From the time that the peak stress is achieved to the time t_ω, the stress at X decreases from τ_{peak} to $\tau_{residual}$. Within the cohesive zone, displacements u are less than observed d_r proportional to d_c. The variations in stress and fault displacement as a function of time at X are shown on the right side of Figure 5.1 . The rate- and state-dependent friction models incorporating high-speed cutoffs feature inherent maximum peak and minimum residual stress levels.

The simple equation (5.1) has some rather obvious implications. First, if $\omega_c = 0$, then $t_\omega = 0$ and the stress drop $\tau_p - \tau_r$ would occur instantaneously. The size of the cohesive zone is estimated, as mentioned in Chapter 2, by rearranging (5.1) . Frequency $f_\omega = t_\omega^{-1}$ exists such that f_ω increases with decreasing cohesive zone size ω_c. This frequency is a characteristic of the cohesive zone size. Finally, the time t_ω represents the departure in the stress time history from a step function. Therefore, a corner frequency appears at f_ω; at frequencies $f > f_\omega$, the fault stress time histories are diminished in high frequency components with respect to a step function.

Referring to the stick-slip data pictured in Figure 5.2 (initially presented as Figure 2.3), times t_ω are larger for the stick-slip events produced on the rough fault than on the smooth fault, implying that cohesive zone sizes are smaller on the smooth fault and that cohesive zone size on a fault governed by a state variable friction model is directly related to a critical fault slip parameter featured in these friction models. Two possible interpretations of the observed sliding behavior following the onset of stick-slip were given in Chapter 2. The

reasoning presented above would favor the interpretation that, because of the smaller cohesive zone on the smooth fault, stick-slip on the smooth fault generates enhanced high frequency signal compared to the rough fault. The high frequency waves reflect from the sample boundaries and the observed chatter is produced in the stress records.

Fourier amplitude spectra of the stick-slip stress histories shown in Figure 5.2 are calculated using a Fast Fourier Transform (FFT). They are plotted with the original time series in Figures 5.3 a-e from the smooth fault and in 5.4 a-d from the rough fault. The transforms are computed in order to preserve the DC offset (stick-slip stress drop) with signal means subtracted and half-cosine tapers applied to the fronts and backs of the windows.

The spectra in Figures 5.3 and 5.4 are dominated by the f^{-1} roll-offs associated with the DC offset. The smooth fault spectra display amplitude peaks near 20 kHz. The values of f_ω determined from estimates of t_ω are also nearly 20 kHz, as are the frequencies of some of the smaller amplitude signals following the stress drop. To avoid the f^{-1} predominance, transforms are computed for windows of the smooth fault data, excluding the stress drop. These are shown in Figure 5.5 , and they display broad amplitude peaks centered at about 15 kHz. The amplitude spectrum of a hammer blow on the sample recorded at a strain gage is plotted in Figure 5.6 , showing, in addition to a peak corresponding to the sample thickness, a side double-peak also centered about 15 kHz. This seems to confirm the interpretation that the chatter following the stick-slip stress drop is a feature of the sample geometry rather than of the sliding process. Because f_ω is very close to this sample resonance, reliable spectral estimates of ω_c are not allowed by this stick-slip data.

The rough fault data, on the other hand, provide a more encouraging result. In the time domain (refer to Figure 5.2), the rough fault data clearly display the weakening time t_ω, and, once the unstable slip is well-developed, it is observed that t_ω is clearly shorter at positions farther from the rupture nucleation region. This feature, while not unambiguously

seen in the smooth fault data, is observable in all of the rough fault stick-slip data. Above frequencies f_ω, the spectral roll-offs proceed more quickly than f^{-1}. Estimates of ω_c for this rough fault data are given in Table 5.1 . Presumably, even with crude estimates of rupture velocity v_c, cohesive zone size for a dynamic shear crack can be estimated using observed f_ω or t_ω values. A further reduction, described in Rice [1980], is required to obtain estimates of d_c from cohesive zone size.

5.3 Fractal Characterization of Fault Geometry

Not only are natural faults presumably rougher than laboratory faults, but, displaying splayed and discontinuous features as well as non-planarity, they are also geometrically more complicated than a planar model fault. Degree of geometric fault complexity has long been linked to the manner in which tectonic strain is accommodated along a fault [*e. g.*, Allen, 1968]. The effects of fault discontinuities on the stress and displacement distributions in the neighborhood of a fault have been considered theoretically [Segall and Pollard, 1980] and discussed in more qualitative terms with regard to the spatial distribution of earthquake hypocenters [*e. g.*, Eaton *et al.*, 1970; Bakun *et al.*, 1980; Reasenberg and Ellsworth, 1982]. Also, details of recorded strong ground motions from earthquakes have been interpreted as showing evidence of the interaction of the dynamic earthquake rupture with mapped fault complication [*e. g..*, Aki, 1968; Lindh and Boore, 1981]. If geometric fault complexity is, indeed, important to an of understanding fault mechanics, then it would be useful to have a means of classifying or even quantifying complexity. If, at some level, the concepts of roughness and complexity are interchangeable, analysis of fault complexity could possibly lead to another means for attaching reasonable physical length scales to faulting processes and assigning suitable values to constitutive model parameters.

Fault surfaces will be treated as fractal sets. The fractal approach to quantifying fault complexity is suggested by considering two different types of observations of fault geometry and earthquake occurrence. Tchalenko [1970] examined the structures of shear deformation zones ranging in size from shear box experiments to earthquakes. He observed that, over a wide range in length scales, from tens of millimeters to hundreds of meters, the formation and evolution of these shear zones involved identical characteristic stages which correlated with characteristic features on force-vs-displacement diagrams. Therefore, from a structural point of view, shear deformation zones are similar over the range of sizes he considered. The other relevant observation is that there is a rather simple empirical representation of the distribution of earthquakes over the observed range of magnitudes. A single parameter, the earthquake b-value, characterizes this distribution. It has been shown [Andrews, 1980; Aki, 1981] that b-value can be directly obtained from an assumption of earthquake self-similarity, that is, that earthquake size or magnitude is a function of only fault length. Considering both the structural similarities of faults and the scaling of earthquakes, then, it may be useful to treat the complexity of fault geometry in such a way as to allow it to persist to all scales. One such approach is that of fractals, developed by Mandelbrot [1977] to characterize sets which exhibit irregularity regardless of the scale at which the set is being examined.

Central to the development of the idea of fractals are the notions of dimension and that, for a given set, a number of different dimensions can be defined which need not all be coincident. Two of the different definitions of dimension, namely, topological dimension and fractal or Hausdorff-Besicovitch dimension, must be considered in order to identify a set as being a fractal set. From Mandelbrot [1977, p. 15], "A fractal set will be defined as a set for which the Hausdorff-Besicovitch dimension strictly exceeds the topological dimension." Topological dimension is the more commonly encountered definition of dimension and it simply refers to the number of coordinates associated with elements in the set. Fractal

dimension is a measure of a set's complexity or irregularity. It can be determined in a number of ways, and, once the fractal dimension of a set has been determined, it provides a means of quantitatively characterizing the fractal nature of that set.

The notion of fractal dimension is perhaps most effectively introduced by means of an example. The example chosen by Mandelbrot [1977] is that of the length of the coastline of Britain. Mandelbrot [1977] presents the data from an experiment conducted by Richardson who estimated the lengths of coastlines, national boundaries and simple curves using a chain of line segments of equal length **r**. Rather than converge to an estimate of what might be expected to represent the true lengths of the coastlines, as the measuring length or yardstick length **r** is assigned smaller and smaller values, it is observed that the length of coastline L(**r**) tends to increase without limit. Plotted on log-log axes, the empirical relationship between L(**r**) and **r** is represented by a straight line:

$$\log_{10} L(\mathbf{r}) = a + b \log_{10}(\mathbf{r}) . \qquad (5.2)$$

A further interpretation of this result is that, in order to approximate a coastline by a number of line segments of length **r**, two constants must be specified. To achieve a total length L(**r**) from segments of length **r** requires a total number $A\mathbf{r}^{-D}$ of such segments, so that

$$L(\mathbf{r}) = A\, \mathbf{r}^{1-D} . \qquad (5.3)$$

Comparing (5.2) and (5.3), it follows that : a = log A and b = 1 - D . It also follows that L(**r**) increases more rapidly for larger D so that larger values of D can also be directly associated with more complicated curves or coastlines.

It was suggested by Mandelbrot that D which appears in the exponent in equation (5.3) can be thought of as a dimension following the approach of Hausdorff and leading to

the definition of Hausdorff, or fractal, dimension. The linear measure of a polygon, its perimeter, is obtained by adding the lengths of its sides, raised to the power d = 1. The surface measure of the same polygon is obtained by first paving or tiling with squares and then adding up the areas of these squares, i. e., by summing the lengths raised to the power d = 2. If the coastline is approximated by means of polygons with sides of length **r**, then Richardson's result states that the total number of polygons N is $N = A\,\mathbf{r}^{-D}$. A measure μ of the set defined by the coastline in the dimension d is given by:

$$\begin{aligned} \mu &= N\,\mathbf{r}^{d} \\ &= A\,\mathbf{r}^{-D}\,\mathbf{r}^{d}. \end{aligned} \qquad (5.4)$$

It is important to note that the measure μ in the dimension d is independent of segment length **r** and dimension d for the Euclidean case when d = D. For d less than D, the measure μ increases with decreasing **r**. Similarly, for d greater than D, μ tends to 0 as **r** decreases. In the case of a coastline, d = 1 and D > 1 so that, as the sensitivity of the measurement increases by decreasing the yardstick length **r**, the measure (length) of the coastline increases.

This increase in coastline length with decreasing yardstick length results from the ability to follow details of the coastal features with finer length measures. The fractal dimension thus obtained is a measure of the irregularity of the coastline over the range of scales included in the set of measurements. The idea of a coastline can be further developed by including off-shore islands in the coastline length determinations. With sufficiently fine resolution, the irregularity of the island coastlines can be measured such that the islands can be considered as mini-continents. Clearly, however, with too small a yardstick length rendering each island a continent in its own right, the relationship of the off-shore islands to the continent is lost. That the presence of the islands reflects the fragmented nature of the

continental coastline is demonstrated by measurements over a range of yardstick lengths which not only resolves the irregularity of the individual island coastlines but also spans the distances by which the islands find themselves separated from their continent. With such a range, the islands are lost as parts of the continental coastline at long yardstick lengths. They become more and more prominent as the yardstick length decreases. The fractal dimension determined with this set of yardsticks is a measure of the fragmentation as well as the irregularity of the coastline. In terms of the fractal dimension, it is not necessary to distinguish between topologically different sets represented by coastlines of continents, *i. e.* irregular but continuous, and coastlines of continents and islands, *i. e.* unconnected or fragmented and irregular [Mandelbrot, 1977, p. 70].

Fault trace complexity measured by fractal dimension is also a combination of fault irregularity and fault fragmentation. If faults are considered as continents and/or islands with zero width, the same approach may be followed to estimate fault fractal dimension. Segall and Pollard [1980] have analysed the mechanics of fragmented, *en echelon* fault segments for which the important parameters are fault segment length and inter-segment spacings both along strike and off of strike. For this type of fault model, the individual elements are simple, nonfractal segments and the complexity which arises is strictly a product of the fragmentation introduced by inter-segment spacings. As with off-shore islands, the apparent length of fault trace increases if the set of measuring lengths ranges from greater than to less than the fault spacings.

5.4 Fractal Geometry in the San Andreas Fault Zone

5.4.1 Measuring Method

Recalling that one definition of fractal dimension is derived from a collection of length estimates, fractal dimension of fault traces can be determined in a manner identical to

that which was used by Richardson and Mandelbrot to fix the fractal dimensions of coastlines. Estimates of lengths of mapped fault traces are made according to a method described by Mandelbrot [1977] which he identifies with determining the covering dimension of a set. Circles of a chosen radius **r** are drawn in order to cover the fault trace using a minimum number N(**r**) of such circles. Fault length is a function of radius **r** and it is defined as the total area of the N circles, divided by the diameter of a single circle. That is,

$$L(\mathbf{r}) = \frac{N(\mathbf{r})\,\pi\,\mathbf{r}^2}{2\mathbf{r}} \,. \qquad (5.5)$$

L is further normalized by a factor of $\pi/4$ so that the fault length estimates are given by:

$$L^{\circ}(\mathbf{r}) = 2\,N(\mathbf{r})\,\mathbf{r}. \qquad (5.6)$$

Lengths $L^{\circ}(\mathbf{r})$ are plotted as a function of measuring radius **r** on log-log axes. The fractal dimension D is estimated from the "D-slope," that is, the slope b of straight-line fits to the log-log plots, as:

$$D = 1 - b\,. \qquad (5.7)$$

D is thus a measure of the rate of change of log(fault length) with respect to log(resolution of length measurement).

This method is illustrated with the simple example shown in Figure 5.7. In this figure, two parallel fault segments of equal length **a** are separated in the x- and y-directions by spacings **g** and **h**, respectively. In this example,

$$\mathbf{a} = 4 \text{ cm}, \ \mathbf{g} = 2 \text{ cm}, \ \mathbf{h} = 1 \text{ cm} \ .$$

With a covering circle diameter of $2\mathbf{r} = 3.05$ cm, or a yardstick length of $\mathbf{r} = 1.52$ cm, these two segments can be covered by two circles; $L^{\circ}(\mathbf{r}) = 6.10$ cm. Five circles of diameter 1.35 cm are required to cover these same segments. The measured length increases to $L^{\circ}(\mathbf{r}) = 6.75$ cm . Finally, when the circle diameter is reduced to less than the spacing **h** between the line segments, we begin to measure the lengths of the segments separately. With $\mathbf{r} = 0.35$ cm, the length increases even further to $L^{\circ}(\mathbf{r}) = 8.40$ cm . In this example, for $2\mathbf{r} < \mathbf{h}$ the measured segment lengths will tend toward $L^{\circ}(\mathbf{r}) = 8$ cm as **r** decreases. If non-uniform segment lengths and segment spacings are introduced, the length measurements will vary over a wider range of **r** which is determined by the total extent of segments and the distributions of **a**, **g**, and **h** for the segment population.

5.4.2 Fault Trace Data

The data for this exercise are taken from maps in the United States Geological Survey "strip map" series showing the most recently active fault breaks along the San Andreas fault in central and southern California mapped to scales of 1: 62,500 [Brown, 1970] and 1: 24,000 [Ross, 1969; Vedder and Wallace, 1970]. The strip maps display the fault trace centered within a band about 4-km-wide. These maps, together, will be used to study the fault geometry between Bitterwater in the northwest to Lake Hughes in the southeast, including parts of the fault which are believed to have ruptured during the great 1857 Fort Tejon earthquake and during the M_L 1966 Parkfield earthquake.

A study of fault geometry such as this one which uses compilations of field data relies heavily on the degree to which the observed geomorphologic and topographic expressions of fault movement can be accurately interpreted in terms of the locations of fault traces. Surface features like fault scarps, sag ponds, stream offsets and ridges which are

used to infer fault locations and amounts of fault offset are subjected to erosion and weathering. Through time, the unambiguous identification of these features is progressively more difficult. The task of tracing the fault location over a large region is further complicated by variations in the amounts of rainfall and resultant erosion of surface features which occur in different areas. For example, signs of fault offset are well-preserved in dry regions like the Mojave Desert and the Carrizo Plain along the 1857 break, but they are more likely to be obscured or erased in areas like the Coast Range where more rain falls.

By making inferences about the complexity of fault trace geometry and its possible relation to the mechanical behavior of faults, it is clearly necessary to rely on the assumption that the surface expressions of faulting do reflect deeper fault structure. It is possible that the mapped fault complexity is strictly an effect of the properties of materials which constitute the uppermost crust and that fault surfaces are smoother at depth. On the other hand, seismicity studies like the ones mentioned above suggest that complex fault structure does, indeed, extend to depths of the order of 12 to 15 km [*e. g.*, Eaton *et al.*, 1970]. That the fault complexity actually increases rather than decreases with depth in regions of thrust faulting has also been suggested by King and Yielding [1983] who note that aftershocks of the 1980 El Asnam, Algeria earthquake are not located along clearly defined fault planes. From the full range of possibilities, the premise adopted here is that the mapped fault detail is representative of the structural detail of the fault surface at depth, without requiring that the same detail be exactly projected down. Finally, although only fault trace geometry is discussed here, measurements of fault trace complexity may be suggestive of fault surface complexity if a method referred to as "slit island analysis" [Mandelbrot *et al.*, 1984] proves to be applicable to fault topography. If fault trace complexity can be extended to fault surface complexity in this way, $D_{surface} = D_{trace} + 1$.

Earlier discussions of fractals in connection with fault behavior, e. g., Andrews [1980], Aki [1981] and King [1984], have begun with the notion that the fractal sets that the

fault make up are self-similar, or that the same complexity of fault structure observed at one scale is observed at any other scale, as well. Self-similarity implies that, when examined over any length scale, the same fractal dimension is produced. The assumption of the scale-invariance of earthquakes has also been made in order to apply the theory of renormalization groups to fault mechanics [Smalley *et al.*, 1985] and has long been justified on the basis of magnitude-frequency relationships. Moreover, the actual determination of fractal dimension of these sets is simplified by introducing the similarity dimension which, for the case of self-similarity, is identical to fractal dimension. It is this equivalence of similarity dimension to fractal dimension which was used by Aki [1981] when he determined fractal dimension of faults from the empirical magnitude-frequency and magnitude-moment relations and, also, by King [1984] in his geometrical explanation of b-value. Because the underlying premise here is that the San Andreas fault displays varying degree of complexity from region to region, the assumption of self-similarity will not be used. Therefore, it should be understood that the discussion of fractal dimension which follows relates to fault trace geometry as it is mapped to a specific scale.

What results from the selection of a specific scale is a set of effective dimensions which characterize the fractal over lengths which lie betwen upper and lower bounds or fractal cutoffs, selected, in principle, on the basis of specific physical processes being considered. In constructing the magnitude-frequency relation for earthquakes from a self-similar model, Andrews [1980] restricted his discussion to fault lengths which range between the grain sizes of fault zone materials at short wavelengths and the depth in the lithosphere to which seismic activity persists at long wavelengths. Following the approach of Andrews [1980], an upper bound or outer cutoff of 15 km is chosen initially, associated with the thickness of the seismogenic crust in California. As stated earlier, the measurement resolution or range of yardstick lengths that can be considered in a map-based study of fault geometry is restricted, in practice, by the scale of the mapping. With these strip maps,

details down to 50 m can be resolved. This length is the lower bound or cutoff imposed by the map scales.

Three subsets of the San Andreas fault are defined and their general locations are sketched in Figure 5.8 . Subset P extends from Bitterwater to Cholame, where fault creep and small-to-moderate earthquakes are observed. The 1966 Parkfield earthquake ruptured the southernmost 20 to 30 km of this subset. Subsets Q and R extend from Cholame into that part of the San Andreas fault which has remained locked since it ruptured during the 1857 Fort Tejon earthquake. It was noted by Vedder and Wallace [1970] and, later, by Sieh [1978], that in the southern end of the Carrizo Plain, the appearance of the fault break changes from well-defined straight traces through the Carrizo Plain to shorter, more complicated sets of traces secondary to the San Andreas, particularly in the Elkhorn thrust or Elkhorn Hills region. The boundary between Q and R was placed near the occurrence of this transition, about 24 km NW of Camp Dix. R extends from there, through the Big Bend region where the San Andreas is intersected by the Garlock and Big Pine faults, to 8 km NW of Lake Hughes.

5.5 Fault Length Measurements and Fractal Dimension

Using the method illustrated in Figure 5.7 , a series of fault length estimates are made in the subsets defined above. The measurements were begun with the smallest radii and continued with progressively larger radii. This data is presented in Table 5.1 and plotted in Figure 5.9. In Table 5.2, it is seen that as $\mathbf{r}$ increases, the estimates of $L^*(\mathbf{r})$ tend to a constant value, in all cases before $\mathbf{r}$ reaches 8 km . When this is observed, the measurements were stopped and it is assumed that "the" fault length in a nonfractal sense would be approximated by these values.

Before attempting to fit a least squares best-fit straight line to the data, it should first be noted that the same fractal behavior as in the coastline example is exhibited. Measured

fault length of a fault break within a subset increases with decreasing yardstick length. However, more importantly, this increase of measured fault length does not occur uniformly over the entire range of yardstick lengths. Rather, it is observed only over the short wavelengths but, beyond a certain measuring radius, the fault length estimates seem to level off at approximately constant values. Assuming fault self-similarity and imposing a single straight-line fit to each of these collections of data points would mask this effect.

The values of $\mathbf{r} = \mathbf{r}_c$ where changes in the length-vs-yardstick relation occur can be roughly estimated from the graphs. For subset P, the data between 80 m and 350 m show a trend for decreasing L° with increasing **r**, but beyond about 500 or 600 m, this trend is no longer seen. In terms of fractal dimension D, the slopes imply D values for the San Andreas fault, mapped at 1: 62,500 between Bitterwater and Cholame, such that :

$$D \approx 1.1, \text{ for } 80 \text{ m} < \mathbf{r} < 500 \text{ m, and}$$

$$D \approx 1.0, \text{ for } \mathbf{r} > 500 \text{ m.}$$

Similarly, for the fault break in subset Q mapped at 1: 24,000 between Cholame and the Elkhorn region, $D \approx 1.2$ for 50 m $< \mathbf{r} <$ 350-400 m, and $D \approx 1.0$ for $\mathbf{r} >$ 400 m. Finally, in subset R from the Elkhorn thrust to Lake Hughes, also mapped at 1: 24,000, $D \approx 1.2$ for 50 m $< \mathbf{r} <$ 1 km and $D \approx 1.0$ for $\mathbf{r} >$ 1 km .

5.6 Discussion and Conclusions

The observed tendency for the fault length estimates to increase with increasing measurement resolution - or decreasing yardstick length - supports the notion that faults can be considered as fractal sets and that fault trace geometry, much like the geometry of a coastline, is an example of fractal geometry. It is also noted that in these examples

considered here, the fractal geometry is not uniformly expressed along the fault nor over the entire range of measurements. In other words, the set of mapped fault traces is not a self-similar set, being neither translational- nor scale-invariant. Thus, there is the suggestion which follows from this observation that for faults, as it probably is for the majority of natural fractal sets, different fractal dimensions apply at different locations and at different levels of measurement resolution. To assess the fractal character of a fault system, it is necessary to define both the fractal dimension D and the fractal cutoffs which bound the range of scales over which a given D applies.

Interpreting fractal dimension as a measure of fault complexity and fragmentation, the results from the strip map measurements indicate that fault complexity changes at wavelengths $\mathbf{r}_c$ where $\mathbf{r}_c$ represents the values of $\mathbf{r}$ where the slopes of the log L^*-vs-log $\mathbf{r}$ plots in Figure 5.9 change. Of course, it is necessary to establish that $\mathbf{r}_c$ does not arise as a result of the mapping or measuring procedures. Because a fault, even at the scale 1: 24,000 , is still a nearly linear feature, the longer that the fault subset that is being measured is, the less obvious is the expression of the fractal property. This is especially the case if fault complexity is concentrated in specific locations, as these observations suggest for the San Andreas, instead of being uniformly distributed along the fault. In this study, this effect is hopefully diminished by defining fault subsets of approximately equal lengths.

The values of $\mathbf{r}_c$ estimated graphically from Figure 5.9 are: $\mathbf{r}_c \approx 500$ m in P, $\approx$ 300-400 m in Q, and ≈ 1 km in R . Direct comparisons of the subset P value to the others is complicated by the fact that the strip map in P is drawn at 1: 62,500 while in Q and R it is drawn at 1: 24,000 . Because a coarser map would eliminate some of the fault detail, just the difference in map scales might account for the lower D value for $\mathbf{r} < \mathbf{r}_c$ in subset P. The intersections of the $D > 1$ line segment with the flat segment in Figure 5.9 which are used to estimate $\mathbf{r}_c$ are more clearly defined, the greater the difference between D-slope and 0. Thus, it may be difficult to distinguish between $\mathbf{r}_c$ values determined for P and Q. The difference

between P and R is perhaps still suggested by the data. Subsets Q and R, on the other hand, are both mapped at 1:24,000 and, through all of Q and much of R to Tejon Pass, and are both mapped by the same geologists. The southern end of Q and the adjacent northern end of R mapped by Vedder and Wallace [1970] are shown in Figure 5.10 . The fault trace in Q is indeed rather simple. In R, more fault branching and segmentation are mapped. It is the presence of these branched features, spread farther from the fault in R than in Q, which leads to the larger $\mathbf{r}_c$ seen in R. $\mathbf{r}_c$ is possibly identified with the fault zone width.

In terms of the mapped fault trace fractal geometry, then, $\mathbf{r}_c$ is a critical length. At wavelengths greater than $\mathbf{r}_c$, D is nearly 1.0 so that the fault traces are relatively simple, non-fractal sets. Below $\mathbf{r}_c$, the fault fragmentation is more apparent and the fractal property of fault trace geometry is exhibited.

Aki [1979] proposed a fracture mechanics interpretation of seismic source parameters in order to make quantitative estimates of the properties of barriers on a fault plane. He used instrumental data from the 1966 Parkfield earthquake and geologic data relevant to the rupture during the great 1857 Fort Tejon earthquake and postulated a cohesive zone fault model to characterize the properties of the barriers. He found that the size of the cohesive end zone associated with the Parkfield earthquake is ~ 340 - 700 m . In order to determine the force-vs-displacement parameters for the fault cohesive zone associated with the 1857 earthquake, he assumed that the ratio of endzone size to crack length determined for Parkfield is applicable to the 1857 earthquake, so that the cohesive zone in this case is ~ 1 - 2 km [Aki, 1979].

Strong motion seismograms were interpreted in terms of a fault barrier model by Papageorgiou and Aki [1983 a and b]. In their model, they assume that the strong motion power spectrum is cutoff at frequencies above an f_{max} which is controlled by the size of the cohesive endzone on the fault,

$$f_{max} = \frac{v}{d} , \qquad (5.8)$$

where v is the rupture velocity and d is endzone size. Their estimates in terms of the barrier parameters for several other California earthquakes are consistent with Aki's estimates [Papageorgiou and Aki, 1983b], with the larger earthquakes in their data set having larger cohesive zones than the moderate events. Cohesive endzone size in the laboratory experiments corresponds to characteristic frequencies for stick-slip spectra. A characteristic frequency in the seismic spectrum related to endzone size, as assumed by Papageorgiou and Aki, would be expected if the endzone effect is not obscured by spectral properties of propagation path or near-station structure.

It is interesting to note that the cohesive zone dimensions roughly correspond to the critical lengths in the fractal characterization of fault geometry. That is, cohesive zone length associated with the Parkfield earthquake and critical radius r_c in the corresponding subset P are both about 500 m ; similarly, the 1857 cohesive zone and the critical radius for the combined subsets Q and R, where the fault has not slipped since 1857, are both about 1 km. Without knowing how the fault trace geometry was produced to establish the critical geometric length, the correspondence between the cohesive zone size and the fault zone width is but a coincidence. However, it would be intuitively appealing to be able, at some point, to identify the critical geometric length with a physically motivated critical length. If fault zone width were representative of the size of the cohesive zone, then it would be expected that large d_c values are required to model cyclic fault behavior [Mavko, 1983; Tse, 1985] or strong ground motions [Day, 1982].

Table 5.1 . Stick-slip Cohesive Zone Size: $\sigma = 3.45$ MPa.

position	v_c (km/s)	t_ω(s)	ω_c(cm)
988	0.89	6.86×10^{-4}	61
1278	1.45	2.29×10^{-4}	33
1532	1.69	1.63×10^{-4}	27
1785	1.69	1.31×10^{-4}	22

Table 5.2 . Fault length measurements and critical fractal geometry length r_c for San Andreas subsets. P : Bitterwater to Cholame, including Parkfield segment, mapped at 1:62,500; Q: Cholame to 24 km NW of Camp Dix, mapped at 1:24,000 ; R: 24 km NW of Camp Dix to 8 km NW of Lake Hughes, mapped at 1:24,000 .

P			Q			R
r(km)			r(km)			
0.085	N	729	0.055	N	1089	1987
	L°(km)	123.9		L°(km)	119.8	218.6
0.144	N	414	0.095	N	560	--
	L°	119.2		L°	106.4	--
0.247	N	226	0.160	N	291	561
	L°	111.6		L°	93.12	179.5
0.322	N	170	0.280	N	155	285
	L°	109.5		L°	86.8	159.6
0.422	N	131	0.550	N	75	122
	L°	110.6		L°	82.5	134.2
0.555	N	98	1.00	N	41	61
	L°	108.8		L°	82.0	122.0
0.730	N	70	2.00	N	21	29
	L°	102.2		L°	84.0	116.0
1.25	N	41	4.00	N	11	15
	L°	102.5		L°	88.0	120.0
2.00	N	25	8.00	N	--	7
	L°	100.0		L°	--	112.0
4.00	N	13		r_c =	400 m	1 km
	L°	104.0				
8.00	N	7				
	L°	112.0				
	r_c =	500 m				

Figure captions.

Figure 5.1 . Cohesive zone crack model. Left side of figure is crack tip drawn in space with stress and displacement distributions shown. Right side shows hypothetical time histories of stress and displacement at a position on the crack surface.

Figure 5.2 . Time domain plots of stick slip events generated at 3.45 MPa normal stress on smooth (left) and rough (right) fault surfaces.

Figure 5.3 . (a) - (e) Smooth fault stick-slip spectra, with time series plotted at top, normalized to axis length.

Figure 5.4 . (a) - (d) Rough fault spectra, presented as in 5.3 .

Figure 5.5 . (a) - (e) Spectra of smooth fault records after initial decrease in shear stress. Presented as in 5.3 .

Figure 5.6 . Amplitude spectrum of hammer blow applied to test sample.

Figure 5.7 . Example showing measurement of fault lengths with covering circle technique.

Figure 5.8. Map, adapted from Jennings [1975] fault map of California, showing quaternary and younger faults. Subsets P, Q, and R are indicated.

Figure 5.9 . Fault length plotted as a function of measuring circle radius for subsets P, Q, and R.

Figure 5.10 . Mapped fault traces around the boundary between subsets Q and R, after Vedder and Wallace [1970], used in this study. Traces should be joined together at locations indicated by the capital letters. Sets of covering circles of radius $\mathbf{r} = 0.2$ km are drawn on each of the traces.

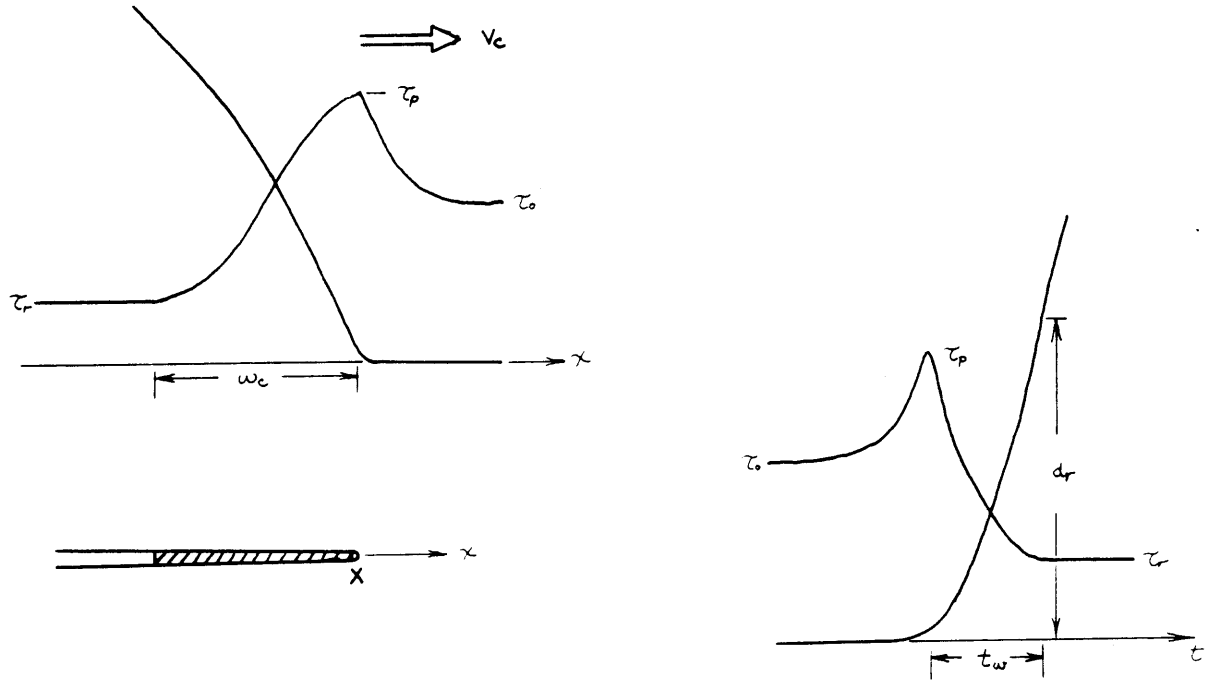

Figure 5.1

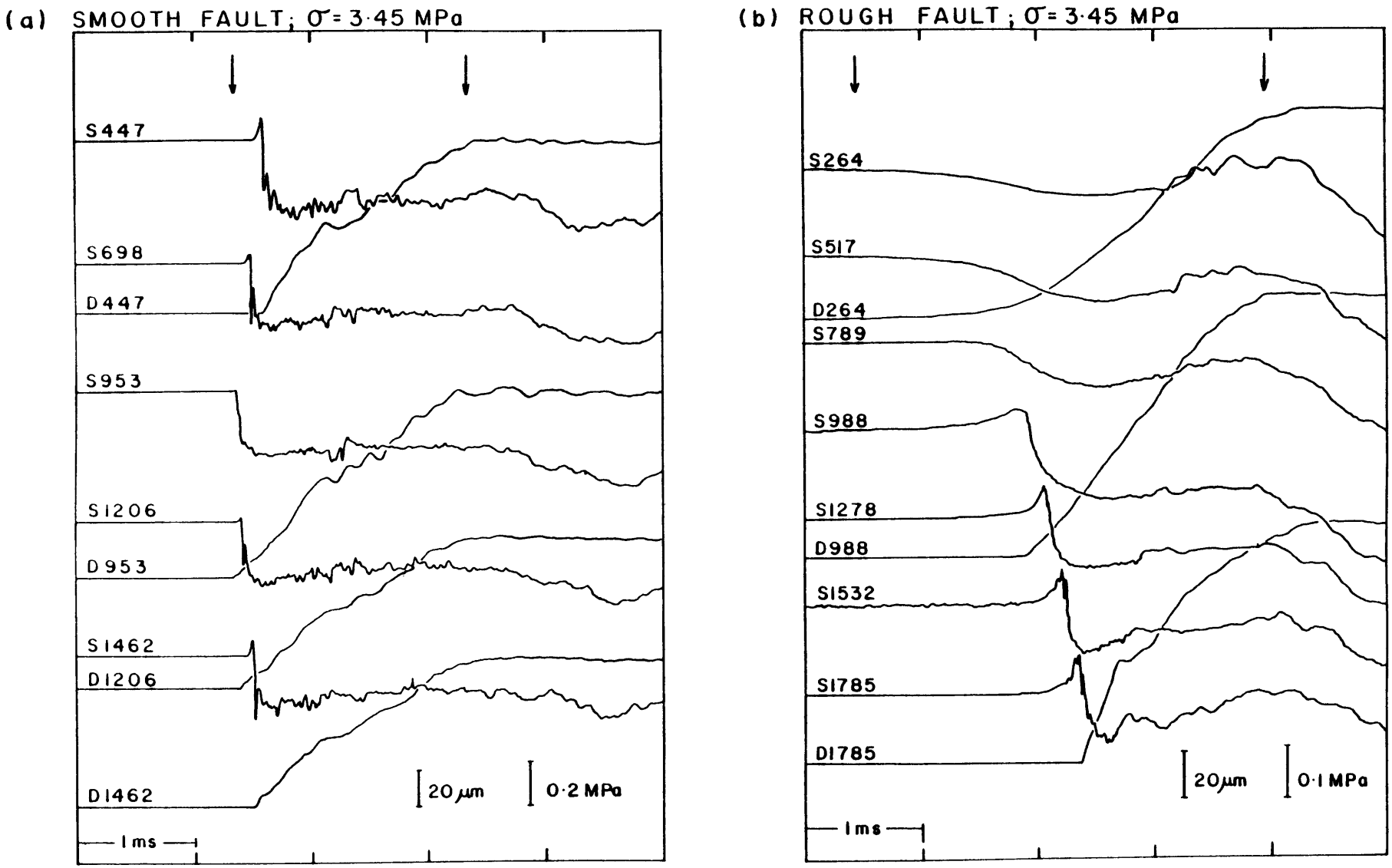
(a) SMOOTH FAULT; σ = 3·45 MPa
S447
S698
D447
S953
S1206
D953
S1462
D1206
D1462
20 μm
0·2 MPa
1 ms
(b) ROUGH FAULT; σ = 3·45 MPa
S264
S517
D264
S789
S988
S1278
D988
S1532
S1785
D1785
20 μm
0·1 MPa
1 ms

Figure 5.2

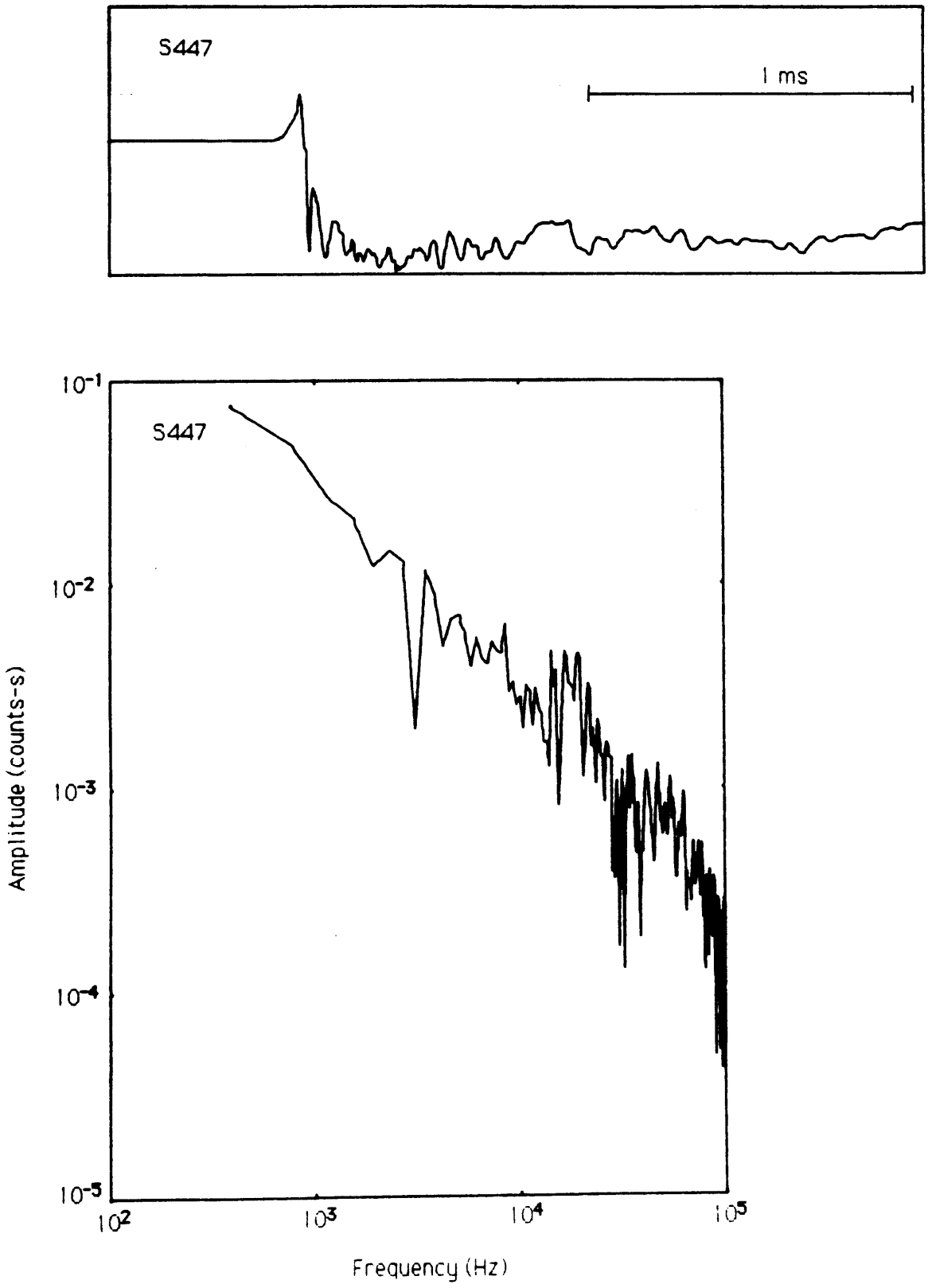
S447
1 ms
S447
10^{-1}
10^{-2}
10^{-3}
10^{-4}
10^{-5}
Amplitude (counts-s)
10^{2}
10^{3}
10^{4}
10^{5}
Frequency (Hz)

Figure 5.3a

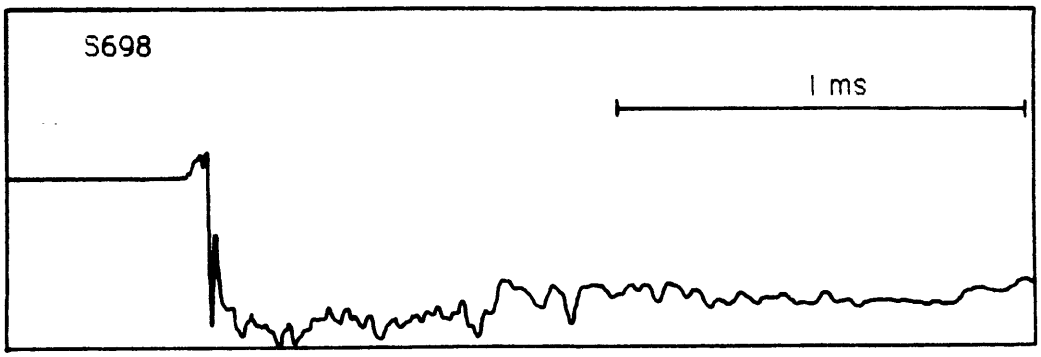
S698
1 ms

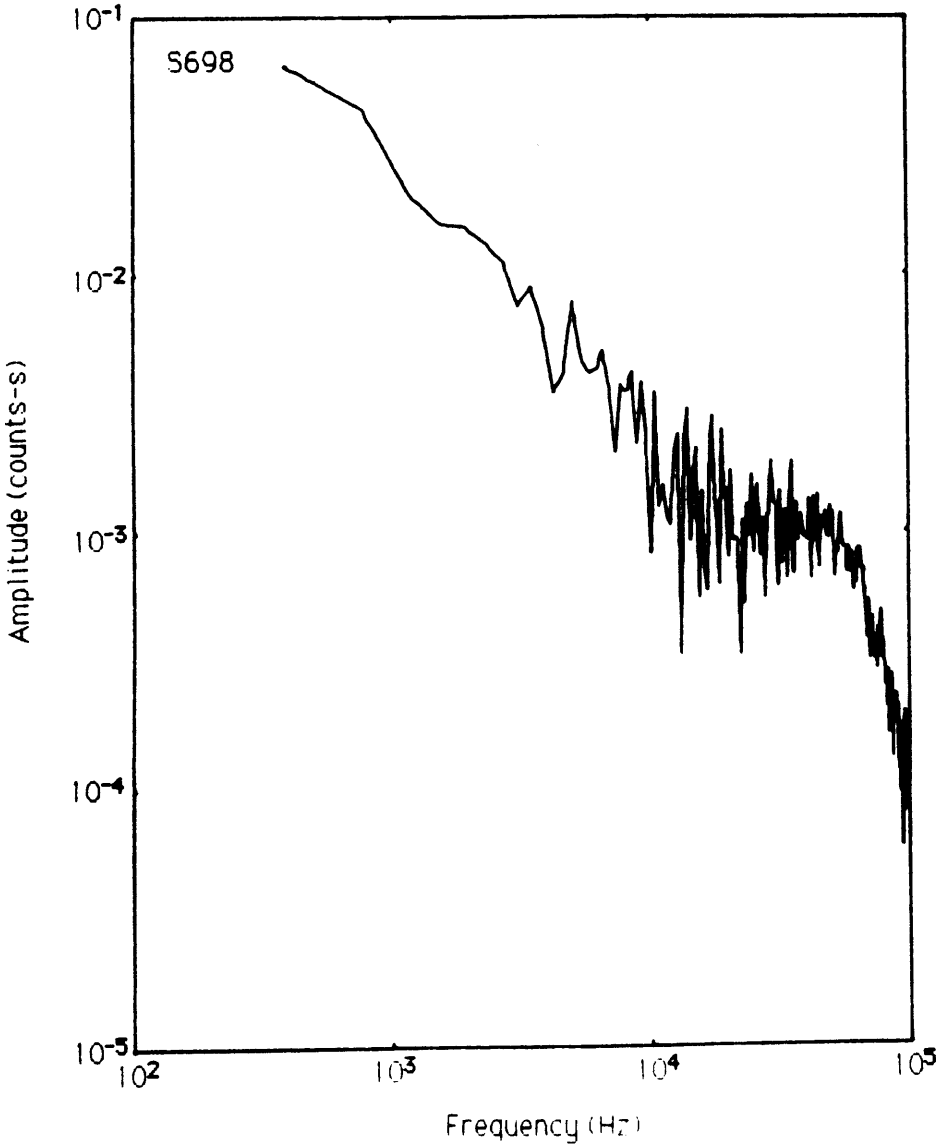
S698
10^{-1}
10^{-2}
10^{-3}
10^{-4}
10^{-5}
Amplitude (counts-s)
10^{2}
10^{3}
10^{4}
10^{5}
Frequency (Hz)

Figure 5.3b

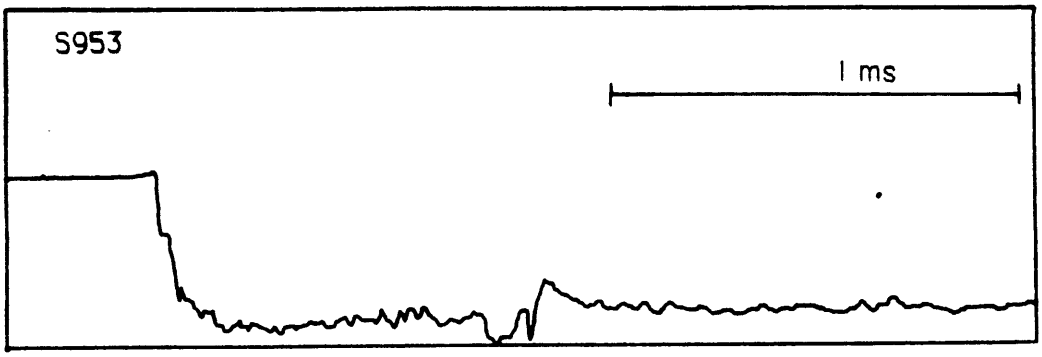
S953
1 ms

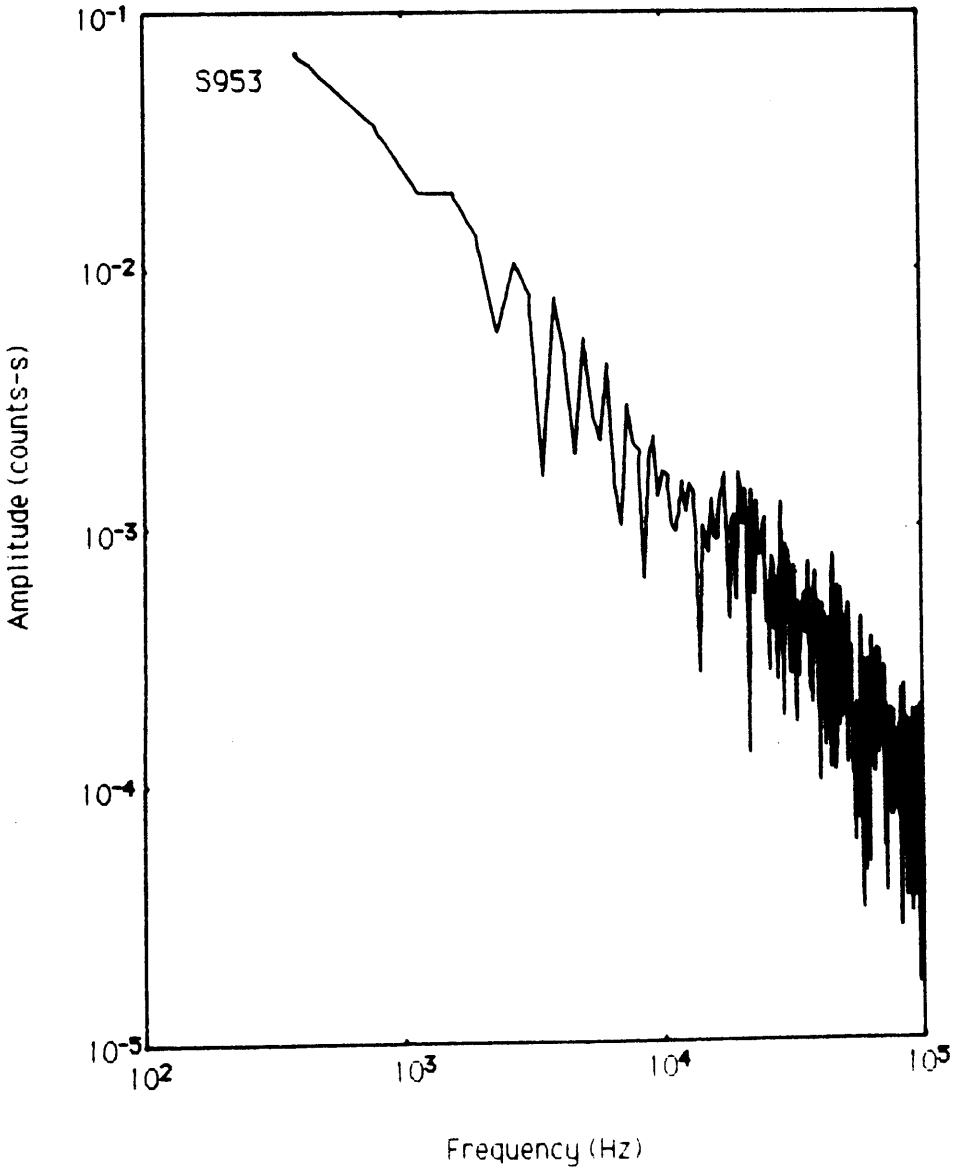
S953
10^{-1}
10^{-2}
10^{-3}
10^{-4}
10^{-5}
10^{2}
10^{3}
10^{4}
10^{5}
Amplitude (counts-s)
Frequency (Hz)

Figure 5.3c

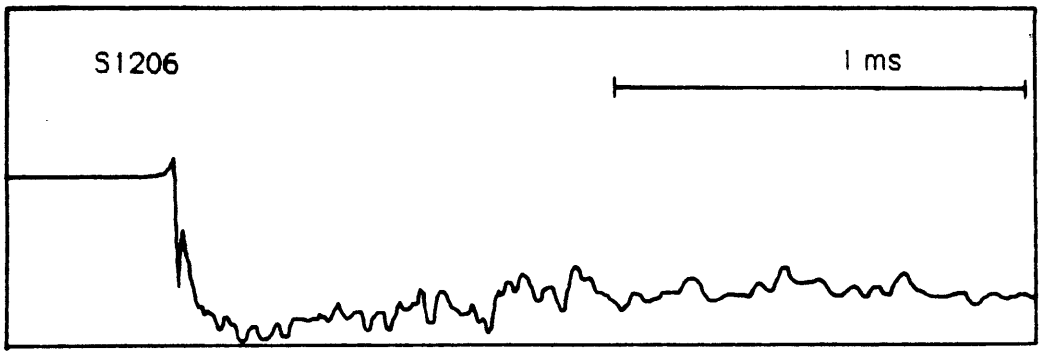
S1206
1 ms

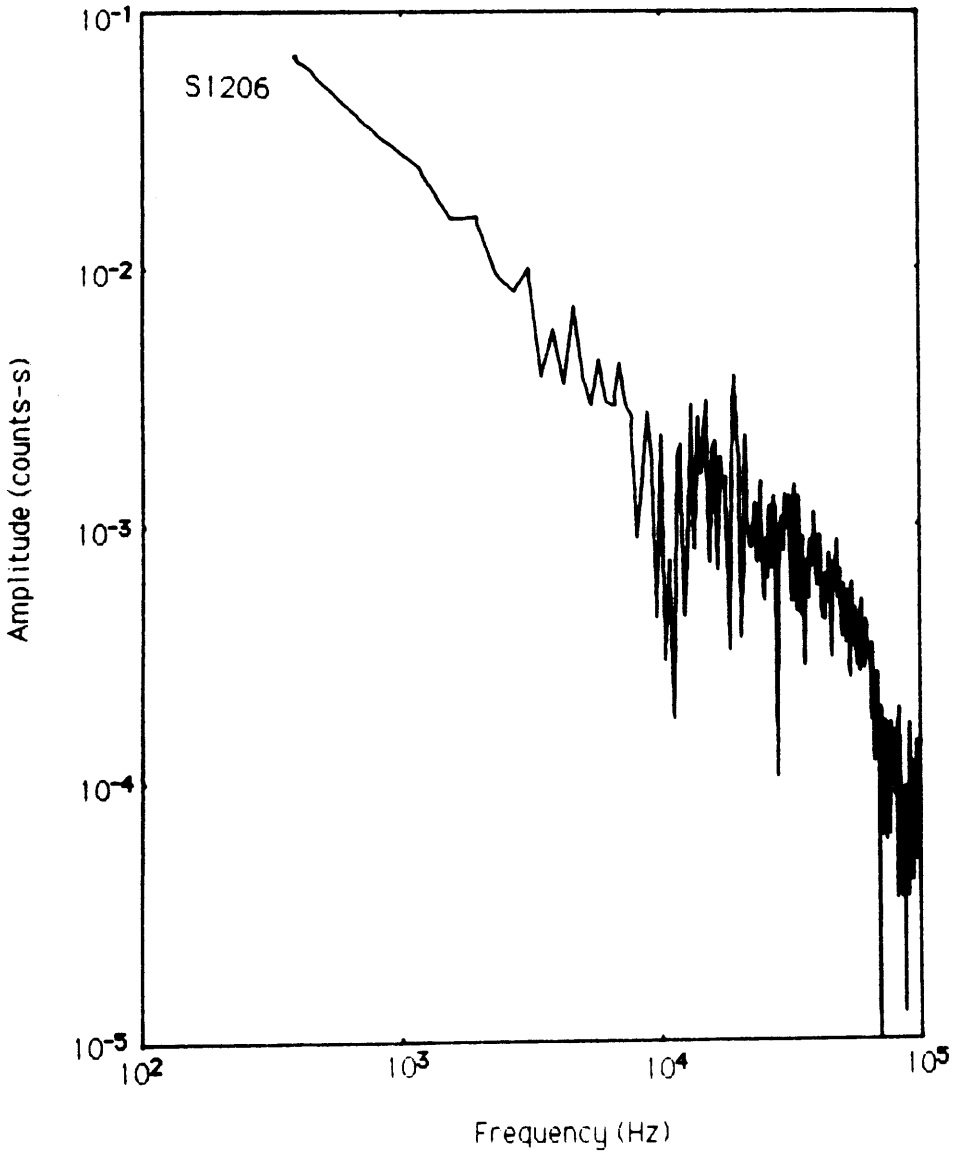
S1206
Amplitude (counts-s)
10-1
10-2
10-3
10-4
10-5
10²
10³
10⁴
10⁵
Frequency (Hz)

Figure 5.3d

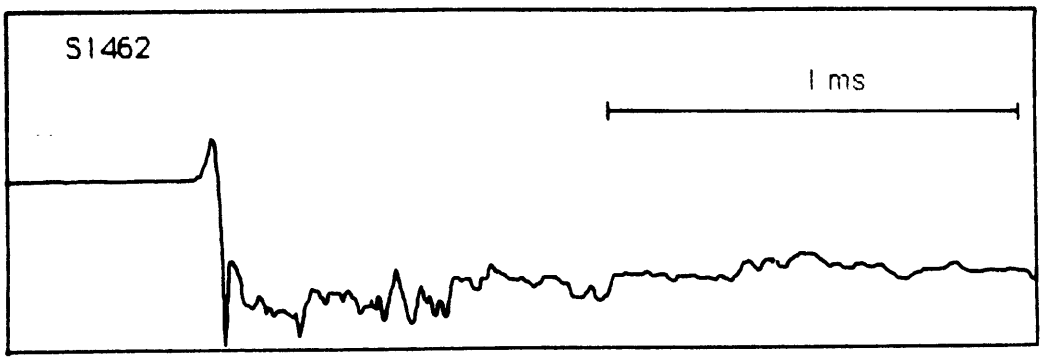
S1462
1 ms

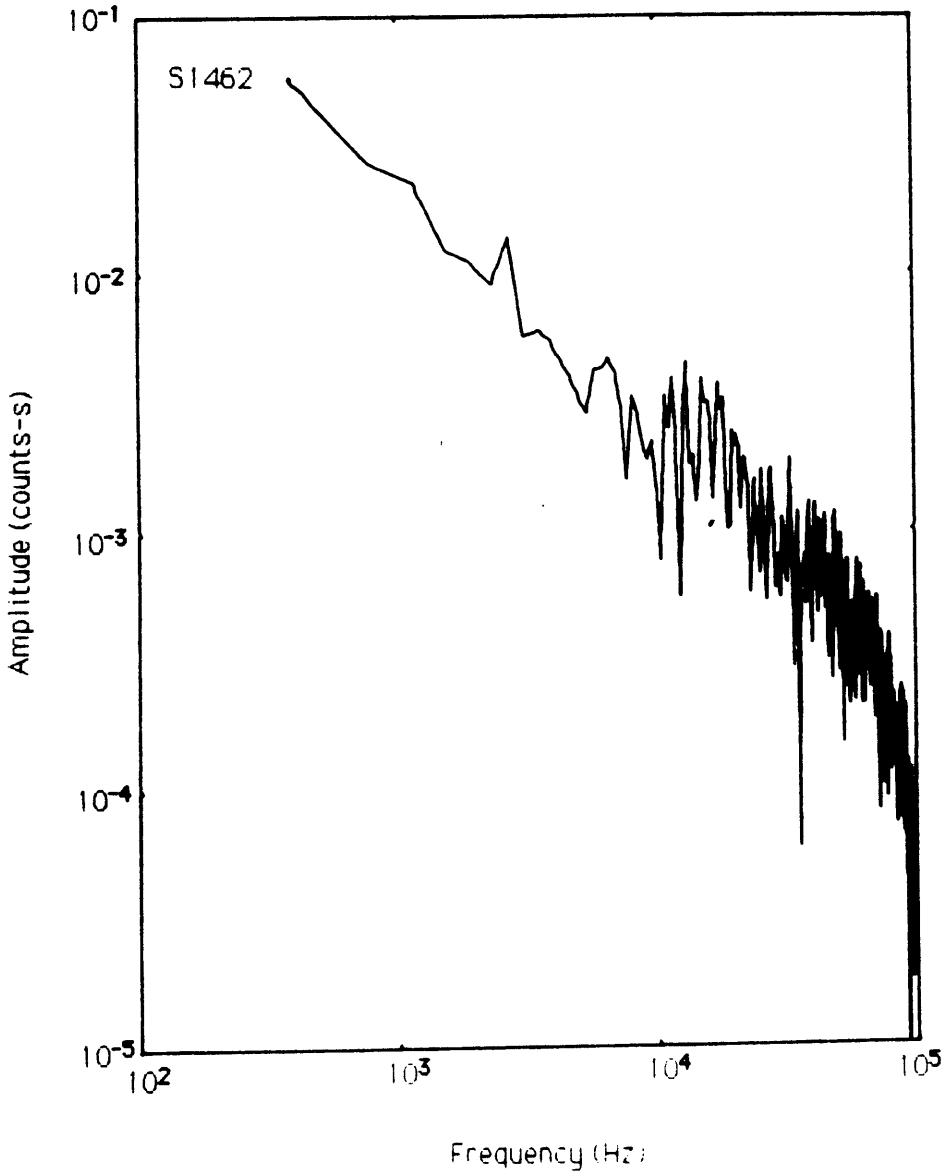
S1462
10^{-1}
10^{-2}
10^{-3}
10^{-4}
10^{-5}
Amplitude (counts-s)
10^{2}
10^{3}
10^{4}
10^{5}
Frequency (Hz)

Figure 5.3e

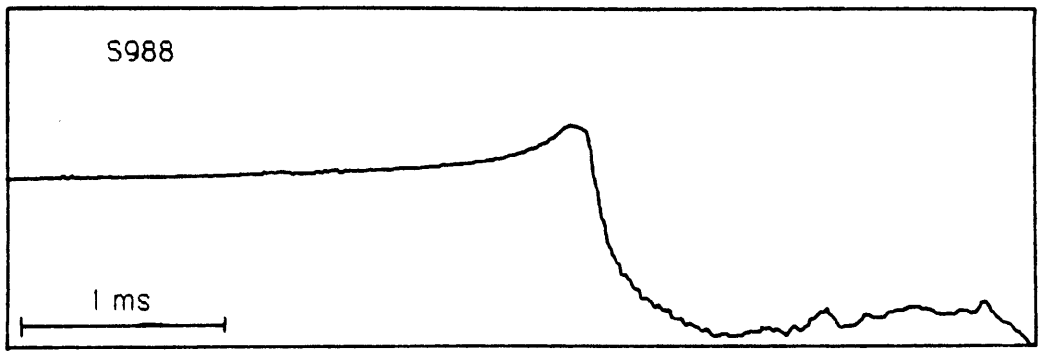
S988
1 ms

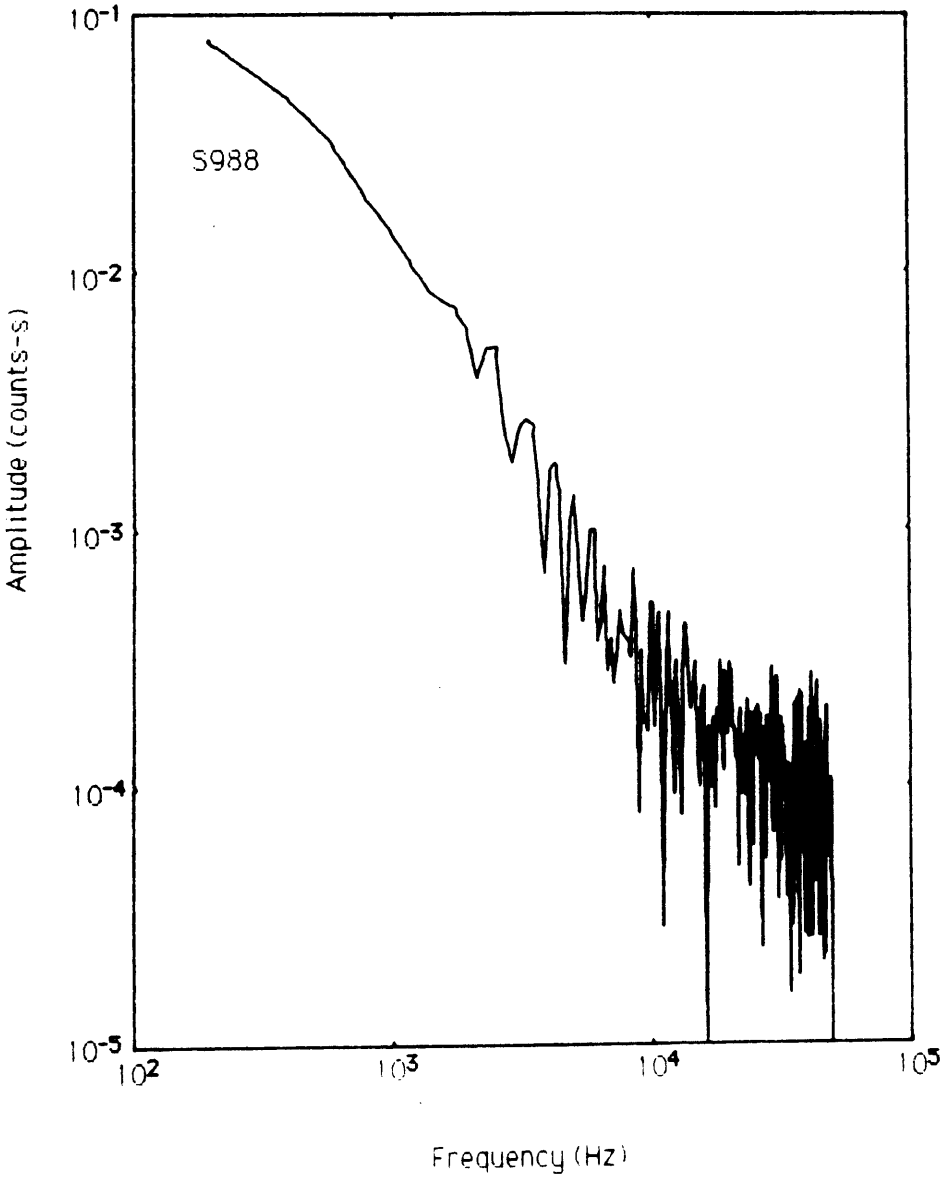
S988
Amplitude (counts-s)
10^{-1}
10^{-2}
10^{-3}
10^{-4}
10^{-5}
10^{2}
10^{3}
10^{4}
10^{5}
Frequency (Hz)

Figure 5.4a

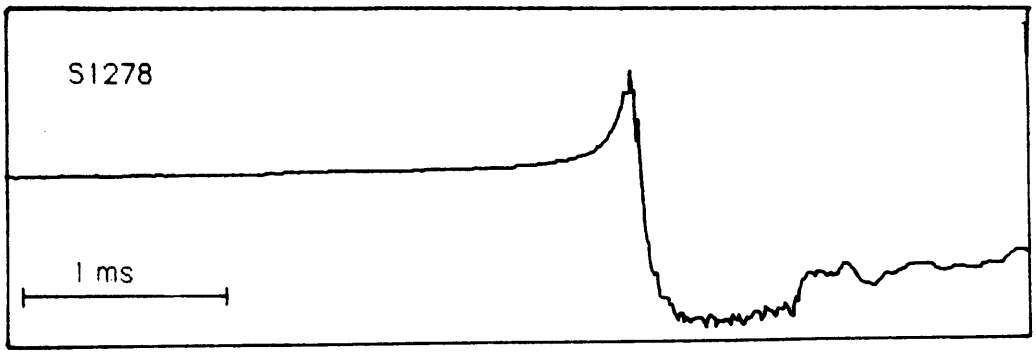
S1278
1 ms

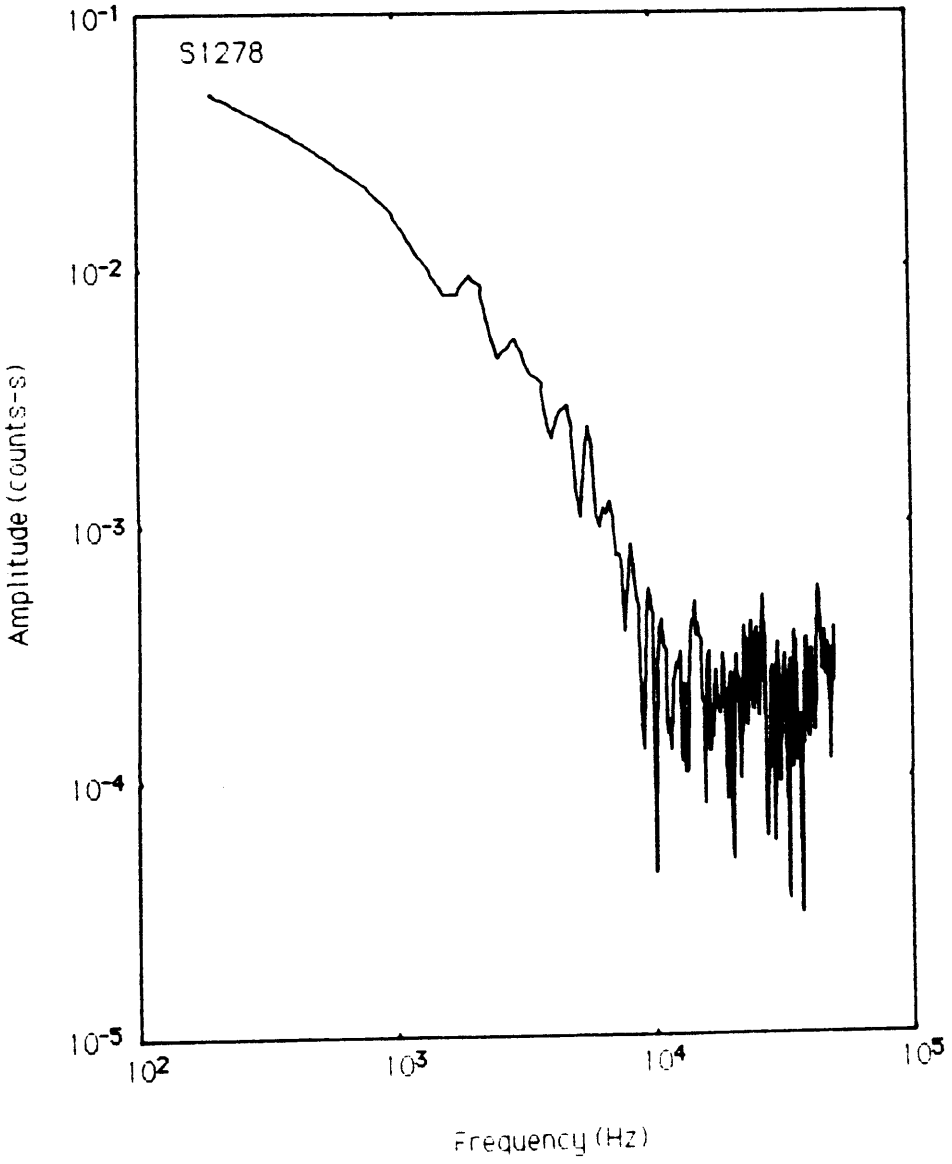
S1278
10^{-1}
10^{-2}
10^{-3}
10^{-4}
10^{-5}
Amplitude (counts-s)
10^{2}
10^{3}
10^{4}
10^{5}
Frequency (Hz)

Figure 5.4b

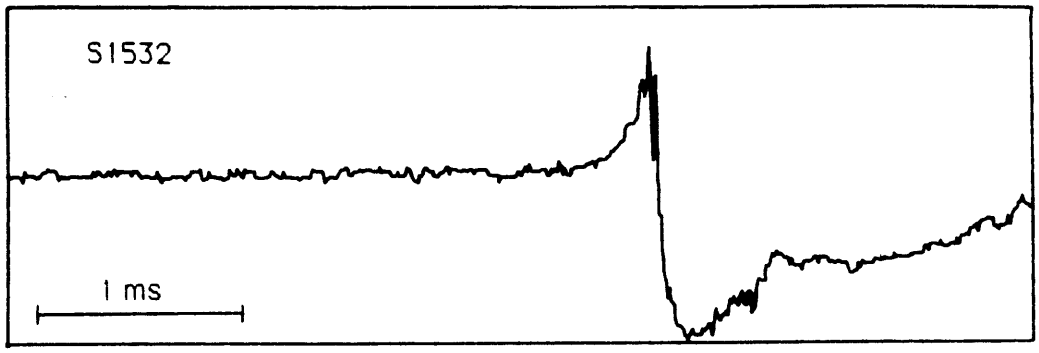
S1532
1 ms

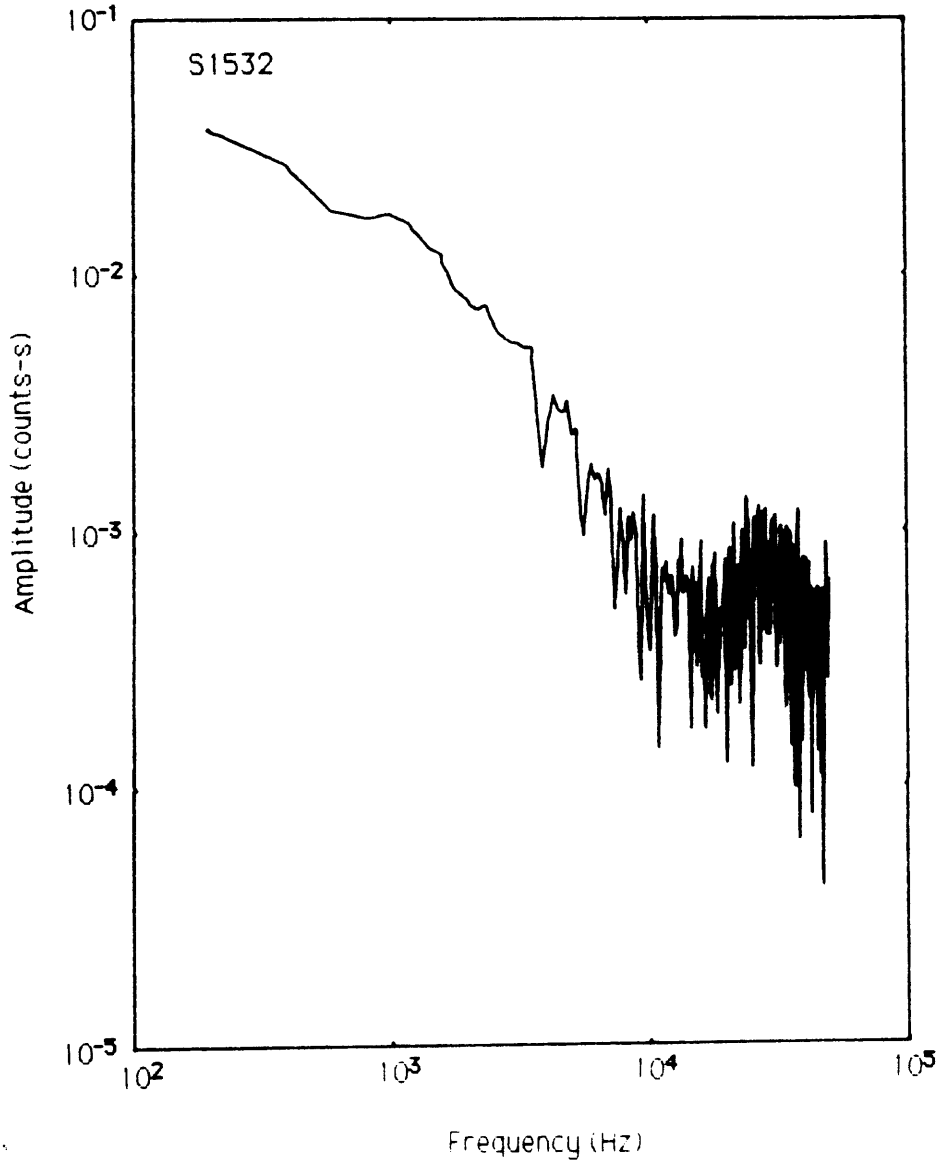
S1532
10^{-1}
10^{-2}
10^{-3}
10^{-4}
10^{-5}
Amplitude (counts-s)
10^{2}
10^{3}
10^{4}
10^{5}
Frequency (Hz)

Figure 5.4c

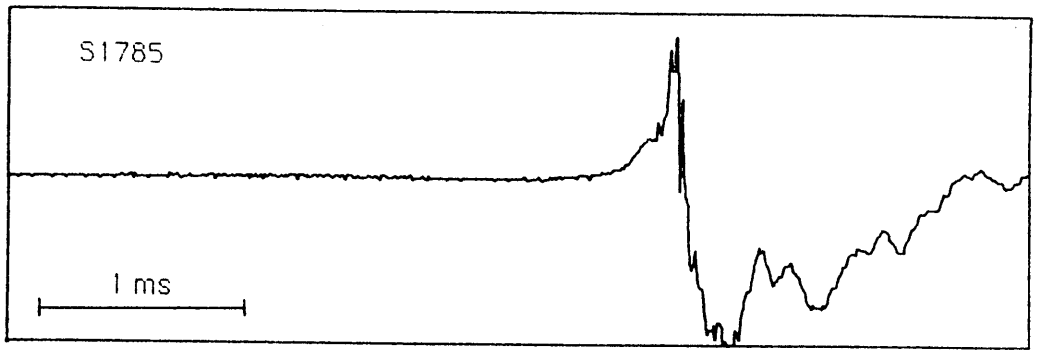
S1785
1 ms

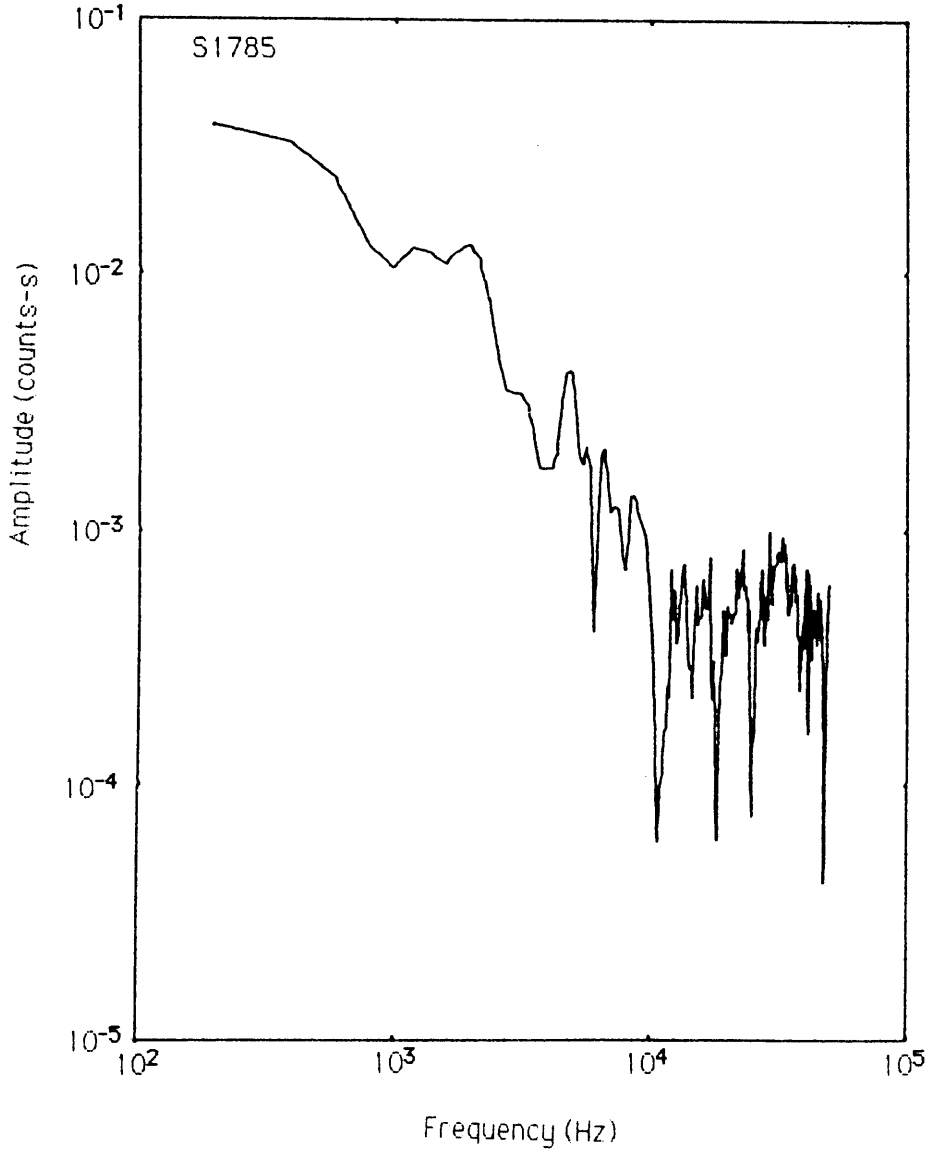
S1785
Amplitude (counts-s)
10-1
10-2
10-3
10-4
10-5
10²
10³
10⁴
10⁵
Frequency (Hz)

Figure 5.4d

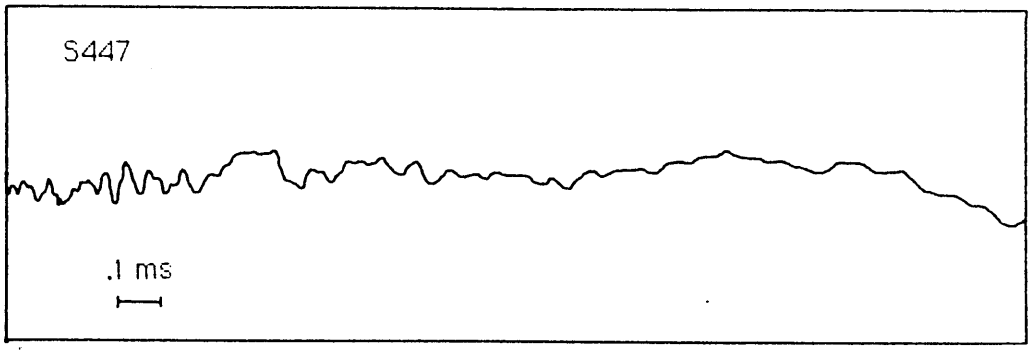
S447
.1 ms

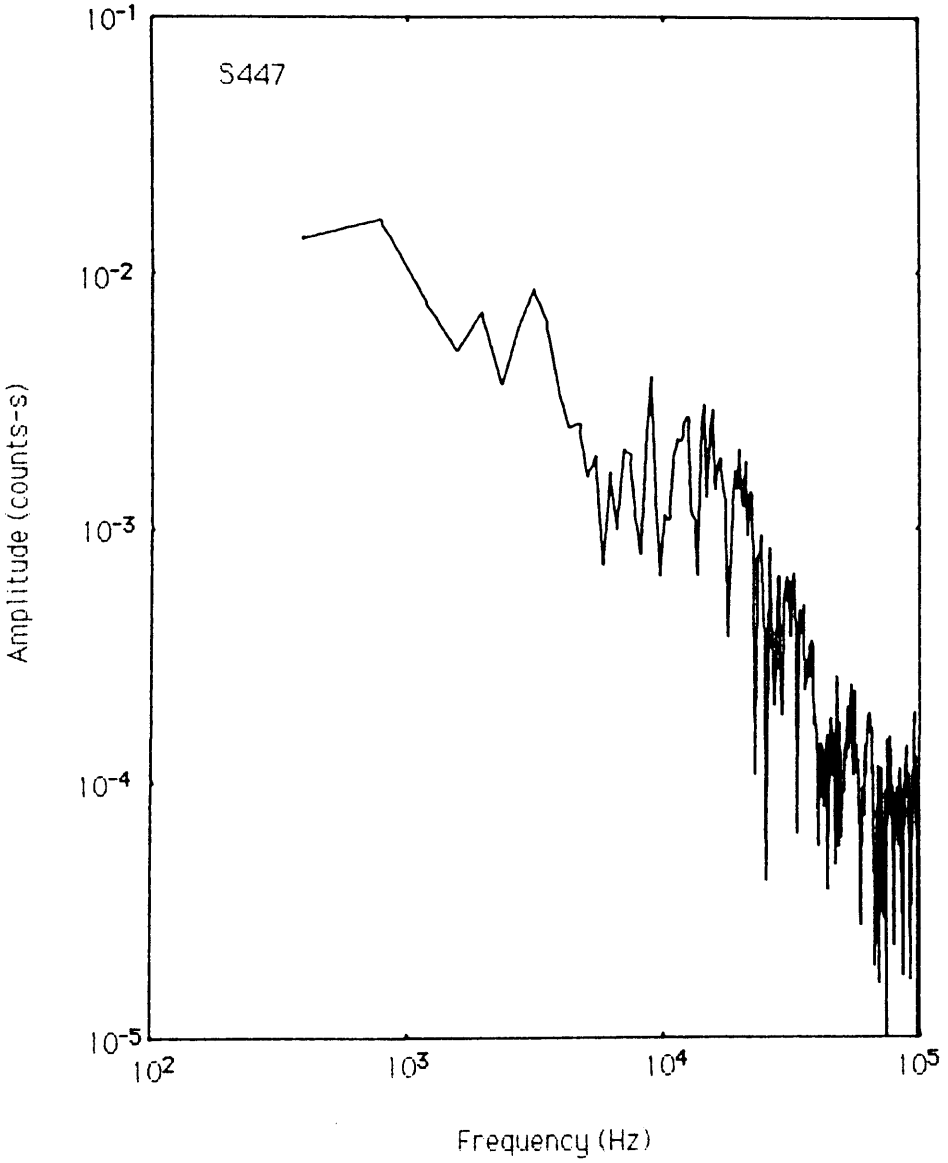
S447
10^{-1}
10^{-2}
10^{-3}
10^{-4}
10^{-5}
Amplitude (counts-s)
10^{2}
10^{3}
10^{4}
10^{5}
Frequency (Hz)

Figure 5.5a

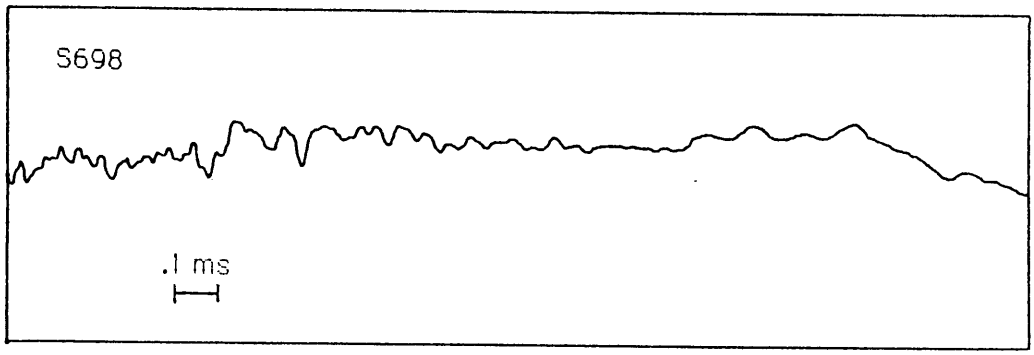
S698
.1 ms

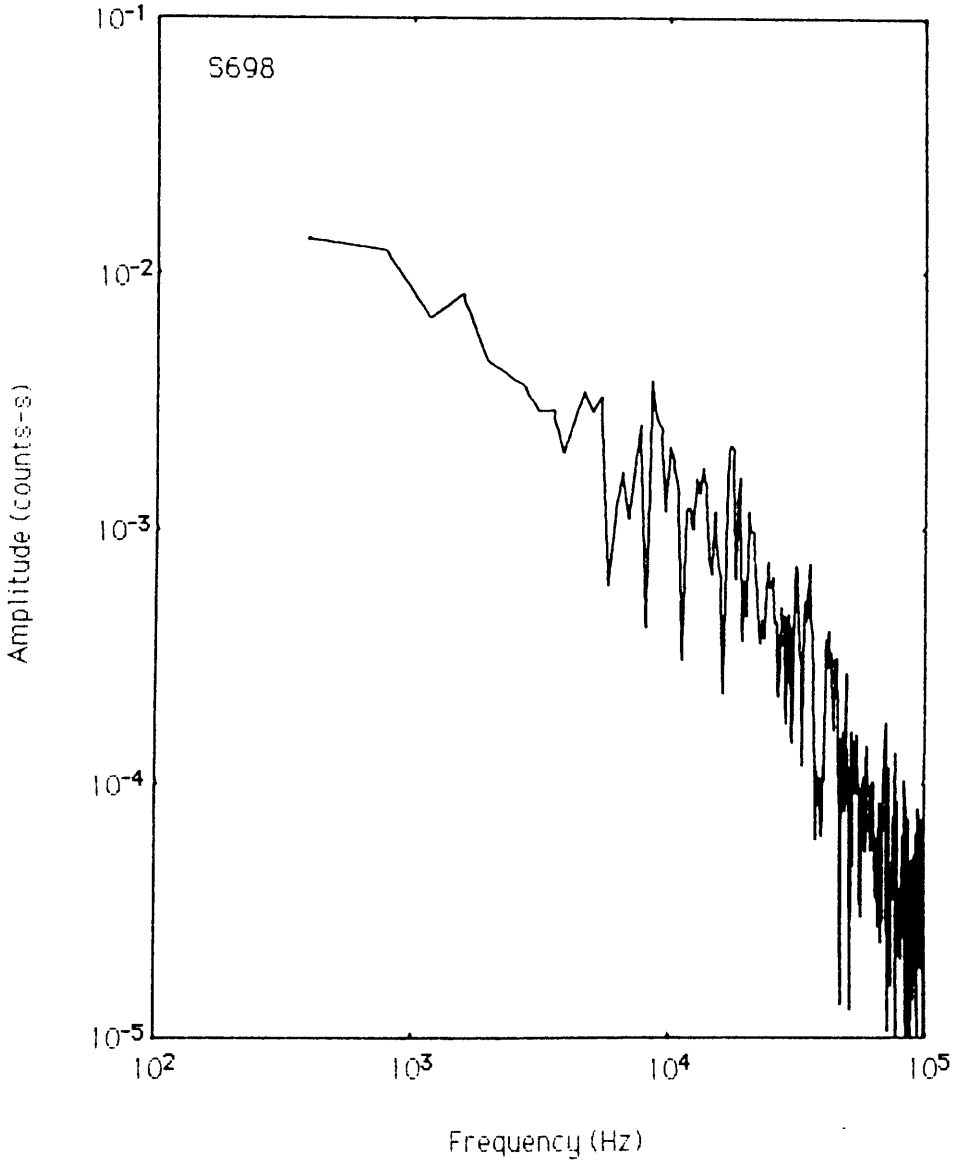
S698
10^{-1}
10^{-2}
10^{-3}
10^{-4}
10^{-5}
Amplitude (counts-s)
10^{2}
10^{3}
10^{4}
10^{5}
Frequency (Hz)

Figure 5.5b

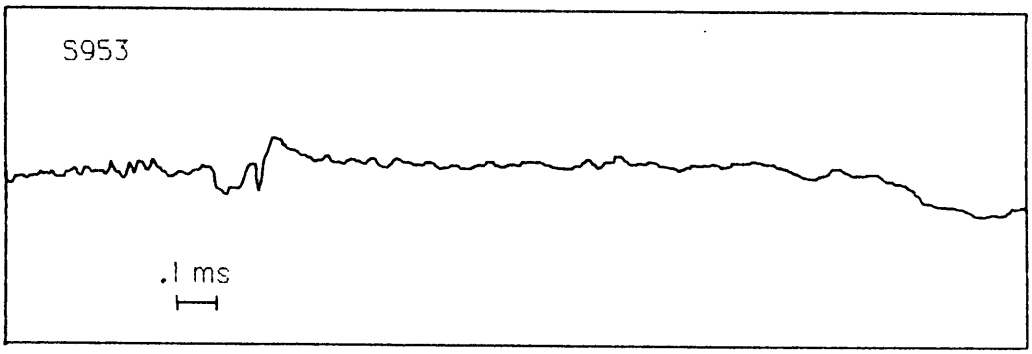
S953
.1 ms

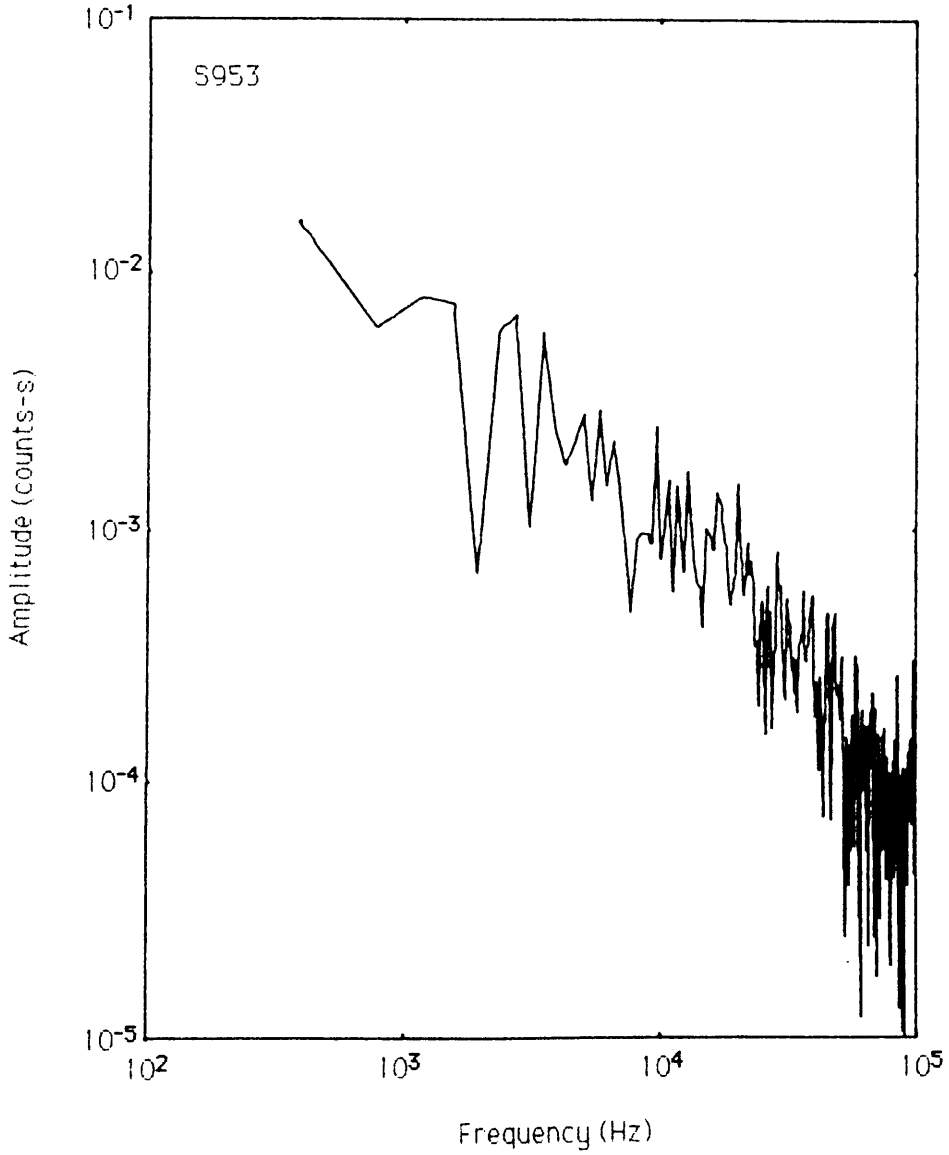
S953
10^{-1}
10^{-2}
10^{-3}
10^{-4}
10^{-5}
Amplitude (counts-s)
10^{2}
10^{3}
10^{4}
10^{5}
Frequency (Hz)

Figure 5.5c

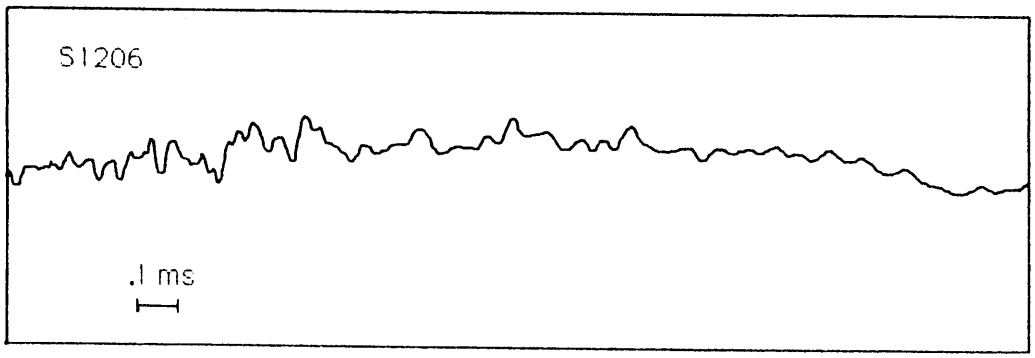
S1206
.1 ms

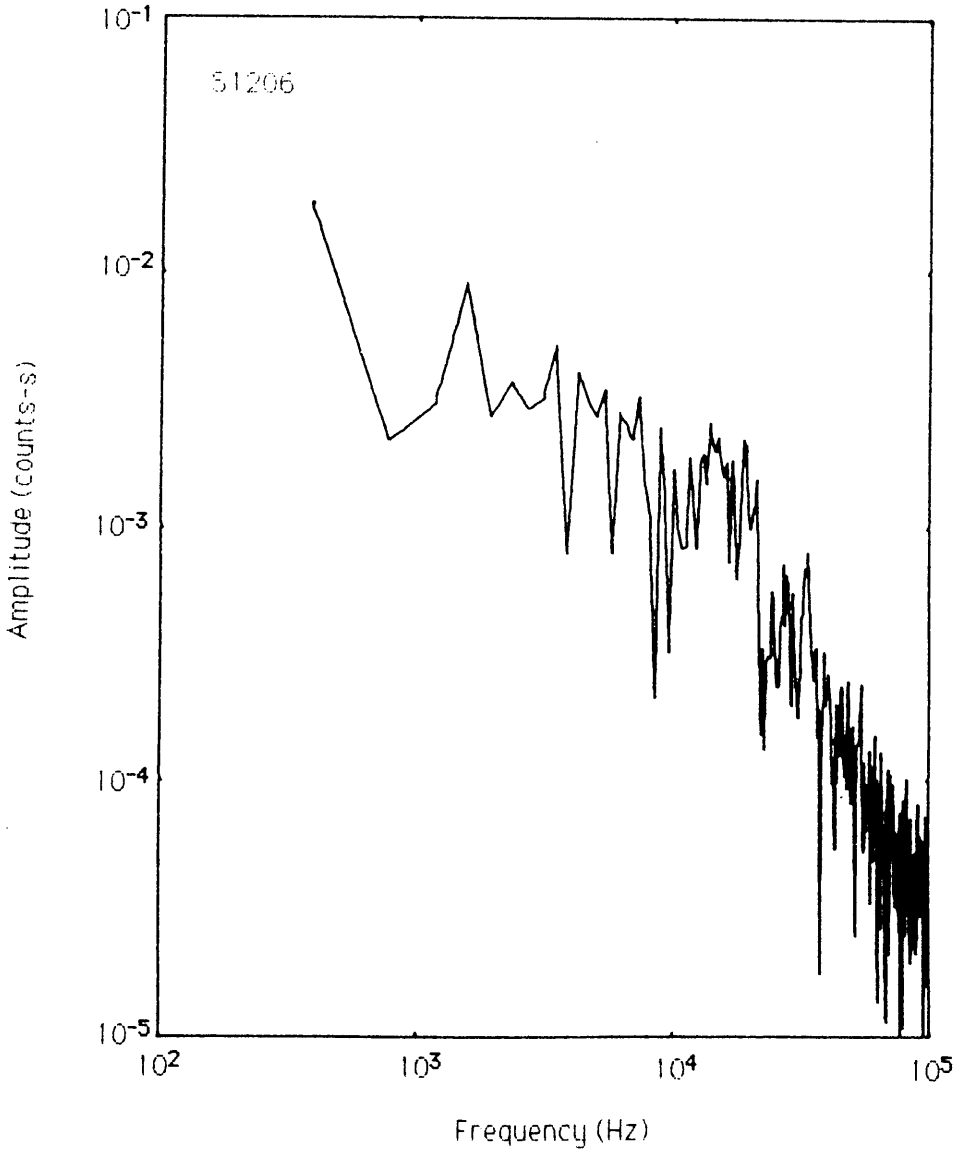
S1206
Amplitude (counts-s)
10-1
10-2
10-3
10-4
10-5
10²
10³
10⁴
10⁵
Frequency (Hz)

Figure 5.5d

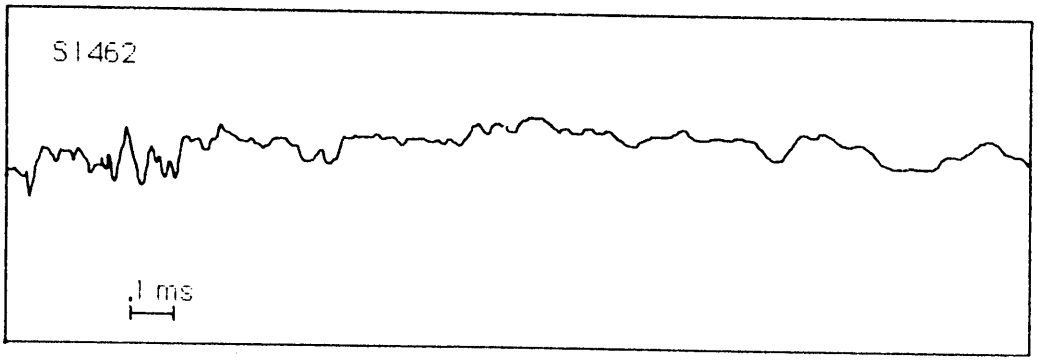
S1462
.1 ms

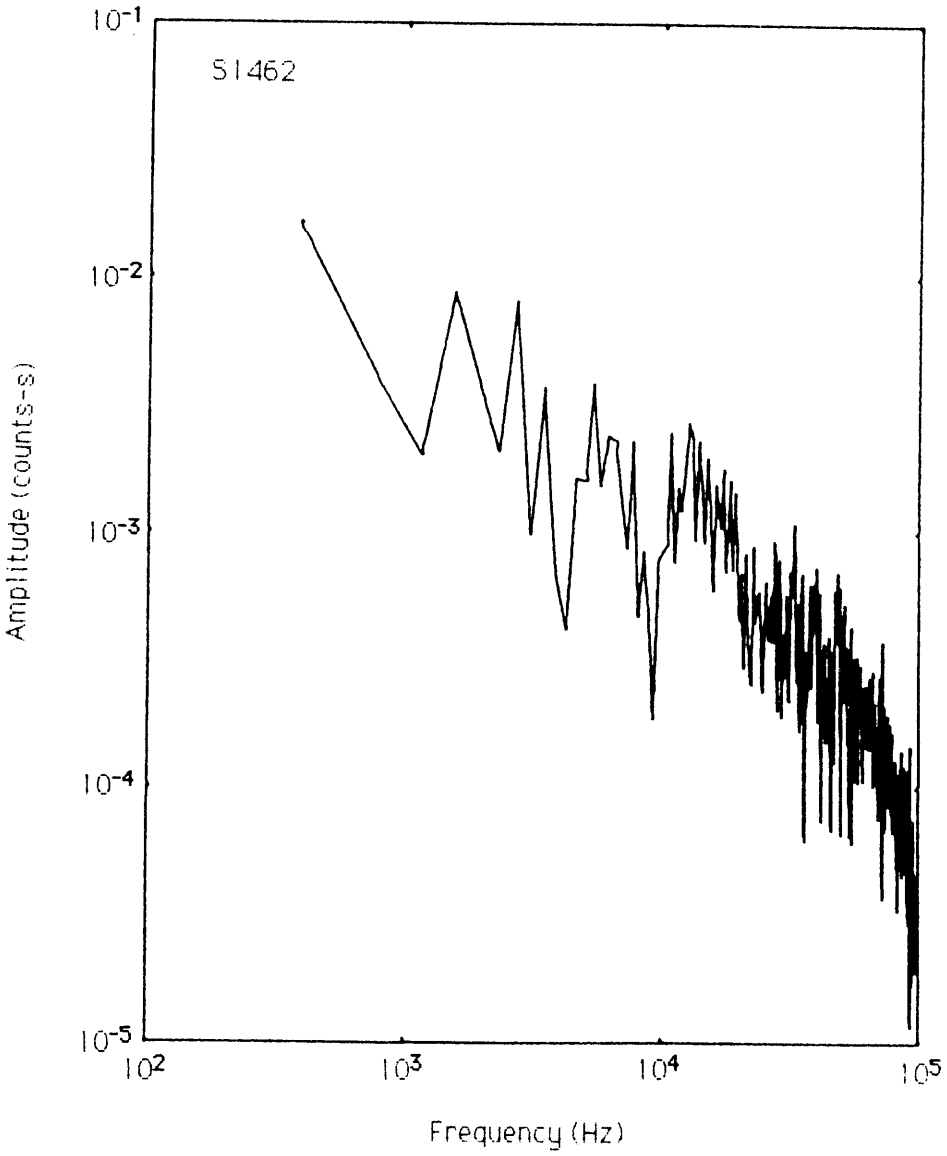
S1462
10^{-1}
10^{-2}
10^{-3}
10^{-4}
10^{-5}
Amplitude (counts-s)
10^{2}
10^{3}
10^{4}
10^{5}
Frequency (Hz)

Figure 5.5e

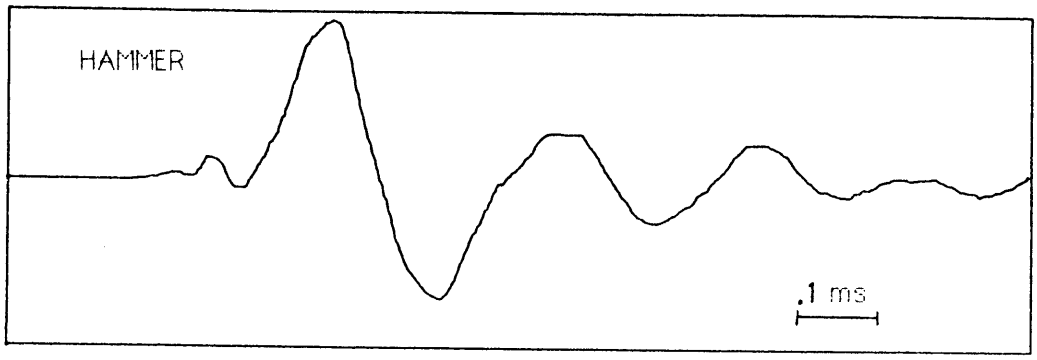
HAMMER
.1 ms

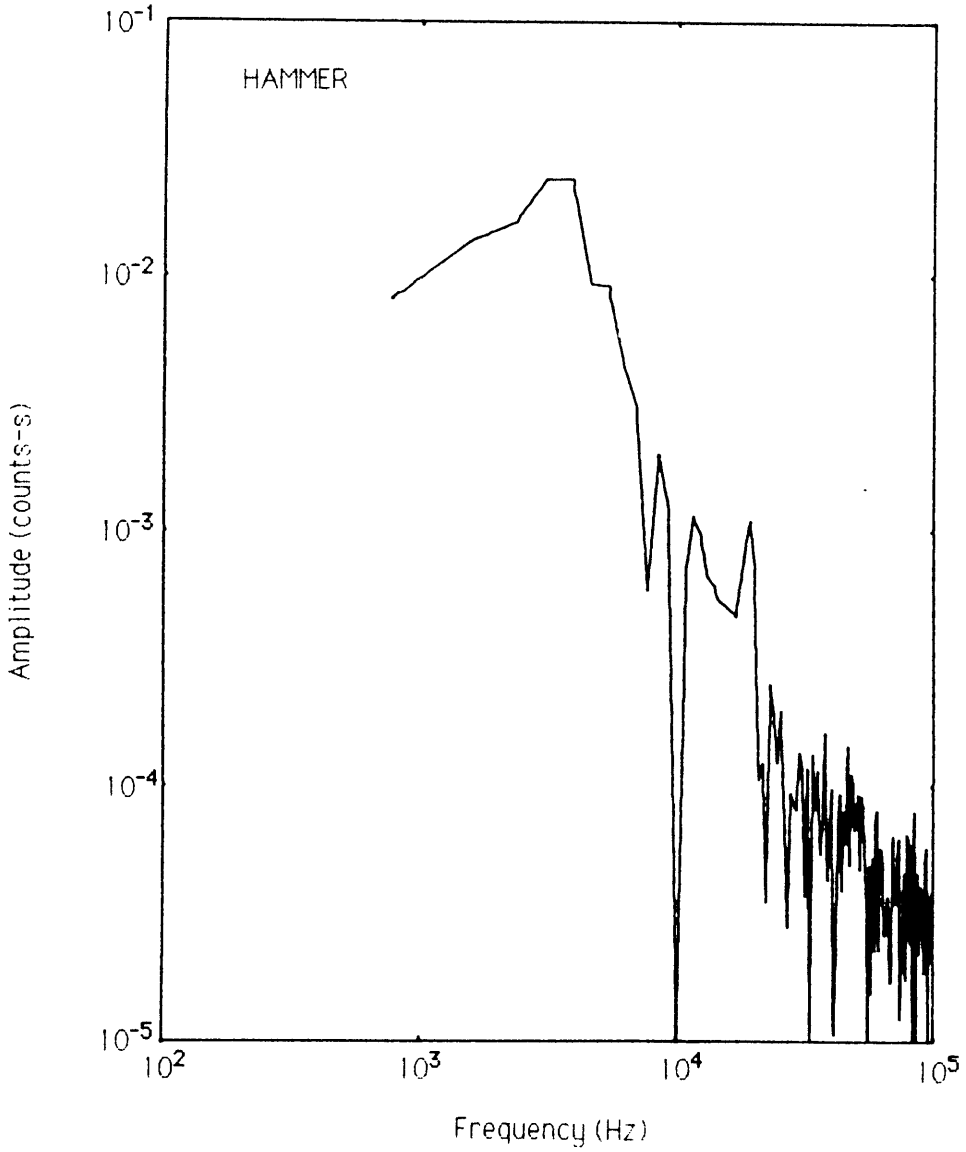
HAMMER
10^{-1}
10^{-2}
10^{-3}
10^{-4}
10^{-5}
Amplitude (counts-s)
10^{2}
10^{3}
10^{4}
10^{5}
Frequency (Hz)

Figure 5.6

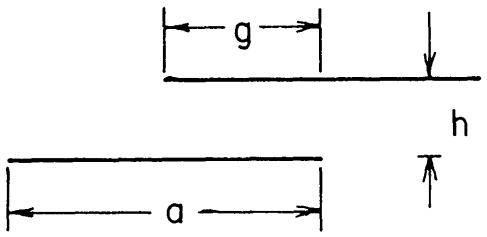

a = 4 cm
g = 2 cm
h = 1 cm

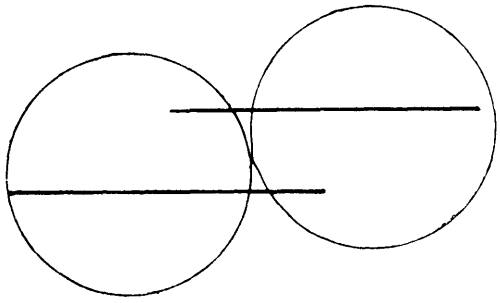

2r = 3·05 cm
L° = 6·10 cm

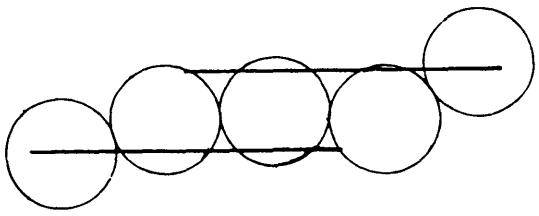

2r = 1·35 cm
L° = 6·75 cm

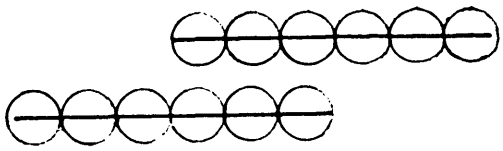

2r = 0·70 cm
L° = 8·40 cm

Figure 5.7

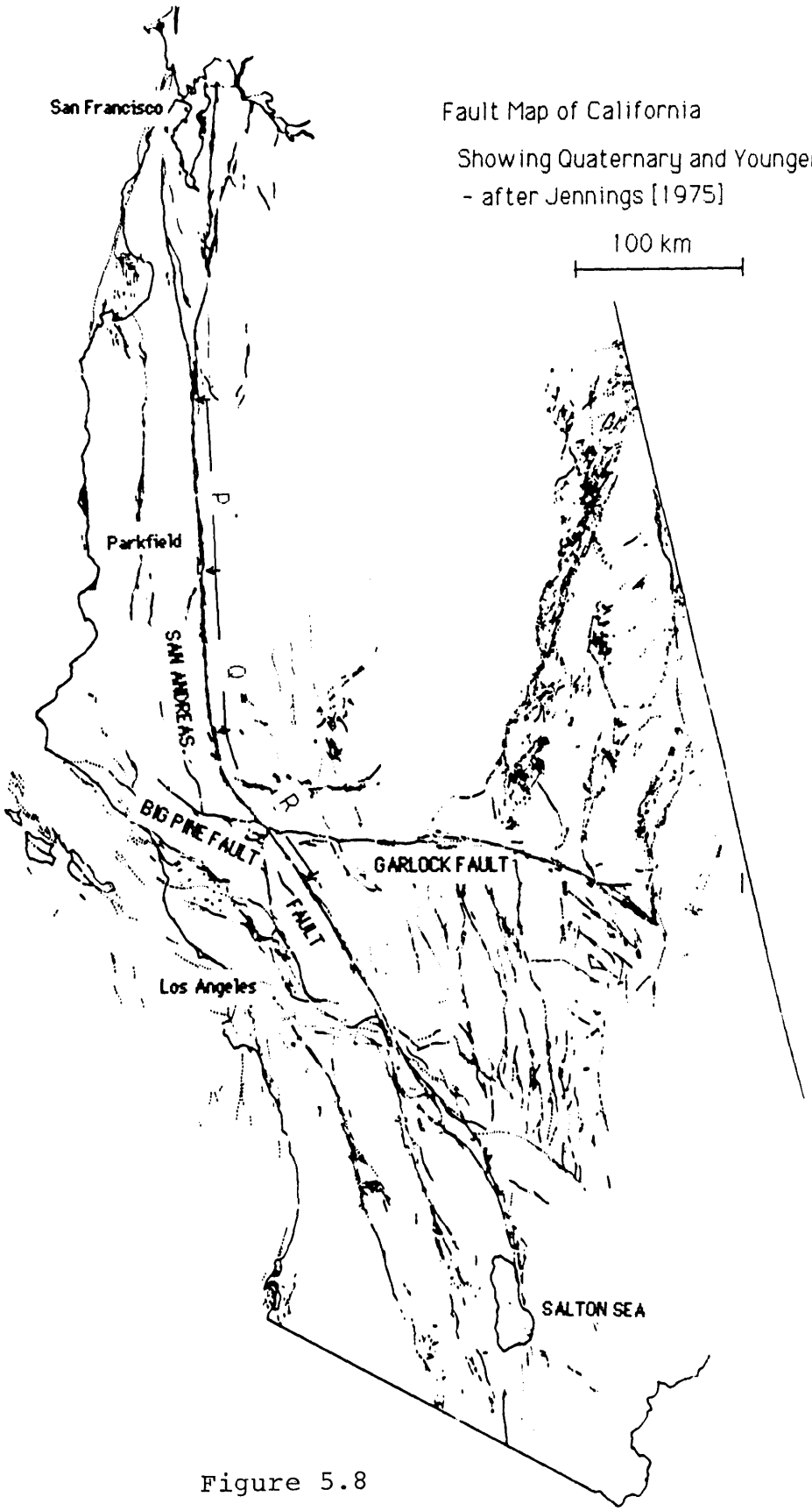
San Francisco
Fault Map of California
Showing Quaternary and Younger Faults
- after Jennings [1975]
100 km
Parkfield
SAN ANDREAS
BIG PINE FAULT
GARLOCK FAULT
FAULT
Los Angeles
SALTON SEA

Figure 5.8

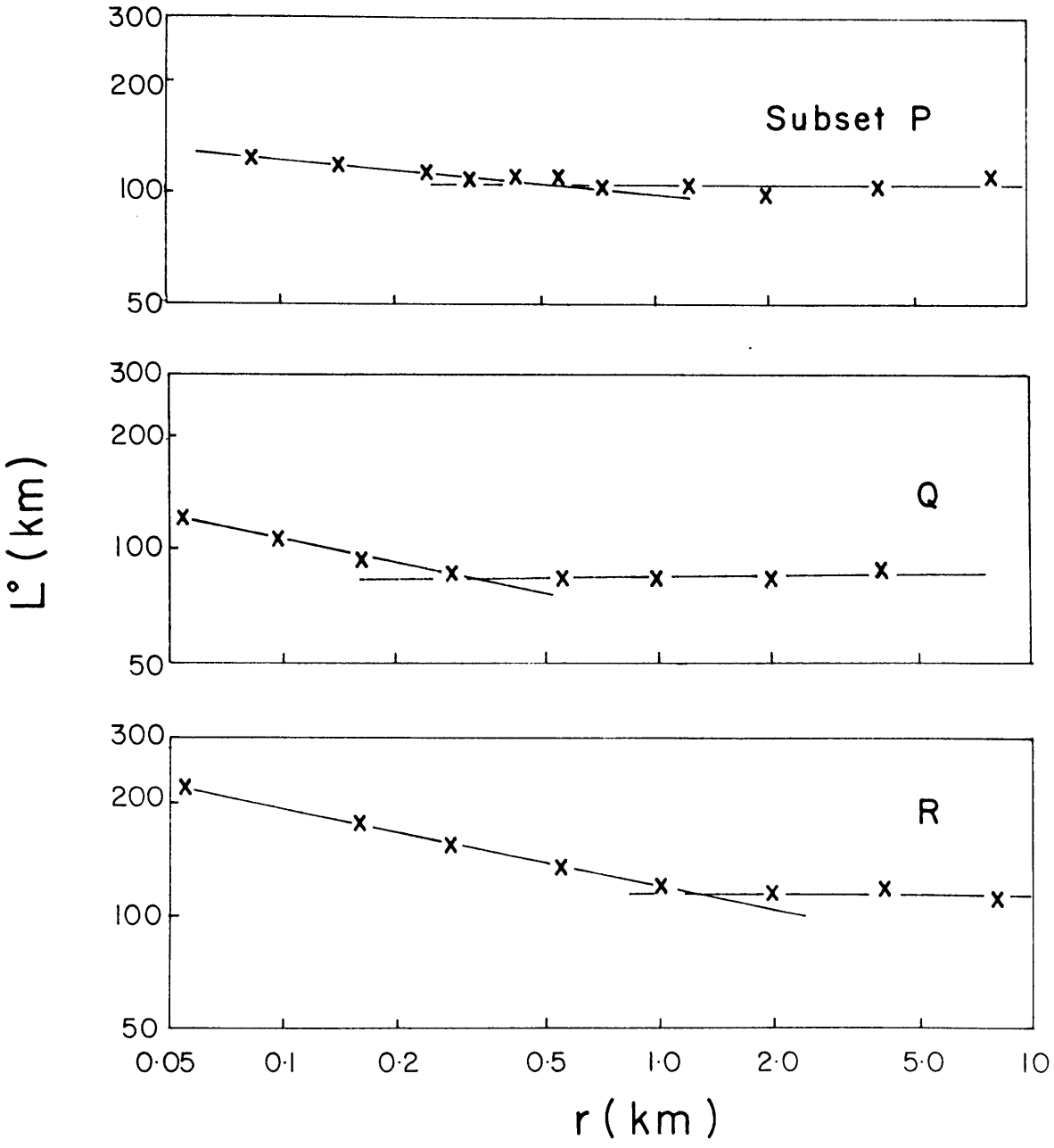
300
200
100
50
Subset P
300
200
100
50
Q
300
200
100
50
R
L° (km)
0·05
0·1
0·2
0·5
1·0
2·0
5·0
10
r (km)

Figure 5.9

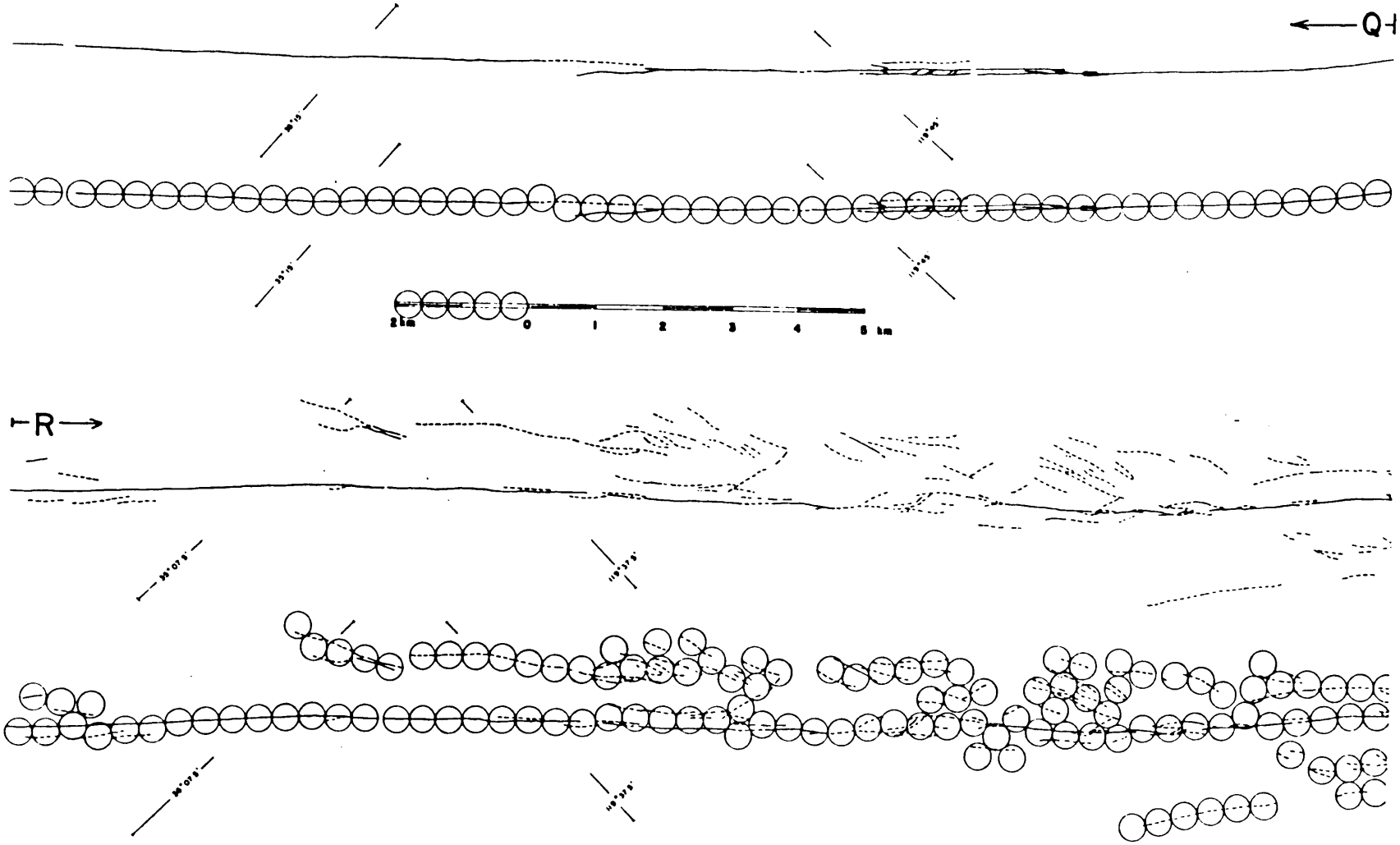

Figure 5.10

Chapter 6 - Concluding Discussion

In the preceding discussion, we have considered experimental and numerical, and, to a degree, conceptual, models of dynamic frictional instabilties. The discussion began, focused at the laboratory scale, somewhat larger than typically used in the laboratory, in order to obtain and interpret detailed observations of stick-slip failures. Among the key observations in that discussion is that of critical slip displacements associated with the onset of stick-slip instability. The existence of this critical slip increment implies the existence of a length scale which controls the frictional instability process. The large sample size allowed experiments to be performed with two values of this critical length, and the sample dimensions combined with high-speed recording capability in the laboratory allow resolution of features of the stick-slip failure process that provide direct insights into the behavior of shear fractures at these different scales. An apparent fracture energy which depends on loading and fault roughness parameters is measureable. This implies that shear fractures, certainly those on preexisting planes of weakness, are basically different from tensile fractures for which the energy required to promote crack extension is a material property.

It remains to understand physically what the critical displacement, which is referred to as d_c, represents. The experiments show that d_c is related to fault roughness such that rougher fault surfaces are characterized by larger d_c. Studies based on spectral analyses of the profiles of sliding surfaces for which d_c have been measured have been initiated, and an early interpretation has been that d_c corresponds to an average radius of contacting asperity (T. Tullis, personal communication). At any rate, phenomenologically, d_c represents the interval of adjustment that sliding surfaces require to respond to changes in the conditions of slip.

The observation of a d_c for the stick-slip events which resembled in behavior that observed in quasistatic sliding experiments was taken as a suggestion that a class of friction

models derived from the quasistatic experiments is also appropriate for describing the constitutive response of faults undergoing dynamic slip. It was found that it is, indeed, the case. The rate- and state-dependent friction model, although its introduction into rock mechanics by Dieterich [1979a] stemmed from material science principles and recent experiments indicate that surface chemistry effects appear to be important [Dieterich and Conrad, 1984], has been viewed largely as an empirical framework which has proven to be quite versatile both in accounting for observed laboratory behavior and in making predictions regarding the frictional response of systems ranging from idealized point mass sliders to crustal-scale seismogenic faults. There is still lively debate surrounding the use of state variable friction models, and it is quite clear that further laboratory study is required to resolve some of the remaining issues.

Some preliminary calculations of the dynamic growth of a fault governed by a state variable friction model indicate that these models can reproduce behavior that is observed for a slip weakening crack. Possibly important differences between rate- and state-dependent behavior and slip weakening behavior near the tip of the advancing crack are seen, but significant similarities are also seen. Differences which might be more relevant to strong ground motion predictions might be present during the rupture arrest stages, where the frictional sliding is decelerating. Further modeling in which nonuniform initial state properties are assigned over the fault surface would begin to address this question.

With the large scale testing it is possible to investigate the effects of length scales on the fault behavior. With laboratory-derived insights and numerical modeling, it is also possible to predict the effects of changing some of the critical scaling parameters. However, in the Earth for natural faults, large-scale irregularities such as fragmentation might be present which would complicate attempts to directly "scale-up" from the laboratory. Any program directed at such a scaling should include some means of identifying the scaling parameters and characterizing the system geometry. The use of fractal geometry has been

suggested, and its rather crude application to fault geometry in this thesis did point out that fault traces do exhibit fractal characteristics and that there are identifiable critical lengths in the fault trace geometry. More refined efforts to characterize the fractal geometry of faults point out the crucial nature of data selection, set definition and measurement technique [see, for example, Aviles *et al.*, 1985], but fractal geometry could be the means of initially highlighting the critical lengths to lead to an understanding of the scales of faulting.

References

Aki, K., Seismic displacements near a fault, J. Geophys. Res., 73, 5359-5376, 1968.

Aki, K., Characterization of barriers on an earthquake fault, J. Geophys.Res., 84, 6140-6148, 1979.

Aki, K., A probabilistic synthesis of precursory phenomena, in Earthquake Prediction - An International Review, M. Ewing Series, 4, American Geophysical Union, ed. by D. W. Simpson and P. G. Richards, 1981.

Allen, C. R., The tectonic environments of seismically active and inactive areas along the San Andreas Fault system, in Proceedings, Conference on Geologic Problems of the San Andreas Fault System, Stanford Univ. Pub. Geol. Sci., 11, ed. by W. R. Dickinson and A. Grantz, 1968.

Andrews, D. J., Rupture velocity of plane-strain shear cracks, J. Geophys. Res., 81, 5679-5687, 1976.

Andrews, D. J., A stochastic fault model - I. Static case, J. Geophys. Res., 85, 3867-3877, 1980.

Andrews, D. J., Dynamic plane-strain shear rupture with a slip-weakening friction law calculated by a boundary integral method, Bull. Seismol. Soc. Am., 75, 1-21, 1985.

Archuleta, R. J., A faulting model for the 1979 Imperial Valley earthquake, J. Geophys. Res., 89, 4559-4585, 1984.

Archuleta, R. J., and J. N. Brune, Surface strong motion associated with a stick-slip event in a foam rubber model of earthquakes, Bull. Seismol. Soc. Am., 65, 1059-1071, 1975.

Aviles, C. A., C. H. Scholz, and J. Boatwright, Fractal analysis applied to characteristic segments of the San Andreas Fault, preprint, 1985.

Bakun, W. H., R. M. Stewart, C. G. Bufe, and S. M. Marks, Implication of seismicity for failure of a section of the San Andreas Fault, Bull. Seismol. Soc. Am., 70, 185-201, 1980.

Barenblatt, G. I., The formation of equilibrium cracks during brittle fracture. General ideas and hypotheses: Axially symmetric cracks, Appl. Math. Mech., 23, 622-636, 1959.

Brace, W. F., and J. D. Byerlee, Stick-slip as a mechanism for earthquakes, Science, 153, 990-992, 1966.

Brace, W. F., and J. B. Walsh, Some direct measurements of the surface energy of quartz and orthoclase, Am. Mineral., 47, 111-112, 1962.

Brown, R. D., Map showing recently active breaks along the San Andreas and related faults

between the northern Gabilan Range and Cholame Valley, CA, Misc. Geologic Investigations, Map I-575, United States Geological Survey, 1970.

Brune, J. N., Tectonic stress and spectra of seismic shear waves from earthquakes, J. Geophys. Res., 75, 4997-5009, 1970.

Brune, J. N., Earthquake modeling by stick-slip along pre-cut surfaces in stressed foam rubber, Bull. Seismol. Soc. Am., 63, 2105-2119, 1973.

Burridge, R., Admissible speeds for plane-strain self-similar cracks with friction but lacking cohesion, Geophys. J. R. astr. Soc., 35, 439-455, 1973.

Burridge, R., and L. Knopoff, Body force equivalents for seismic dislocation, Bull. Seismol. Soc. Am., 54, 1875-1888, 1964.

Burridge, R., G. Conn, and L. B. Freund,The stability of a rapid mode II shear crack with finite cohesive traction, J. Geophys. Res., 84, 2210-2222, 1979.

Das, S., A numerical study of rupture propagation and earthquake source mechanism, Sc. D. thesis, 217 pp., Massachusetts Institute of Technology, Cambridge, Ma, 1976.

Das, S., A numerical method for determining source time functions for general three-dimensional rupture, Geophys. J. R. astr. Soc., 62, 591-604, 1980.

Das, S., and K. Aki, A numerical study of two-dimensional spontaneous rupture propagation, Geophys. J. R. astr. Soc., 50, 643-668, 1977a.

Das, S., and K. Aki, Fault plane with barriers: A versatile earthquake model, J. Geophys. Res., 82, 5658-5670, 1977b.

Day, S. M., Three-dimensional simulation of spontaneous rupture: The effect of nonuniform prestress, Bull. Seismol. Soc. Am., 72, 1881-1902, 1982.

Dieterich, J. H., Time-dependent friction in rocks, J. Geophys. Res., 77, 3690-3697, 1972.

Dieterich, J. H., Time dependent friction and the mechanics of stick-slip, Pageoph., 116, 790-806, 1978a.

Dieterich, J. H., Preseismic fault slip and earthquake prediction, J. Geophys. Res., 83, 3940-3947, 1978b.

Dieterich, J. H., Modeling of rock friction 1. Experimental results and constitutive equations, J. Geophys. Res., 84, 2161-2168, 1979a.

Dieterich, J. H., Modeling of rock friction 2. Simulation of preseismic slip, J. Geophys. Res., 84, 2169-2175, 1979b.

Dieterich, J. H., Experimental and model study of fault constitutive properties, in Solid Earth Geophysics and Geomechanics, Appl. Mech. Div., 42, American Society of Mechanical Engineers, ed. S. Nemat-Nasser, 21-30, 1980.

Dieterich, J. H., Potential for geophysical experiments in large scale tests, Geophys. Res.

Lett., 8, 653-656, 1981a.

Dieterich, J. H., Constitutive properties of faults with simulated gouge, in Mechanical Behavior of Crustal Rocks, Geophysical Monograph, 24, American Geophysical Union, eds. N. L. Carter, M. Friedman, J. M. Logan and D. W. Stearns, 103-120, 1981b.

Dieterich, J. H., A model for the nucleation of earthquake slip, preprint, submitted to 5th Ewing Symposium on Earthquake Mechanics, 1985.

Dieterich, J. H., and G. Conrad, Effect of humidity on time and velocity dependent friction, J. Geophys. Res., 89, 4196-4202, 1984.

Dieterich, J. H., D. W. Barber, G. Conrad, and Q. A. Gorton, Preseismic slip in a large scale friction experiment, Proceedings, 19th U. S. Rock Mechanics Symposium, 110-117, 1978.

Dugdale, A. S., Yielding of steel sheets containing slits, J. Mech. Phys. Solids, 8, 100-104, 1960.

Eaton, J. P., M. E. O'Neill, and J. N. Murdock, Aftershocks of the 1966 Parkfield-Cholame earthquake: a detailed study, Bull. Seismol. Soc. Am., 60, 1151-1197, 1970.

Freund, L. B., The mechanics of dynamic shear crack propagation, J. Geophys. Res., 84, 2199-2209, 1979.

Friedman, M., J. Handin, and G. Alani, Fracture surface energy of rocks, Int. J. Rock Mech. Min. Sci., 9, 757-766, 1972.

Goodman, R. E., and P. N. Sundaram, The influence of system stiffness and test mode on phenomena accompanying stick-slip on fault surfaces, Pageoph., 116, 873-887,1978.

Gu, J.-C., J. R. Rice, A. L. Ruina, and S. T. Tse, Slip motion and stability of a single degree of freedom elastic system with rate and state dependent friction, J. Mech. Phys. Solids, 32, 167-196, 1984.

Hamano, Y., Dependence of rupture time history on the heterogeneous distribution of stress and strength on the fault plane (abstract), EOS, Trans., American Geophys. Union, 55, 352, 1974.

Hartzell, S. H., and R. J. Archuleta, Rupture propagation and focusing of energy in a foam rubber model of a stick-slip earthquake, J. Geophys. Res., 84, 3623-3636, 1979.

Husseini, M. I., Energy balance for motion along a fault, Geophys. J. R. astr. Soc., 49, 699-714, 1978.

Ida, Y., Cohesive force across the tip of a longitudinal shear crack and Griffith's specific surface energy, J. Geophys. Res., 77, 3796-3805, 1972.

Ida, Y., The maximum acceleration of seismic ground motion, Bull. Seismol. Soc. Am., 63,

959-968, 1973.

Jennings, C. W., Fault map of California with locations of volcanoes, thermal springs and thermal wells, California Geologic Data Map Series, Map 1, California Division of Mines and Geology, 1975.

Johnson, T., and C. H. Scholz, Dynamic properties of stick-slip friction of rocks, J. Geophys. Res., 81, 881-888, 1976.

Johnson, T., F. T. Wu, and C. H. Scholz, Source parameters for stick-slip and for earthquakes, Science, 179, 278-280, 1973.

King, G. C. P., The accommodation of large strains in the upper lithosphere of the Earth and other solids by self-similar fault systems: the geometrical origin of b-value, Pageoph., 121, 761-815, 1984.

King, G. C. P., and G. Yielding, The evolution of a thrust fault system: processes of rupture initiation, propagation, and termination in the 1980 El Asnam, Algeria earthquake, Geophys. J. R. astr. Soc., 77, 915-933, 1983.

Kostrov, B., Selfsimilar problems of propagating of shear cracks, J. Appl. Math. Mech., 28, 1077-1087, 1964.

Kostrov, B., Unsteady propagation of longitudinal shear cracks, J. Appl. Math. Mech., 30, 1241-1248, 1966.

Lindh, A. G., and D. M. Boore, Control of rupture by fault geometry during the 1966 Parkfield earthquake, Bull. Seismol. Soc. Am., 71, 95-116, 1981.

Mandelbrot, B. B., Fractals : Form, Chance and Dimension, W. H. Freeman and Co., San Francisco, 365 pp., 1977. (Also: B. B. Mandelbrot, The Fractal Geometry of Nature, revised edition of Fractals, W. H. Freeman and Co., San Francisco, 468 pp., 1983.)

Mandelbrot, B. B., D. E. Passoja, and A. J. Paullay, Fractal character of fracture surfaces of metals, Nature, 308, 721-722, 1984.

Maruyama, T., On force equivalents of dynamic elastic dislocations with reference to earthquake mechanism, Bull. Earthquake Res. Inst., Tokyo Univ., 41, 462-486, 1963.

Mavko, G. M., Large-scale earthquakes from a laboratory friction law, preprint, 1983.

Mikumo, T., and T. Miyatake, Dynamic rupture process on a frictional fault model with non-uniform frictions and near-field waves, Geophys. J. R. astr. Soc., 54, 417-438, 1978.

Mikumo, T., and T. Miyatake, Earthquake sequences of a frictional fault model with non-uniform strengths and relaxation times, Geophys. J. R. astr. Soc., 59, 497-522, 1979.

Ohnaka, M., Experimental studies of stick-slip and their application to the earthquake source

mechanism, J. Phys. Earth, 21, 285-303, 1973.

Ohnaka, M., Applications of some dynamic properties of stick-slip to earthquakes, Geophys. J. R. astr. Soc., 53, 311-318, 1978.

Okubo, P. G., and J. H. Dieterich, Fracture energy of stick-slip events in a large scale biaxial experiment, Geophys. Res. Lett., 8, 887-890, 1981.

Okubo, P. G., and J. H. Dieterich, Effects of physical fault properties on frictional instabilities produced on simulated faults, J. Geophys. Res., 89, 5815-5827, 1984.

Palmer, A. C., and J. R. Rice, The growth of slip surfaces in the progressive failure of over-consolidated clay, Proc. R. Soc. London, A332, 527-548, 1973.

Papageorgiou, A. S., and K. Aki, A specific barrier model for the quantitative description of inhomogeneous faulting and the prediction of strong ground motion, Part I Description of the model, Bull. Seismol. Soc. Am., 73, 693-722, 1983a.

Papageorgiou, A. S., and K. Aki, A specific barrier model for the quantitative description of inhomogeneous faulting and the prediction of strong ground motion, Part II Applications of the model, Bull. Seismol. Soc. Am., 73, 953-978, 1983b.

Paterson, M. S., Experimental Rock Deformation - The Brittle Field, Minerals and Rocks, 13, Springer-Verlag, New York, 1978.

Reasenberg, P., and W. L. Ellsworth, Aftershocks of the Coyote Lake, CA earthquake of August 6, 1979: A detailed study, J. Geophys. Res., 87, 10637-10655, 1982.

Reid, H. F., Mechanics of the earthquake, in The California Earthquake of April 18, 1906, V 2, Carnegie Inst. of Washington, D. C., 1910.

Rice, J. R., The mechanics of earthquake rupture, Proceedings, Int. Sch. Phys., Enrico Fermi, Italian Physical Society, in Physics of the Earth's Interior, 78, ed. by E. Boschi and A. M. Dziewonski, North-Holland, Amsterdam,555-649, 1980.

Rice, J. R., Constitutive relations for fault slip and earthquake instabilities, Pageoph., 121, 443-475, 1983.

Rice, J. R., and S. T. Tse, Dynamic motion of a single degree of freedom system following a rate- and state-dependent friction law, preprint, submitted to J. Geophys. Res., 1985.

Richards, P. G., Dynamic motions near an earthquake fault : a three-dimensional solution, Bull. Seismol. Soc. Am., 66, 1-32, 1976.

Ross, D. C., Map showing recently active breaks along the San Andreas Fault between Tejon Pass and Cajon Pass, CA, Misc. Investigations Series, Map I-553, United States Geological Survey, 1969.

Ruina, A. L., Slip instability and state variable friction laws, J. Geophys. Res., 88, 10359-10370, 1983.

Rummel, F., H.-J. Alheid, and C. Frohn, Dilatancy and fracture-induced velocity changes in rock and their relation to frictional sliding, Pageoph., 116, 743-764, 1978.

Segall, P., and D. D. Pollard, Mechanics of discontinuous faults, J. Geophys. Res., 85, 4337-4350, 1980.

Shimamoto, T., J. Handin, and J. M. Logan, Specimen-apparatus interaction during stick-slip in a triaxial compression machine: A decoupled two-degree of freedom model,Tectonophysics, 67, 175-205, 1980.

Sieh, K. E., Slip along the San Andreas Fault associated with the great 1857 earthquake, Bull. Seismol. Soc. Am., 68, 1421-1448, 1978.

Smalley, R. F., D. L. Turcotte, and S. A. Solla, A renormalization group approach to the stick-slip behavior of faults, J. Geophys. Res., 90, 1894-1901, 1985.

Stesky, R. M., Mechanisms of high temperature frictional sliding in Westerly granite, Can. J. Earth Sci., 15, 361-375, 1978.

Tchalenko, J. S., Similarities between shear zones of different magnitudes, Geol. Soc. Am. Bull., 81, 1625-1640, 1970.

Tse, S. T., Mechanics of Crustal Strike-slip Earthquakes in Relation to Frictional Constitutive Response, PhD thesis, 160 pp. Harvard University, Cambridge, MA, 1985.

Tullis, T. E., and J. D. Weeks, Constitutive behavior and stability of frictional sliding on granite, preprint, submitted to 5th Ewing Symposium on Earthquake Mechanics, 1985.

Vedder, J. G., and R. E. Wallace, Map showing recently active breaks along the San Andreas and related faults between Cholame Valley and Tejon Pass, CA, Misc. Geologic Investigations, Map I-574, United States Geological Survey, 1970.

Wang, C. Y., X. J. Shi, Z. Q. Guo, and T. Hasegawa, Direct measurement of stick-slip and shear fracture energy of granite at elevated pressures, preprint, 1985.

Wong, T.-F., Shear fracture energy of Westerly granite from post-failure behavior, J. Geophys. Res., 87, 990-1000, 1982.

Wong, T.-F., On the normal stress dependence of shear fracture energy, preprint, submitted to 5th Ewing Symposiuim on Earthquake Mechanics, 1985.

Wu, F. T., K. C. Thomson, and H. Kuenzler, Stick-slip propagation velocity and seismic source mechanism, Bull. Seismol. Soc. Am., 62, 1621-1628, 1972.